Understanding the atmospheric turbulence structure parameter, C_n^2, in the littoral regime

by

Carlos O. Font Jiménez

A thesis submitted in partial fulfillment of the requirements for the degree of

MASTER OF SCIENCE
in
PHYSICS

UNIVERSITY OF PUERTO RICO
MAYAGÜEZ CAMPUS
2006

Approved by:

_____	_____
Mark P. J. L. Chang, Ph.D. President, Graduate Committee	Date
_____	_____
Erick Roura, Ph.D. Member, Graduate Committee	Date
_____	_____
Héctor Jiménez, Ph.D. Member, Graduate Committee	Date
_____	_____
José Rosado, Ph.D. Representative of Graduate Studies	Date
_____	_____
Héctor Jiménez, Ph.D. Chairperson of the Department	Date

Abstract

Understanding optical propagation through atmospheric turbulence is a highly important step for the efficient implementation of a free space laser communication system and for achieving diffraction limited imaging over long paths. The project reported has studied the refractive index structure parameter, C_n^2, as function of local bulk meteorological conditions. We present the data collected and the methodology used during the campaigns of the past 3 years. In our analysis we address the greatest limitation that affects studies of turbulence data, the non-stationary and non-linear characteristics which severely limit the usefulness of traditional time series analysis. We have devised a new mathematical technique, referred to as the Hilbert Phase Analysis (HPA) and we report on its implementation and testing in this work.

Resumen

Entender la propagación óptica a través de los efectos de turbulencia atmosférica es un paso importante para la implementación efectiva de sistemas de comunicación por láser y de toma de imágenes a través de la atmósfera a largas distancias. Este trabajo presenta el estudio del parámetro de estructura del índice de refracción de la atmósfera,, C_n^2 , en función de las condiciones climáticas locales. Aquí presentamos la data obtenida y la metodología implementada en los distintos experimentos por los pasados 3 años. En nuestro análisis trabajamos con la limitación más grande para el análisis de nuestra data de turbulencia, la data no posee características de ser estacionaria ni linear, lo cual limita severamente el análisis por métodos tradicionales. Hemos desarrollado una nueva técnica matemática nombrada “Hilbert Phase Analisys” (HPA) y reportamos su implementación y pruebas en este trabajo.

Dedicated to Bolita…

Acknowledgements

I would like to thanks all the people that directly or indirectly were involved in the success of this work.

I would like to give special thanks to my advisor, Dr. Mark Chang, for all his support along all this years and for helping me become who I am today. To my graduate committee Dr. Erick Roura and Dr. Héctor Jiménez, thank you for all the trust and all the encouragement you gave me that that made me follow this career. To Dr. Pablo Marrero, for all those words of support and advice during these years. Also I have to include Dr. Carlos Pabón for all his advice and all those interesting conversations about my project and different topics.

I want to thank also all my family for their support throughout my life that helped me to reach all my goals. To my very special groups of friends, which are like my second family along all my University life, Freddie, Luis Balbino, Erick Roura, Angelica, Pablo Marrero, Teddy, Yaireska, Evelyn, Emily, Yaitza, Deby, Cynthia, Jennifer and Bolita between other great friends.

To the US Naval Research Lab for all the support provided through these experiments and to all their team work related to this research, Eun Oh, Dr. Charmaine Gilbreath, Dr. Sergio Restaino & family, and Christopher Wilcox.

Finally but not least, I want to give many thanks to a person who gave me great support day by day during the hard process of writing this thesis in a short period of time and under a lot of pressure. Thanks Zamárit.

Table of Contents

Page

Abstract……..ii

Resumen……iii

Acknowledgements……v

Table of Contents……..vi

List of Figures……viii

List of Tables……ix

Glossary……..x

1. **Introduction**…….....2

   1.1 *Light traveling through the atmosphere*……...2
2. **Background Theory**…….....5

   2.1 The refractive index structure function (C_n^2) ……..5
   2.1.1 Scintillation basis…….....5
   2.1.2 Atmospheric Refractive Index Fluctuations……...6
3. **Calibration**……..10

   3.1 Instrument Overview……..10

   3.2 Instrument Cross Calibration……....12

   3.2.1 Landbound region…….12

   3.2.2 Littoral region……...15

   3.3 Calibration Conclusion……..18
4. **Experiments**……19

   4.1 Physics Building, UPRM Experiment…….....20
   4.2 Chesapeake Bay Detachment, CBD Experiment……...21
   4.3 Magueyes Island, HOPA VIPh Experiment……...23
5. **Experiments results**…….…..27

   5.1 Data Analysis Methods……..27

   5.1.1 Empirical Mode Decomposition (EMD)…….. ...27

   5.1.2 The Analytical Signal……...30

   5.1.3 Hilbert Phase Analysis…….....31
   5.2 Experiments Results……...32

   5.2.1 CBD Experiment…….....32

   5.2.2 UPRM Experiment……38

   5.2.3 HOPA VIPh Experiment…….....41

6. **Conclusions**…….47

References……...……..50

Appendix A Published Conferences Proceedings……52

- Humidity contribution to the refractive index structure function C_n^2……..53
- On the relationship between C_n^2 and humidity……62
- Applying the Hilbert–Huang Decomposition to Horizontal Light Propagation C_n^2data…….…….....74
- Applying the Hilbert Phase Analysis to the study of Atmospheric Turbulence Data……...……..82

Appendix B Submitted Journal Paper …….83

- Humidity's influence on visible region refractive index structure parameter C_n^2……...…….84

List of Figures

Figures **Page**

1.1 Representation of light from a point source - ……...2
2.1 Representation of Kolmogorov cascade theory. …….....8
3.1 LOA-004 Scintillometer ……10
3.2 Calibration alignment…….....13
3.3 February 28, 2006 C_n^2 data…….....13
3.4 February 28 2006. C_n^2 data from the Scintillometer 2 and Scintillometer 1...-….....14
3.5 February 28 2006. C_n^2 data from the Scintillometer 2 and Scintillometer 1…-……..15
3.6 September 3 & 4 2006. C_n^2 data from the Scintillometer 2 and Scintillometer 1 …...16
3.7 September 3 & 4 2006. C_n^2 data from the Scintillometer 2 and Scintillometer 1……16
3.8 Cross correlation coefficients…….....17
4.1 Sketch of the Experiment at the top of the Physics Building (UPRM Exp)……20
4.2 Aerial view of the Chesapeake Beach Detachment…….22
4.3 View of the area where the CBD experiment was performed…….....23
4.4 Aerial view of the experimental site and representations……24
4.5 View of the transmitter at the top of the hotel…….25
4.6 View of the transmitter at the top of the hotel…….25
4.7 Weather Station located with the Receiver #2 at the hotel……..26
5.1 This figure shows the basic algorithm for the EMD method…….....28
5.2 C_n^2 data corresponding to March 9, 2006, smoothed with a 30 values rolling……29
5.3 IMFs calculated for the C_n^2 data collected on March 9, 2006 at UPRM Exp……..29
5.4 C_n^2 data from the CBD experiment on November 9 2003……...32
5.5 November 3 2003, night. Correlogram (left), Cross-Covariance (right)…….34
5.6 Plot comparing the minimum coefficient……35
5.7 March 28 2004, morning…….....37
5.8 March 9, 2006, UPRM Experiment…….38
5.9 March 7, 2006, UPRM Experiment…….39
5.10 March 9, 2006. Plot of the cross covariance's……...40
5.11 February 28, 2006. Plot of the cross covariance's…….41
5.12 August 27, 2006. C_n^2 data for both Scintillometer…….42
5.13 Cross Covariance of HPA for the New Scintillometer……..42
5.14 Cross Covariance of HPA for the Old Scintillometer……43
5.15 Cross Covariance of HPA for the New Scintillometer……..44
5.16 Cross Covariance of HPA for the Old Scintillometer……45
5.17 Plot of Cn2 data of the three different experiments……...46

List of Tables

Tables **Page**

5.1 Statistical values for the analyzed cases from CBD experiment…….33
5.2 Values of the cross covariance coefficients at zero lag……...35
5.3 Principal differences between the 3 experiments……46

Chapter 1: Introduction

1.1 Light traveling through the atmosphere

Light from a point source propagates as spherical waves. After long distances of propagation a small section of these spherical waves can be assumed to be planar waves. That is the case of star light incident on the Earth. Once the starlight propagates through the Earth's atmosphere, it will suffer from atmosphere induced effects. These can be considered as two separate items: attenuation effects and index of refraction effects.

We illustrate the distortions in response to the changes of refractive index in the atmosphere in figure 1.1.

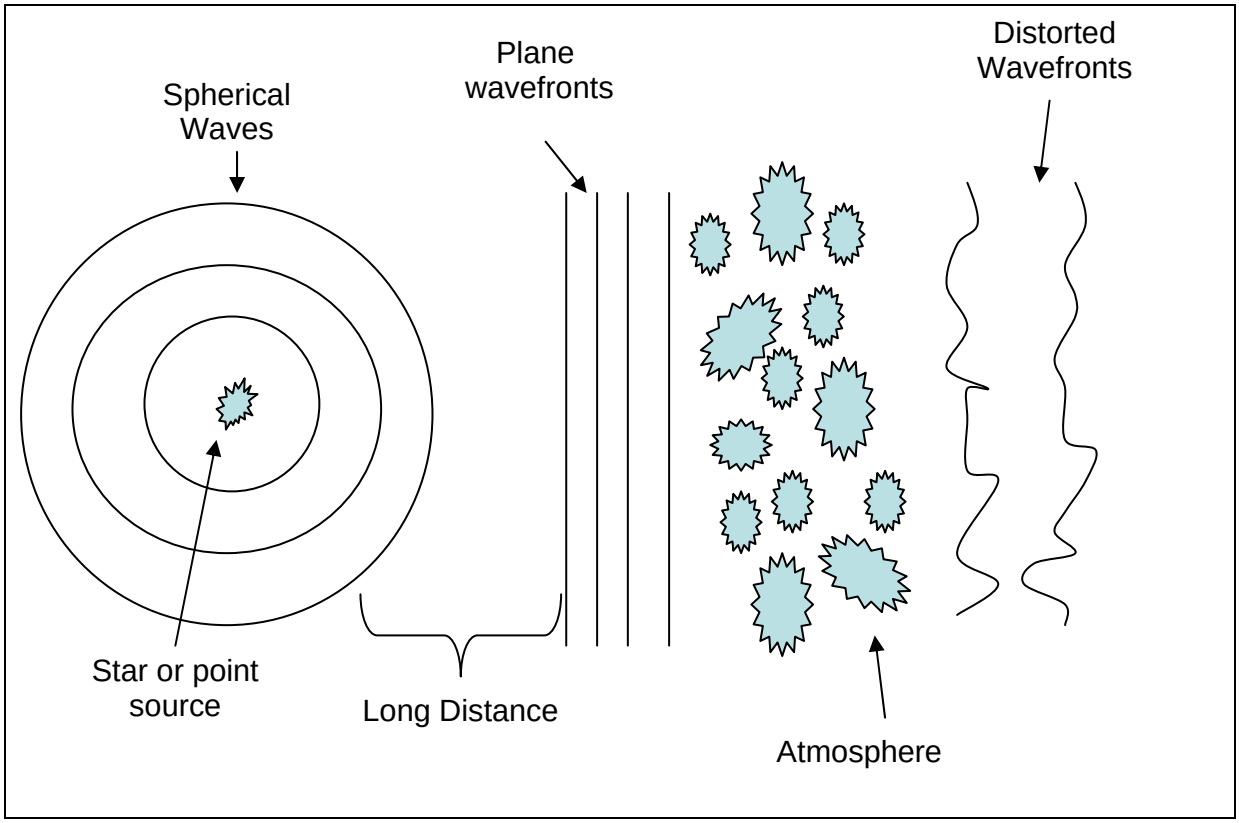

Figure 1.1 Representation of light from a point source traveling through the atmosphere.

The atmosphere is a non-homogeneous system in which properties will be sensitive to changes in pressure, temperature, humidity and wind speed/direction. Properties also will vary as a function of the altitude with respect to the Earth surface due the layered nature of the atmosphere. This layered nature and the sensitivity of the non-homogeneous system to different variables creates the turbulent fluctuations in the refractive index of the atmosphere, producing phase fluctuations in the traveling wavefront.

Atmospheric turbulence is a major problem for imaging and energy transport. During the past decades most studies in this area have been directed along the vertical propagation paths, for astronomical observations and imaging. However, in recent years, research in horizontal path propagation has been increased due the efforts for the improvement of free space optical communication systems and low altitude astronomical observations.

Turbulence on the optical field, leads to scintillation, absorption and scattering, where scintillation is the effect of interest in this work. The absorption and scattering effects by the atmosphere are wavelength dependent and give rise primarily to attenuation of the optical wave.

The structure parameter of refractive index or as it is better known, C_n^2, is the physical parameter used to describe the magnitude of the atmospheric turbulence in the atmosphere which is related to the scintillation effect and is defined to be wavelength independent.

In the lowest layer of the atmosphere this atmospheric turbulence parameter has been related to different bulk weather parameters like the solar insolation circle and fluctuations in wind speed/direction, temperature and pressure. But however, no complete theory or model exists which precisely explains its behavior.

In order for this work to be able to make a contribution towards solving the problems described before, specific objectives had to be addressed as listed below,

- take measurements of C_n^2 in the weak turbulence regime where the C_n^2 is claimed to be proportional to the *Rytov varian*ce [4]
- examine the first order effects of the local weather in the C_n^2 parameter
- find a valid method of analysis to analyze in a qualitative and quantitative way the possible contributions of the local weather parameters over the C_n^2.

With these objectives fulfilled, we were able to demonstrate the necessity to have available a mathematical tool which allow the study and the quantification of the effects of different local weather parameters over the C_n^2 parameter.

This dissertation is laid out in the following format:

Chapter 1. Introduction

Chapter 2. Background Theory

Chapter 3. Calibration

Chapter 4. Experiments

Chapter 5. Data Analysis

Chapter 6. Conclusions

Chapter 2: Background Theory

2.1 The refractive index structure function (C_n^2)

The refractive index structure function, C_n^2, is a parameter which describes the magnitude of the turbulence effects in the atmosphere for the optical range. Most of the studies refer to this turbulence as an effect of turbulent air motion and fluctuations where the source of energy for this motion are the gradients or changes in heating and cooling of the atmosphere and Earth surface caused mostly for sunlight and diurnal cycle. One characteristic of turbulent air motion is that is unpredictable, which made this more as a general study of optical wave propagation through a random media. As a random media we refer to a system were it basic properties are random functions of space and time.

The physical meaning of the refractive index structure function C_n^2 is a measurement of the strength of the fluctuations in the refractive index in the atmosphere. This parameter can be classified in two different regimes: weak turbulence and strong turbulence. Typically values for the weak turbulence regime are 10^{-17} $m^{-2/3}$ or less and for strong turbulence regime up to 10^{-13} $m^{-2/3}$ or more. The $m^{-2/3}$ units are derived from dimensional analysis.

2.1.1 Scintillation basis

Scintillation can be described as the destructive and constructive interference of optical waves caused by the fluctuations in the index of refraction along the optical path causing changes in intensity in the optical beam [6]. The scintillation index is perhaps the

most immediate and easy variable to measure in function of space and time and that allow a direct relation with the C_n^2 parameter. The scintillation index is defined by

$$\sigma_1^2 = \frac{< I^2 >}{< I >^2} - 1 \qquad (1)$$

where I is the intensity and the brackets < …> denotes an ensemble average. Applying the optical wave model of an infinite plane wave it can be characterized by the *Rytov variance* which represent what we normally know as the scintillation index or the normalized irradiance variance. By the *Rytov approximation*[1] then

$$\sigma_{Rytov} = \sigma_1^2 = 1.23 C_n^2 k^{7/6} L^{11/6}, \qquad [unitless] \qquad (2)$$

It claims a direct relation between the C_n^2 and the scintillation index, where $k = \frac{2\pi}{\lambda}$ is the optical wave number, λ (m) is the wavelength and L (m) is the propagation path length. This relation is true for the weak turbulence regime which is also defined as $\sigma_1^2 < 1$. This relationship shows that the scintillation is product of the small fluctuations on the refractive index of the atmosphere in function of time.

2.1.2 Atmospheric Refractive Index Fluctuations

In optical wave propagation through the atmosphere the index of refraction is a significant parameter of study. This parameter is sensitive small-scale fluctuations in different weather parameters like temperature and pressure. At a determined point in space in some specific time it can be expressed as

$$n(R,t) = n_0 + n_1(R,t) \qquad (3)$$

where $n_0 \approx 1$ and $n_1(R, t)$ represent the random deviation of the atmospheric refraction index. This term represent the changes due the random behavior of the atmosphere. For optical and IR wavelengths the refractive index can be written as

$$n(R) = 1 + 77.6 * 10^{-6}(1 + 7.52 * 10^{-3}\lambda^{-2})\frac{P(R)}{T(R)} \qquad (4)$$

or assuming $\lambda \approx .5$ μm due the small dependence λ for optical frequencies

$$n(r) \cong 1 + 79 * 10^{-6}\frac{P(R)}{T(R)} \qquad (5)$$

according to [4]. Here λ is the wavelength in μm, P is pressure in millibars and T temperature in Kelvin.

The behavior of the C_n^2 along a propagation path can be related to the fluctuations in the atmospheric refractive index from the temperature structure function, C_T^2, obtained from the difference of the mean-square of point measurements of temperature along the path. Then from equation 5 the C_n^2 can be directly inferred by

$$C_n^2 = (79 * 10^{-6}\frac{P}{T^2})^2 C_T^2 \qquad (6)$$

This statistical description is similar to the description related to random field of turbulent velocities, where are inertial subrange exist bounded by the outer scale L_0 and the inner scale l_0. The inner and outer scales are defined in the classical theory of turbulence developed in the early 1940s by Kolmogorov which concern random fluctuations in the magnitude and direction of the velocity field of a fluid [3].
The concepts of outer scale and inner scale comes from Kolmogorov cascade theory, which assume that this turbulent eddies go from a macroscale to a microscale in size, which create a continuum decreasing eddies as seen in figure 2.1. This idea comes in

visualize the atmosphere in two distinct states of motion, laminar and turbulent. Laminar assume a constant and uniform behavior and turbulent that the atmosphere lose its uniform characteristic due the dynamic mixing and acquire random subflows called turbulent eddies. A transition from laminar characteristic to turbulent characteristic in the atmosphere were occurs when the Reynolds number get to a critical point. Reynolds number are define as,

$$\mathrm{Re} = \frac{Vl}{v} \qquad \text{[unitless]} \qquad (7)$$

where V is speed of the flow (m/s), l is the dimension (m) and v is the kinematic viscosity (m^2/s).

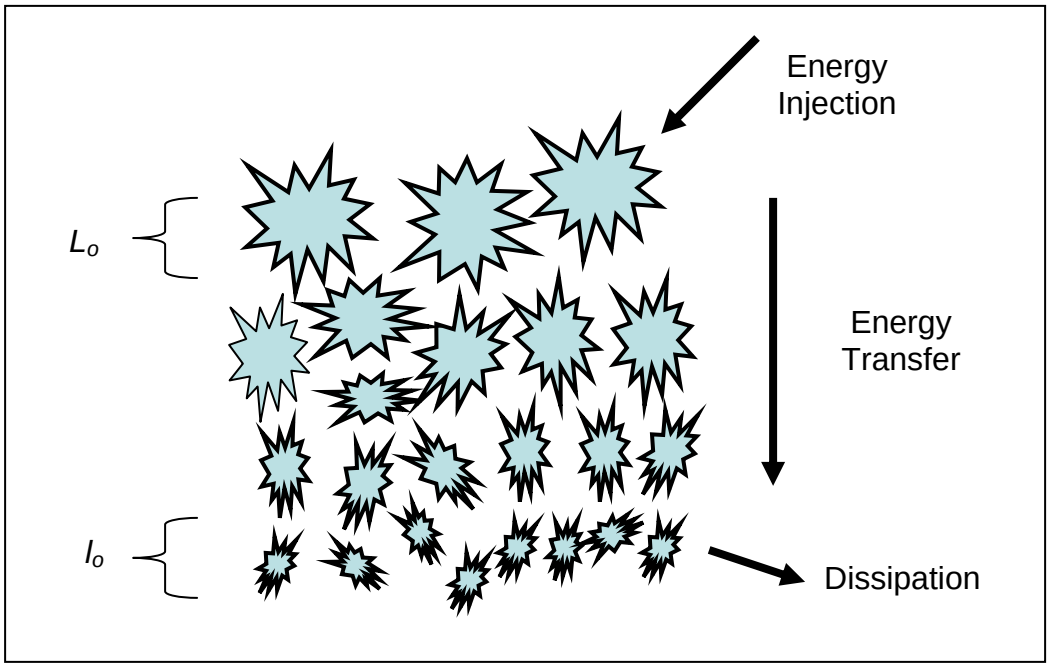

Figure 2.1: Representation of Kolmogorov cascade theory. The area between the outer scale and inner scale form the inertial subrange. L_o represent the outer scale and l_o represent the inner scale

It claims that when the field of velocity fluctuations within the inertia subrange show properties of statistical homogeneity and isotropy, the corresponding inertial subrange of the refractive index fluctuation will inherit those properties too.

Chapter 3: Calibration

3.1 Instrument Overview

For the purpose of this work, a specialized instrument for the measurement of C_n^2 was used. The Optical Scientific, Inc LOA-004 scintillometer systems consists of a transmitter and a receiver system and is shown in figure 3.1.

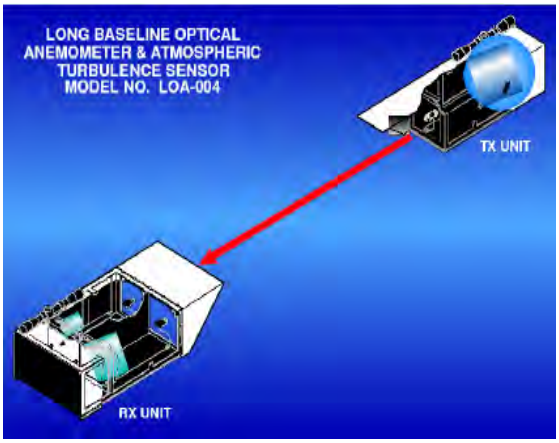

Figure 3.1: LOA-004 Scintillometer

The transmitter consists of a single diode which emits its central wavelength in the infrared band ($\lambda = 0.94\mu m$), although its bandwidth extends significantly into the red end of visible, and its beam is converted to a diverging beam using a 6 inch mirror located in the system.

On the other side, the receiver consists of two single pixel detectors, as seen in figure 3.1 with a broader bandwidth from 0.65 to 1.0 microns. These instruments also work as an anemometer measuring the transverse component of the wind through the propagation path. As an output the instruments provide a time vector with the C_n^2 values, the wind speed values and the voltage values received by each receptor channel. Also provided is a status value which indicates when the detectors operate outside of their calibrated region, which generally

occurs due to too high or too low incident intensity caused by misalignment, loss of power at the transmitter or saturation of the signal in the receptor channels.

The C_n^2 measurements determined by the LOA-004 system is a path integrated which come from the computation of the log-amplitude scintillation ($C_x(r)$) of the two receiving signals. Due the equation for the log-amplitude covariance function of Kolmogorov turbulence by Clifford *et al.* [17], equation 1, it is possible to relate the ($C_x(r)$) computed by the instrument with the C_n^2 parameter.

$$C_x(r) = 2.94\int_0^1 du\,\sigma_T^2(u)[u-(1-u)^{\frac{5}{6}}]\int_0^\infty dy\,y^{\frac{-11}{6}}\sin^y \exp\{\sigma_T^2[u(1-u)]^{\frac{5}{6}}F(y)\}J_0\left\{\left[\frac{4\pi yu}{(1-u)}\right]^{\frac{1}{2}}r\right\} \qquad (1)$$

where r is the separation between the two point detectors in Fresnel zones $\sqrt{\lambda L}$, with L being the path distance between the transmitter and the receiver; y is the normalized spatial wavenumber; $u = \frac{z}{L}$ is the normalized path position; J_0 is the zero order Bessel function of the first kind and

$$\sigma_T^2(u) = 0.124k^{\frac{7}{6}}L^{\frac{11}{6}}C_n^2(u) \qquad (2)$$

$$F(y) = 7.02y^{\frac{5}{6}}\int_{0.7y}^{\infty} d\xi\,\xi^{\frac{-8}{5}}\left[1-J_0(\xi)\right] \qquad (3)$$

To simplify this relations in order to understand the algorithm implemented for the instrument a weighting function $W(u)$, equation 4 can be defined

$$W(u) = 0.365k^{\frac{7}{6}}L^{\frac{11}{6}}\left[u(1-u)\right]^{\frac{5}{6}}\int_0^\infty dy\,g(u,y)J_0\left\{\left[\frac{4\pi yu}{(1-u)}\right]^{\frac{1}{2}}r\right\} \qquad (4)$$

such that

$$C_x(r) = \int_0^1 du C_n^2(u) W(u) \qquad (5)$$

assuming point source and point receivers. The information related to the C_n^2 for point sources and receivers is carried in the term $g(u, y)$ from the expression above. This instrument also made an important point for the calculations of the C_n^2 that the turbulent power spectrum is Kolmogorov meaning that the spatial power spectrum of temperature fluctuations $\Phi_T^2(k)$ and the humidity fluctuations $\Phi_H^2(k)$ are proportional to $k^{\frac{-5}{3}}$.

3.2 Instrument Cross Calibration

3.2.1 Landbound region

Two identical LOA-004 Scintillometers were used for these experiments, provided by the US Naval Research Lab in Washington DC. For initial cross calibration, the instruments were set up side by side on the UPRM Experiment, during the spring of 2006 at an approximate propagation distance of 90 meters. Data was collected data for almost 7 weeks. Because of the divergence of the transmitted beam from each individual system, to avoid cross contamination the systems were aligned with the transmitter and receiver of each on opposite sides of the beam path, as seen in figure 3.2.

The data collected was filtered using the status value provided by the instruments. Once all the data was filtered we identified a day where both instruments had taken good values over a full 24 hours. The data of the instruments was correlated to verify the precision of the measurements of one instrument respect to the other. The data from the instrument that

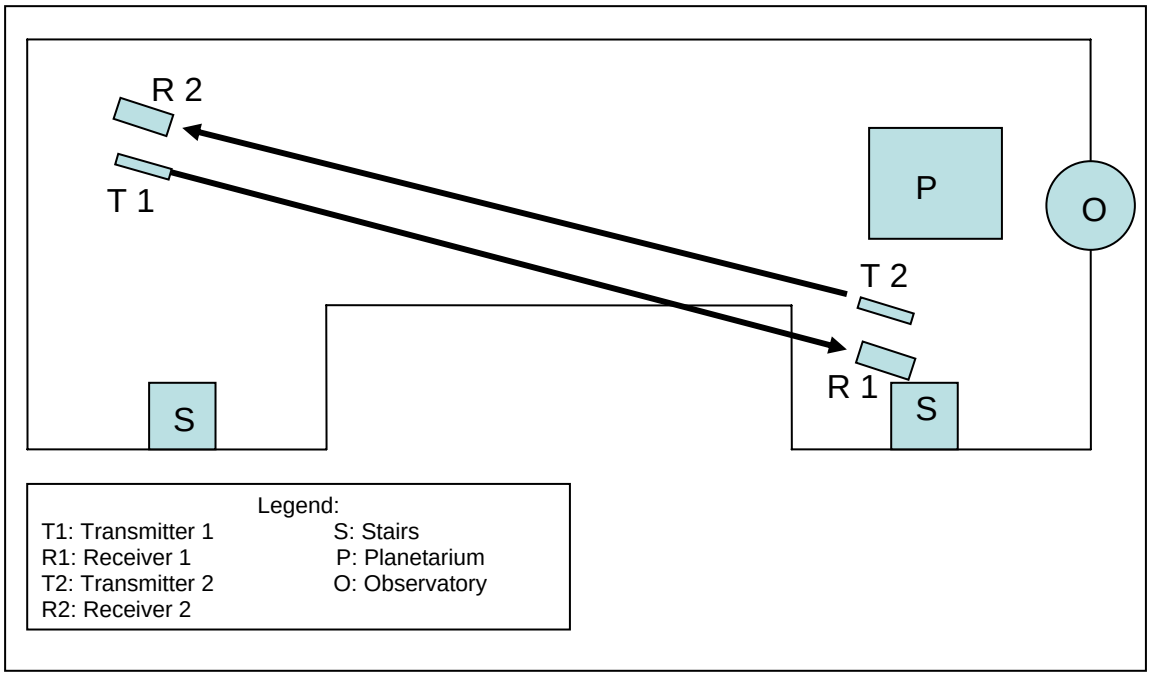

Figure 3.2: Calibration alignment.

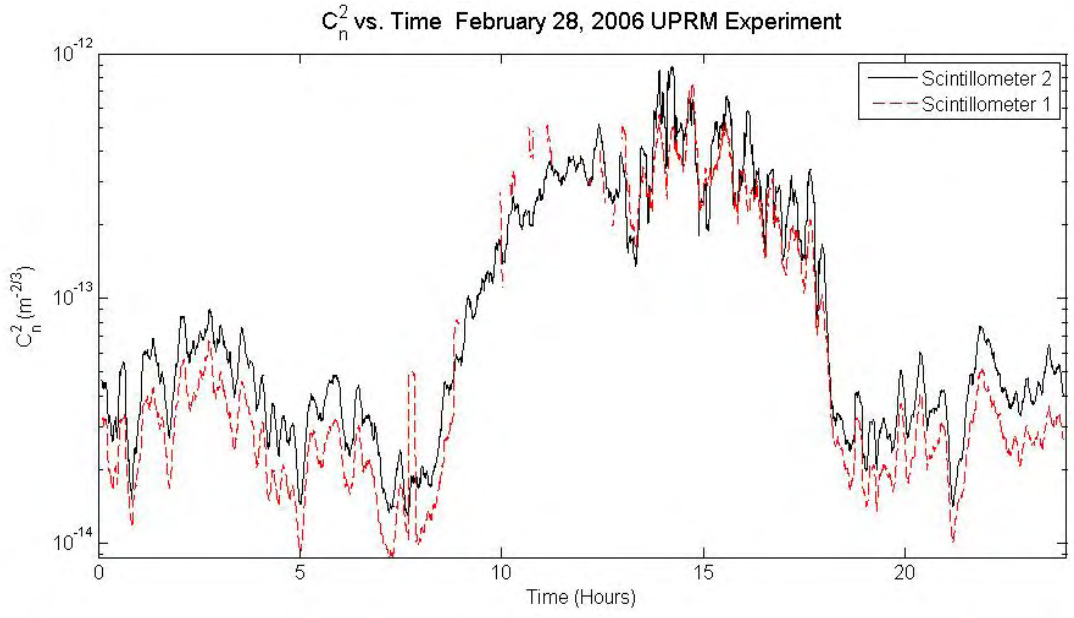

Figure 3.3: February 28, 2006 C_n^2 data.

we name Scintillometer 1 and Scintillometer 2, both over a time period of 24 hours and with a sample rate of 0.1 Hz. In order to better visualize data trends, the data were smoothed using a simple rolling average function. This is also known as boxcar smoothing. The width of the rolling average window can be varied at will, of course. We see in figure 3.4 (top) shows the C_n^2 raw data with its cross correlation as a function of time lag below in figure 3.4 (bottom). Perhaps figure 3.5 (top) show the same C_n^2 data but with a 30 values rolling average or what is equivalent to 5 minutes in our time vector. It is very clear how smoothing the data improve the correlation between the signals of both instruments when we compare the cross correlation coefficient. To investigate the effect of smoothing on the cross correlation

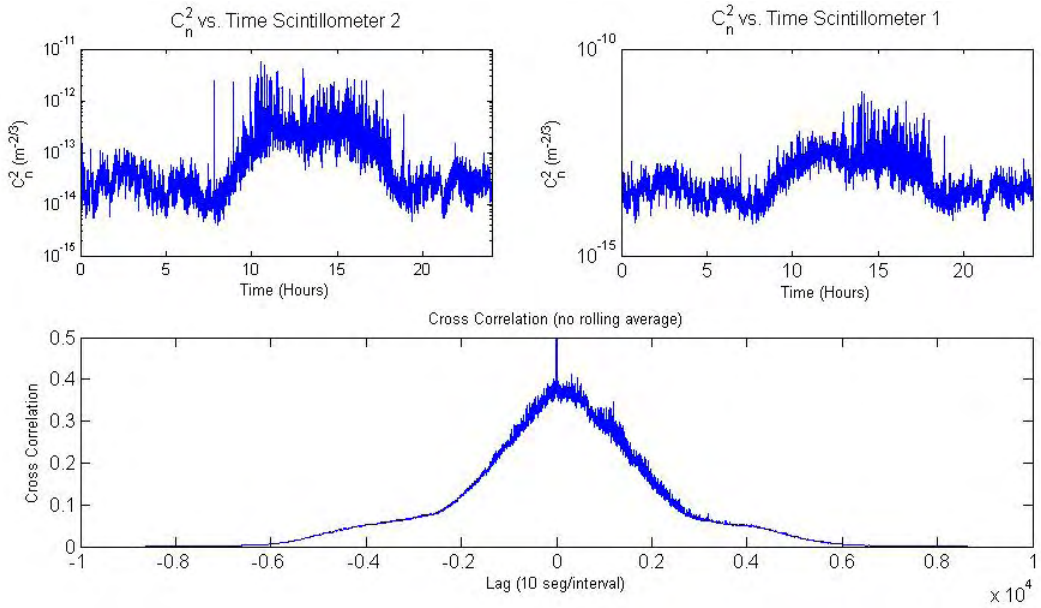

Figure 3.4: February 28 2006. C_n^2 data from the Scintillometer 2 and Scintillometer 1 are plotted on the top graphs respectively, this is the raw data. The bottom graph correspond to the cross correlation between the two signals.

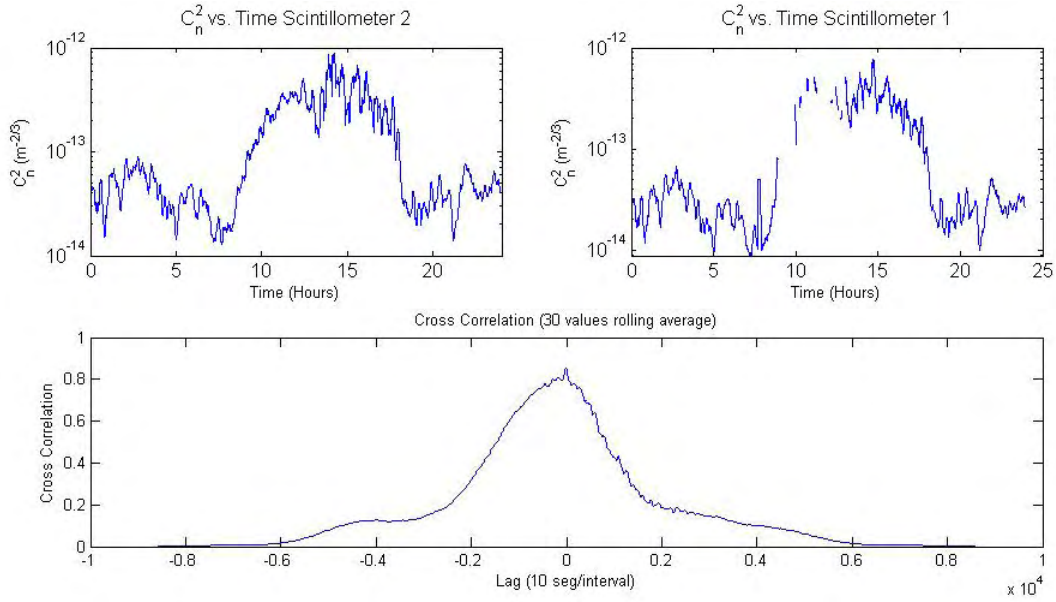

Figure 3.5: February 28 2006. C_n^2 data from the Scintillometer 2 and Scintillometer 1 are plotted on the top graphs respectively; this is with a 30 value rolling average. The bottom graph correspond to the cross correlation between the two signals.

between the two signals, we plot the cross correlation as a function of a 30 value boxcar width, figure 3.8. The blue line corresponds to the data previous described and we can observe that the maximum correlation factor is obtained when the smoothing width was 30 values. The maximum unsmoothed cross correlation coefficient at 0 lag for the calibration measurements was of .49 and with 30 point boxcar the coefficient was of .85.

3.2.2 Littoral region

For the HOPA VIPh experiments, since the geometry and the environment were radically different to the more controlled rooftop calibrations, we decided to check again the calibration of the instruments. The instruments were located in the same antysimetric position between transmitter and receivers as with the top of the Physics Building; this time the beams propagated about 1.5 meters above the surface of the water for almost 600 meters.

Data was collected over 24 hours from which we were able to collect almost 19 hours of contiguous good data with which to analyze the correlation between the signals.

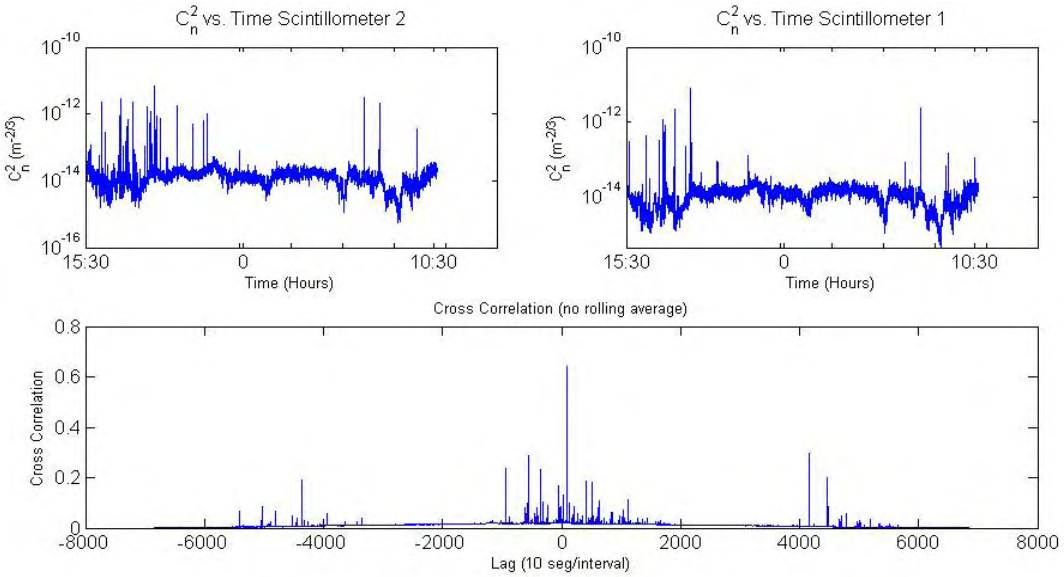

Figure 3.6: September 3 & 4 2006. C_n^2 data from the Scintillometer 2 and Scintillometer 1 are plotted on the top graphs respectively, this is the raw data. The bottom graph correspond to the cross correlation between the two signals.

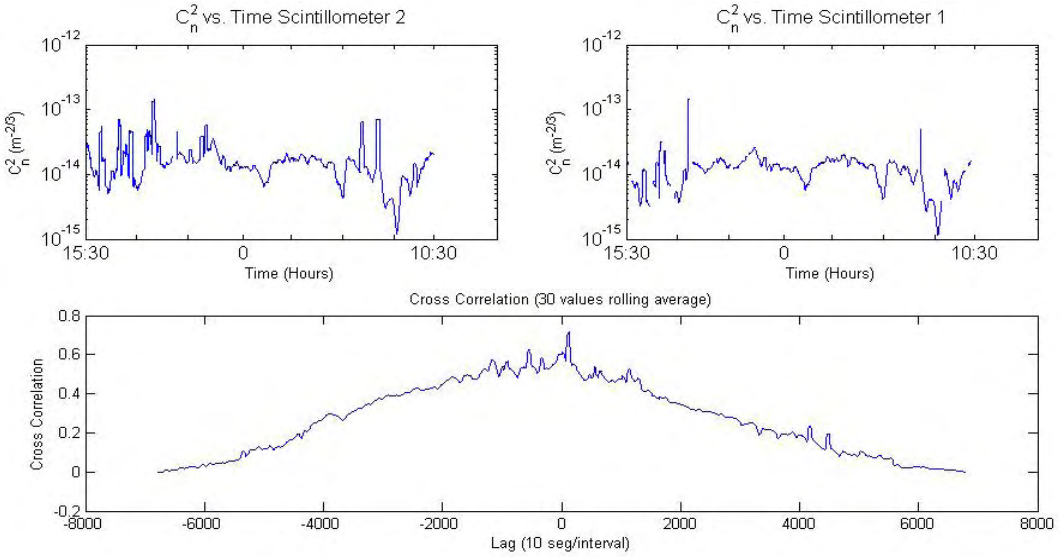

Figure 3.7: September 3 & 4 2006. C_n^2 data from the Scintillometer 2 and Scintillometer 1 are plotted on the top graphs respectively, this is with a 30 value rolling average. The bottom graph correspond to the cross correlation between the two signals.

Figure 3.6 & 3.7 shows the data for calibration over the water collected between September 3 and September 4, 2006 at La Parguera, Lajas, and Puerto Rico. Figure 3.6 show the data without any smoothing and figure 3.7 shows the same data with a 30 point rolling average (5 minutes) and its correlation respectively. Once again it is clear how smoothing the data helps to improve the correlation between the signals for the slower oscillations that interest us in the study. Figure 3.8 shows the comparison of the autocorrelation as a function of boxcar width for both calibrations runs. In both cases we can observe how smoothing the data improve the correlation between the signals, but with rolling averages greater than 30 values (5 minutes) this correlation exhibits a strong asymptotic behavior.

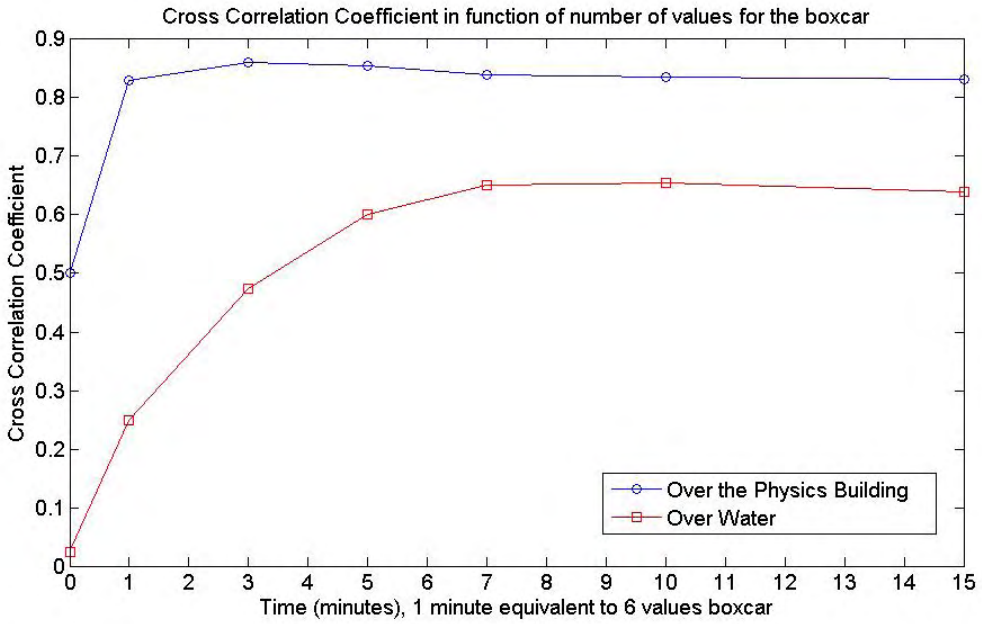

Figure 3.8. Cross correlation coefficients. (Red line: Calibration over Water (September 4 2006), Blue Line: Calibration over Physics Building (February 28 2006)).

The raw cross correlation coefficient for the 19 hours data set collected over water is .025 while with a 30 value boxcar smoothing it is of .60. For the 24 hours data set collected over the Physics Building the cross correlation coefficient at 0 lag for the raw data is of .5 while with a 30 point boxcar smoothing it is .855.

3.3 Calibration Conclusion

The data confirms that the instruments perform very similarly, so that we can confidently perform simultaneous experiments at distinct locations and with different experimental geometries.

Also figure 3.8 shows which number of values for a rolling average it will be better for smoothing our data and keep the precision between the instruments. For both calibrations experiments under completely different conditions is showed how a smoothing 5 minutes in the time vector is the optimal to keep that precision.

Chapter 4: Experiments

For the development of this work multiple experiments at different locations were carried out. All of them followed the same objective of collect as much data as possible with variable weather parameters and geographical conditions. During each campaign we confronted different complications which limited that amount of data collected. The weather conditions was one of the principal affecting factors along all the experiments due strong rains, thunder storms or strong winds which misalign the systems. Under some thunderstorms, or strong rains it was necessary to stop the experiment for protection of the electronic equipment like the computers which control and save the data take by the instruments. During the next sections the difference between each experiment campaign will be discussed.

The alignment process for this equipment at each experiment location consist in being able to collocate the transmitter beam with the receiver aperture between a minimum distance of 100 meters and no more than 2000 meters, as recommended by the manufacture. However we show that less than 100 meters can be obtained by neutral density filters (see section 4.1). Once they are in position the finder telescopes located at the top of each instruments can be used to better the first alignment. After the equipment is on and the SQC data collection software has been set-up following the instructions provided, the software can be run in a setup or alignment mode. The set up shows the voltage value corresponding to each receiver channel. A good alignment process consists in changing the direction of the transmitter and the receiver using the micrometer screws on the tripods and ensuring the detector voltage values are as close as possible one to the other, preferably no more than .1

volt the difference between them and over the 2.5 volt threshold value for each channel. Each channel should not be under .3volts or higher than 3 volts to be considered as a good data. The power of the LED on the transmitter can be adjusted as necessary, depending in the distance of the setup.

4.1 Physics Building, UPRM, Experiment

The UPRM Experiment was undertaken during the 2006 spring for seven weeks. The main purpose of this experiment was to cross check the relative calibration of the systems but it also provided a large amount of landbound weak scintillation data. Figure 4.1 shows more specifically the setup of the experiment on the top of the Physics Building. The separations between the transmitters to the receivers were approximately 90 meters. Because of the short distance it was necessary to use neutral density filters at the receivers to attenuate the intensity of the incoming beam light and not saturate the receiver channels. The filters

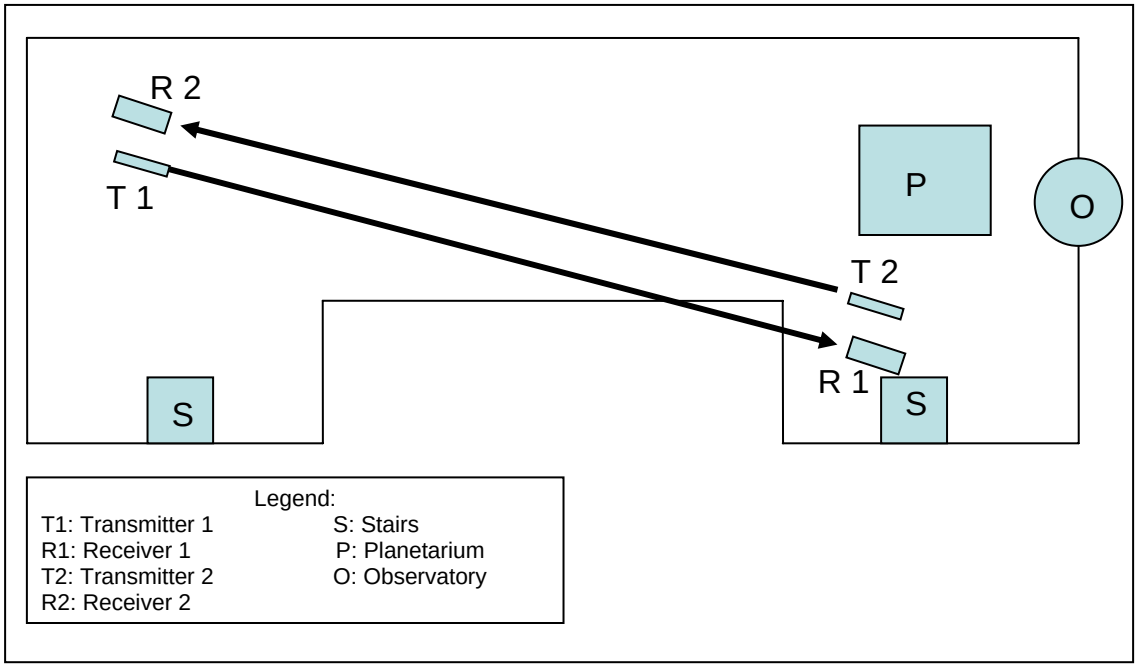

Figure 4.1: Sketch of the Experiment at the top of the Physics Building (UPRM Exp). Distance or propagation between the systems 90 meters approximately (draw not at scale).

were constructed using metallized electrostatic discharge film used to package sensitive electronic components. This film consists of an inner layer of polyethylene, an outer layer of polyester and a sandwich layer of aluminum, which allows for about a 40% transmission in the visible and approximately 20% in the near infrared.

A Davis Pro Weather Station was placed on the roof of the building, but due to technical problems with the control box of the weather station it was not possible to recover that data. Conveniently close to the building, around 100 meters separation, is located a weather station administrated by the Climate Center at the University of Puerto Rico in Mayagüez. This weather station collects data every 10 minutes and can be accessed through the webpage http://atmos.uprm.edu/.

4.2 Chesapeake Bay Detachment, Experiment

The Chesapeake Bay Detachment (CBD) is a research facility of the Naval Research Laboratory located right on the Chesapeake Bay, MD. This site was originally selected for the experiment due the closeness to the bay and it relative isolation, allowing for minimal human intervention in the experiment.

For the CBD Experiment scintillometer #1 was employed only. The transmitter was positioned approximately 20 feet from the edge of a cliff where a receiver was placed in front of a building. The distance of between the transmitter and the receiver was 110 meters approximately mostly over a grassy area. The weather station, a Davis Vantage Pro plus was located close to the receiver over the grassy area.

Figure 4.2: Aerial view of the Chesapeake Beach Detachment of the Naval Research Lab in Chesapeake Beach MD, US.

This experiment ran over a period of two years, 2003 and 2004, to collect data over the four different seasons of the years. As described before the Scintillometer took data every 10 seconds and the weather station collected data every 5 minutes. During that campaign numerous difficulties were found since the Scintillometer needed to be constantly monitored as it would misalign easily; strong winds were the principal reason for the misaligning of the system [14].

Figure 4.3: View of the area where the CBD experiment was performed.

4.3 Magueyes Island, HOPA VIPh Experiment

HOPA VIPh Experiment (HOrizontal PAth propagation over the water from the Villa Parguera hotel) was a 3 week campaign during the end of the summer of 2006. For this experiment both Scintillometers and two Davis Vantage Pro plus weather stations were employed. The experiment was conducted between the Hotel Villa Parguera in Lajas Puerto Rico and Isla Magueyes, a research facility of the Marine Science Department of the University of Puerto Rico, Mayagüez Campus.

Scintillometer #1 was located between the roofs of the hotel building and the roof of the main building on Isla Magueyes as appreciate in figure 4.5. Transmitter #1 was at an altitude of 6 meters approximately versus the receiver #1 at 15 meters altitude approximately over the top of the building in Magueyes Island. Scintillometer #2 was collecting data at low altitude, 5 feet approximately over the water level at each side, transmitter and receiver as observed in figure 4.6. This one was located between the dock at the mentioned hotel and

Figure 4.4: Aerial view of the experimental site and representations of the propagations paths between Villa Parguera hotel and Magueyes Island.

one of the docks at the back sides of Magueyes Island, to complete the 580 meter propagation path just over the water as a difference of with the other system which has approximately 80 meters of land under the propagation path.

This campaign was designed with this geometry to compare data collected at different altitudes and over different propagation paths: over water and over a mix terrain. Also two weather stations were used, one in each receiver. The weather station with the receiver #2 was collecting data each 1 minute and the one in Magueyes Island, close to the receiver #1 was collecting data each 30 minute. Data from the weather station located at Magueyes Island provided by Yaítza Luna, and is available to the public at http://physics.uprm.edu/~yaitza.

(a) (b)

Figure 4.5: (a) View of the transmitter at the top of the hotel, (b) view of the receiver at from the top of the building in Magueyes Island.

(a) (b)

Figure 4.6: (a) Transmitter located at the dock in Magueys Island, (b) view of the receiver located at the dock in Villa Parguera hotel.

(a) (b)

Figure 4.7: (a) Weather Station located with the Receiver #2 at the hotel, (b) weather station located at the Receiver #1. This weather station is administrated by Yaítza Luna.

Chapter 5: Experiments Results

5.1 Data Analysis Methods

MATLAB has been used as the principal data reduction and data analysis platform. Different methods of analysis have been implemented, including correlograms and the calculation of the cross-covariance between different variables of interest. Some of these methods are most effective when used with stationary data; as a consequence a way of achieving this stationarity condition had to be defined and implemented. Stationary data are the data in which the ensemble mean of a subset of the series is equal to the mean of the overall series. We begin by describing a recently developed algorithm which allows us to satisfy the requirement of stationarity.

5.1.1 Empirical Mode Decomposition (EMD)

The *Empirical Mode Decomposition* (EMD) is a new technique pioneered by N. E. Huang *et al.* [16] for representing non-stationary signals. The EMD method is an adaptive decomposition of the data, which results in the extraction of so called Intrinsic Mode Functions (IMFs). The IMFs have well prescribed instantaneous frequencies, defined as the first derivative of the phase of an analytical signal. The algorithm for this technique summarized by G. Rilling [15] as:

1. find all extrema in the signal $x(t)$
2. interpolate between the minima and between the maximas, ending up with some envelope $e_{min}(t)$ & $e_{max}(t)$
3. compute the mean $m(t) = (e_{min}(t) + e_{max}(t))/2$
4. extract the detail $d(t) = x(t) – m(t)$

5. iterate on the residual *m*(t).

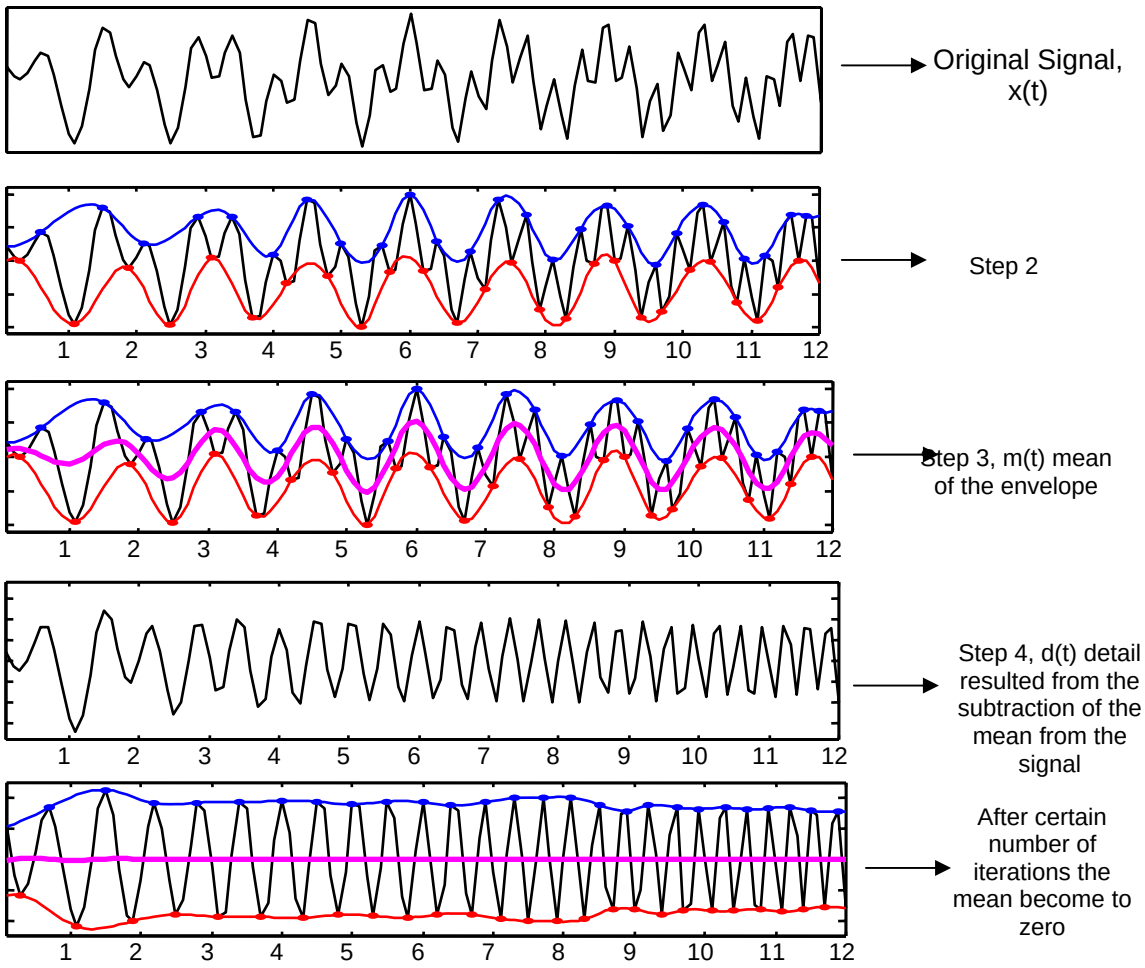

Figure 5.1: This figure show the basic algorithm for the EMD method described in the text. The graph at the top shows the original signal. In the second graph we represent ate how the envelopes are created interpolating between the all the maxima and all the minima. In the third one representing the step 3 describe in the text where the mean is calculated. The graph number 4 shows the residue of the subtraction of the mean. The processes it will be repeated between the steps 2 and 4 until the mean calculated become to zero as seen in the graph at the bottom.

This procedure between step 1 to 4 is repeated until the detail signal *d*(t) is considered have a zero mean. Once this criteria satisfied this signal *d*(t) is know as one IMF. Then the residual is computed and step 5 applies. Figure 5.1 shows the IMFs of a time series signal.

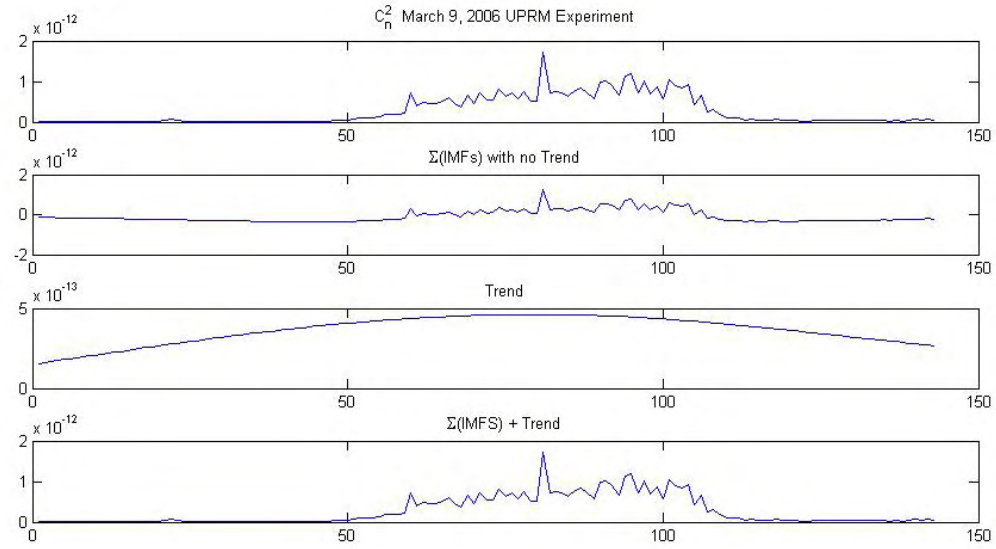

Figure 5.2: C_n^2 data corresponding to March 9, 2006, smoothed with a 30 value rolling average (top graph). In the second graph is showed the sum of all the IMFs calculated without add the trend. The third plot show the trend which was subtracted from the data in the second plot. The bottom plot is the sum of all the IMFs including the trend to regenerate the original data. The reconstruction error was of the order of 10^{-14} %.

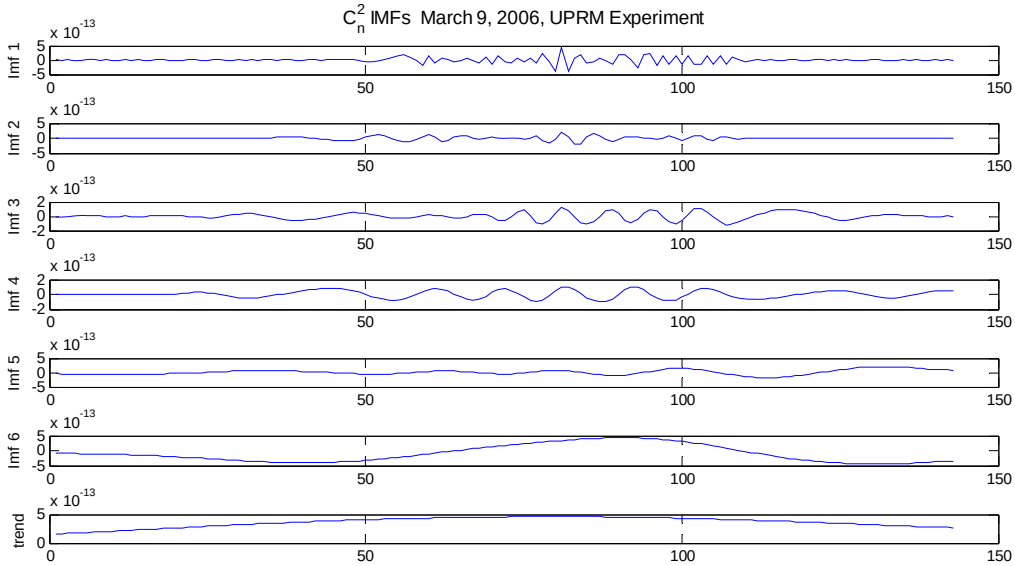

Figure 5.3: IMFs calculated for the C_n^2 data collected on March 9, 2006 at UPRM Exp. The C_n^2 data was smoothed with a 30 value rolling average before extring the IMFs. The bottom-most graph is the residual after removing all the IMFs and represents the overall trend.

The IMFs generated from a signal obey the additive law, within the bounds of numerical error. For the example shown in Figure 5.2, summing the IMFs and the trend line generates a signal that has a relative error in the order of 10^{-14} % with respect to the input time series. Therefore we can add the different IMFs leaving out the last one, called the trend. Leaving the trend out we are eliminating the influence of the lowest oscillation from our data and this will give a stationary resultant as its mean will be zero, allowing the application of different statistical methods for the analysis.

We should also note that the individual IMFs seem to have characteristic timescales, which may be related to external physical effects.

5.1.2 The Analytical Signal

Gabor [18] defined the complex analytical signal, namely

$$\Psi(t) = X(t) + iY(t) \qquad (1)$$

where

$$Y(t) = H[X(t)] \qquad (2)$$

$$= \frac{-1}{\pi} P \int_{\Omega} \frac{X(t)}{(s-t)} ds, \qquad t \in \Omega \qquad (3)$$

where H[●] represent the Hilbert Transform. As a result ψ(t) is an analytical signal. The Hilbert Transform is a Cauchy Principal Integral, which we denote by *P*, An alternative way of writing this is

$$\Psi(t) = a(t) \exp^{i\Phi(t)} \qquad (4)$$

where

$$a(t) = \sqrt{X^2(t) + Y^2(t)} \qquad (5)$$

$$\Phi(t) = \arctan\left(\frac{Y(t)}{X(t)}\right) \qquad (6)$$

This de Moivre form of the analytical signal is similar to the Fourier amplitude and phase expression. Note that the Hilbert amplitude and phase are time dependent, opposed to the Fourier analysis. It is this specific advantage over Fourier analysis that motivates us to consider the less well known Hilbert transform over Fourier techniques in what follows.

5.1.3 Hilbert Phase Analysis

Applying the Hilbert Transform directly to a time varying signal can result in some uninterpretable results due the number of paradoxes attributed to the existence of "riding waves" in the data. This problem can be avoided by applying the Empirical Mode Decomposition (EMD) method, see [11]. The algorithm for this HPA method consists basically of three steps:

1. obtaining the IMFs and trend lines of the original signal.
2. add the different IMFs and apply the Hilbert Transform
3. calculate the phase angle of the Hilbert Transformed IMFs.

The Intrinsic Mode Function (IMFs) obtained from the application of the EMD method have well defined instantaneous frequencies given by

$$w(t) = \frac{d\Phi(t)}{dt}. \qquad (7)$$

5.2 Experiments Results

5.2.1 CBD Experiment

The C_n^2 data for this experiment collected over the 2 year campaign at the CBD was smoothed with a 30 point rolling average. For this analysis we chose data sets under certain weather characteristics, which allow us a better analysis and study of the C_n^2 behavior with the weather parameter of our interest, the humidity. The data was selected by (Appendix B):

- temperature variation no more than 15%
- pressure change no more than 15 mbars
- exclusion of snowing and raining days
- wind speed/direction constant.

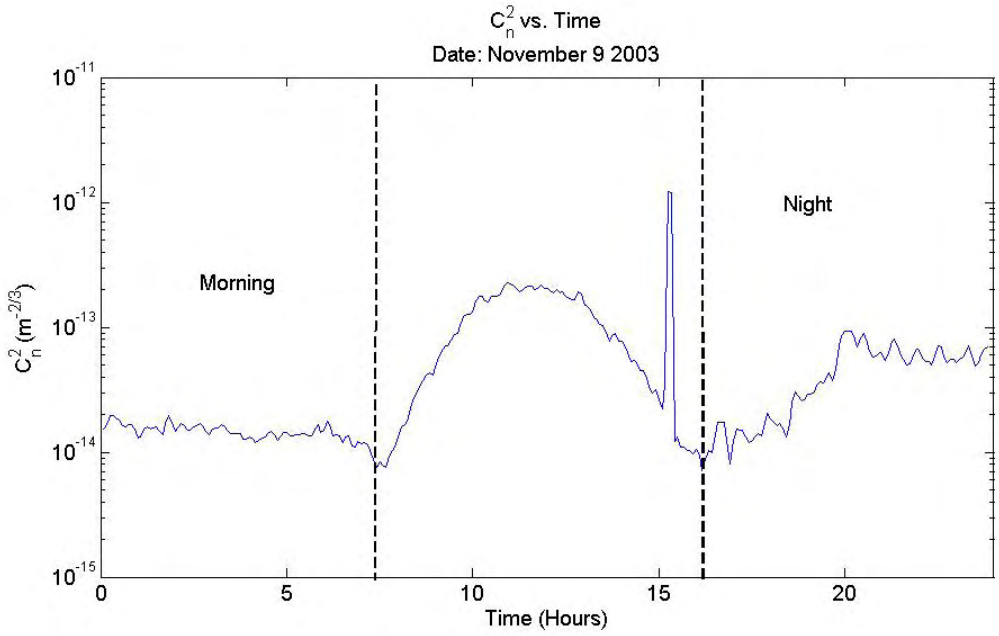

Figure 5.4: C_n^2 data from the CBD experiment on November 9 2003. In this graph we show the sections of the data that we call morning and night for purpose of our analysis.

Due to the state-of-the-art premise that the C_n^2 behavior will be dominated by the temperature trend, which we assume for most clear days to be strongly influenced by the

solar radiation, just data sets during presunrise (morning) and postsunset (night) times were selected to study the fluctuations over the C_n^2 data. This allows us the latititude to study the humidity and other secondary effects. For that purpose the data was separate by morning and night sections as seen in figure 5.4.

Date	**Min RH (%)**	**Max RH (%)**	**Δ RH (%)**	**Min Temp (˚F)**	**Max Temp (˚F)**	**Δ Temp (˚F)**	**Δ C_n^2**	**C_n^2→Temp**	**C_n^2→1/RH**
Nov 03 2003 morning	74	89	15 (+)	64.09	66.2	2.1 (+)	(-)		X
Nov 09 2003 morning	42	57	15 (+)	38.86	40.28	1.4 (-)	(-)	X	X
Nov 10 2003 morning	63	74	15 (+)	30.7	33	2.3 (-)	(-)	X	X
Feb 2 2004 morning	81	100	19 (+)	28.1	30.6	2.5 (+)	(-)		X
Mar 27 2004 night	71	82	11(-)	43.9	51.9	8(-)	(+)		X
Mar 28 2004 morning	75	87	12 (+)	48.5	55.7	7.2 (-)	(-)	X	X
Apr 3 2004 morning	72	90	18 (+)	42.3	48.2	5.9 (-)	(-)	X	X
Apr 3 2004 night	35	49	14 (-)	37.5	43.1	5.6 (-)	(+)		X

Table 5.1: Statistical values for the analyzed cases from CBD experiment. The minus (-) and plus (+) symbols represents if the gradient of the trend of the data was decreasing or increasing respectively.

After the selection of the data collected, 8 cases between November 2003 and April 2004 were extracted from the total set. Table 5.1 show for each of the cases selected the maximum and minimum values for temperature and relative humidity. In the table, the minus (-) and the plus (+) symbols represent the gradient of the trend of the data.

Comparing this for each day we can observe that just in 4 of the 8 cases the temperature-relative humidity inverse relationship assumption of standard, simplistic meteorology is contravened. This inverse relationship is claimed assuming that the moisture in the atmosphere is constant over the whole time period of the measurements. Since the temperature was mostly constant, with minimal fluctuation compared to the relative humidity changes, we can interpret that the amount of moisture in the atmosphere varied over the time interval of measurements.

However an inverse relationship between the relative humidity and the C_n^2, as reported by Oh et al. in 2004[14], has been confirmed in all 8 cases studied here (last column), as we can see by examining the correlograms between the two measured functions, Figure 5.5, which show negative gradient, see appendix A for more data sets(pages 53-56). Supplementing this evidence are the cross-covariance graphs between both time series vectors for each case.

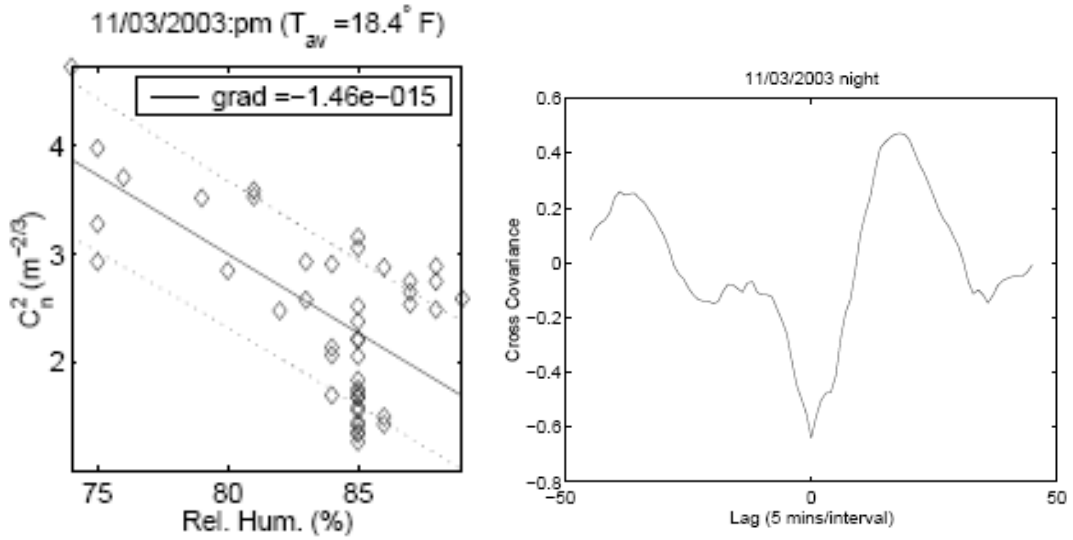

Figure 5.5: November 3 2003, night. Correlogram (left), Cross-Covariance (right).

Data set number	Date [mm/dd/yyyy]	Zero timelag cross covariance
1	11/03/2003 night	-0.6397
2	11/09/2003 morning	-0.6144
3	11/10/2003 morning	-0.7632
4	02/02/2004 morning	-0.6251
5	03/27/2004 morning	-0.2930
6	03/28/2004 morning	-0.5764
7	04/03/2004 morning	-0.5604
8	04/03/2004 night	-0.4374

Table 5.2: Values of the cross covariance coefficients at zero lag to their respective data sets.

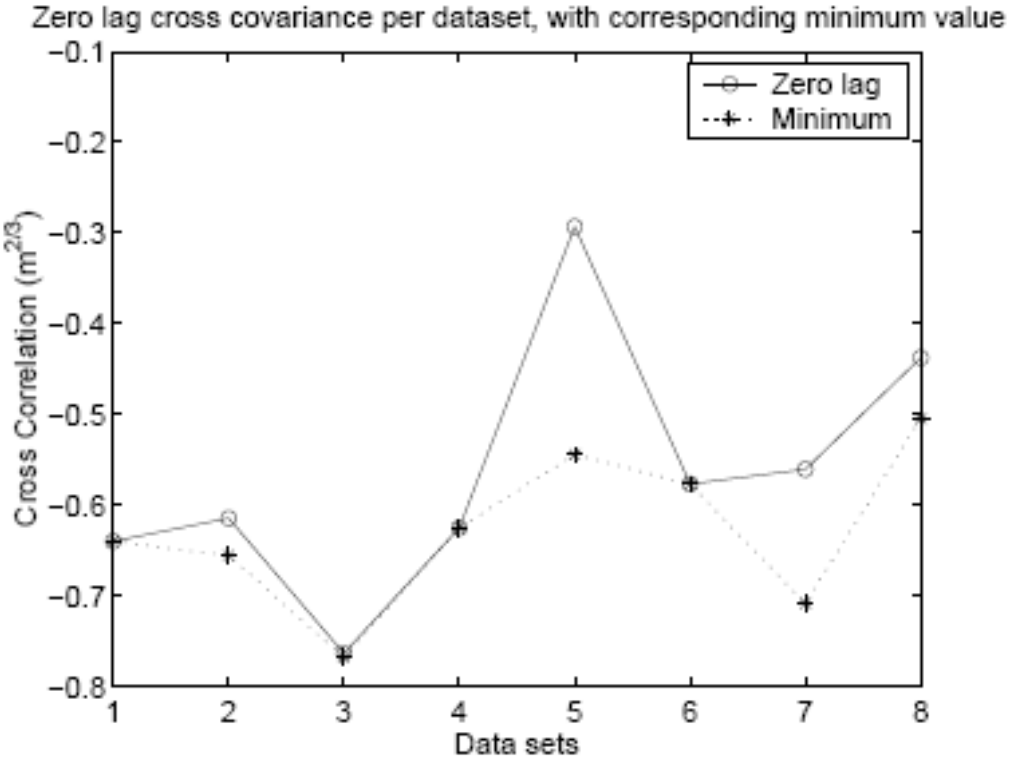

Figure 5.6: Plot comparing the minimum coefficient with the value of the coefficient at the 0 lag.

Each of this figure show similar behavior, a negative gradient in each of the correlograms presented and a negative cross-covariance coefficient at zero lag as presented in table 5.2. Figure 5.6 show a plot of the cross-covariance coefficients at zero lag and the

minimum coefficient value. Most of the cases the minimum coefficient is at the zero lag or close to it, which mean that the influences of the humidity upon the C_n^2 was very close in time (5 minutes per sample).

The HPA method was also applied to the same 8 cases, as a first test of the effectiveness of this method. In figure 5.7 we observe the plots of the HPA method applied to the data, see Appendix A for more examples (pages 63-70). Each figure, which consists of 6 plots, is organized in the following order:

- phase angle of C_n^2 (top left)
- phase angle of temperature and relative humidity (top center)
- average of the phase angle between temperature and relative humidity (top right)
- difference of the average between the phase angle of the weather variables from the phase angle of the C_n^2 (bottom left)
- difference of the phase angle of relative humidity from the phase angle of the C_n^2 (bottom center)
- difference of the phase angle of temperature from the phase angle of the C_n^2 (bottom right)

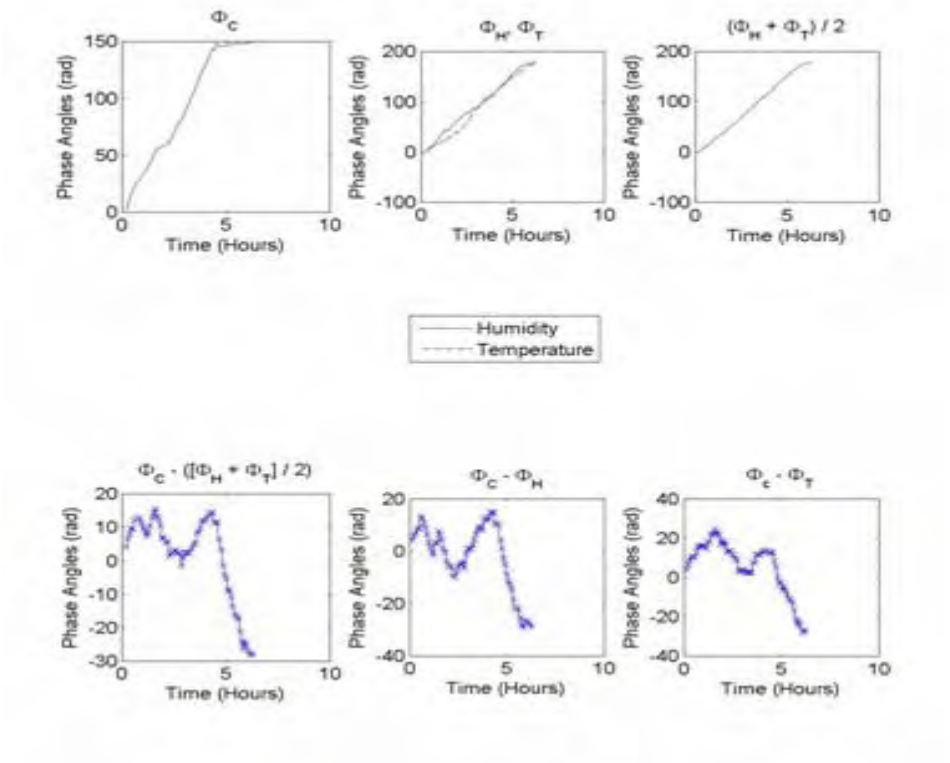

Figure 5.7: March 28 2004, morning. At the top (right) the HPA of the C_n^2, (center) the HPA corresponding to the relative humidity and temperature, (left) the average between the HPA of the temperature and the HPA of the relative humidity. At the bottom (right) the subtraction of the average of the HPA from the C_n^2 HPA, (center) the subtraction of the relative humidity HPA from the C_n^2 HPA, (left) the subtraction of the temperature HPA from the C_n^2 HPA.

After comparing the difference of the phase angles of temperature and relative humidity from the phase angle of C_n^2 we can observe which one conserve the same kind of fluctuations that the plot of the subtraction of the average of the phase angles between relative humidity and temperature from the phase angle of C_n^2, concluding that:

- November 3, 2003 (night): Temperature dominate the C_n^2 behavior
- November 9, 2003 (morning): Not clear which weather parameter dominate C_n^2
- November 10, 2003 (morning): Temperature dominates.
- February 2, 2004 (morning): Not clear which weather parameter dominate C_n^2
- March 27, 2004 (night): Temperature dominates

- March 28, 2004 (morning): humidity dominates
- April 3, 2004 (morning): temperature dominates
- April 3, 2004 (night): humidity dominates.

5.2.2 UPRM Experiment

This experiment was used for the calibration of the two scintillometer instruments, as well as for further testing of the HPA method. From the campaign we were able to extract 6 days where 100% of the data were good values, as defined by the parameters established by the equipment. As a first indicator of how the HPA can describe the behaviors of a time

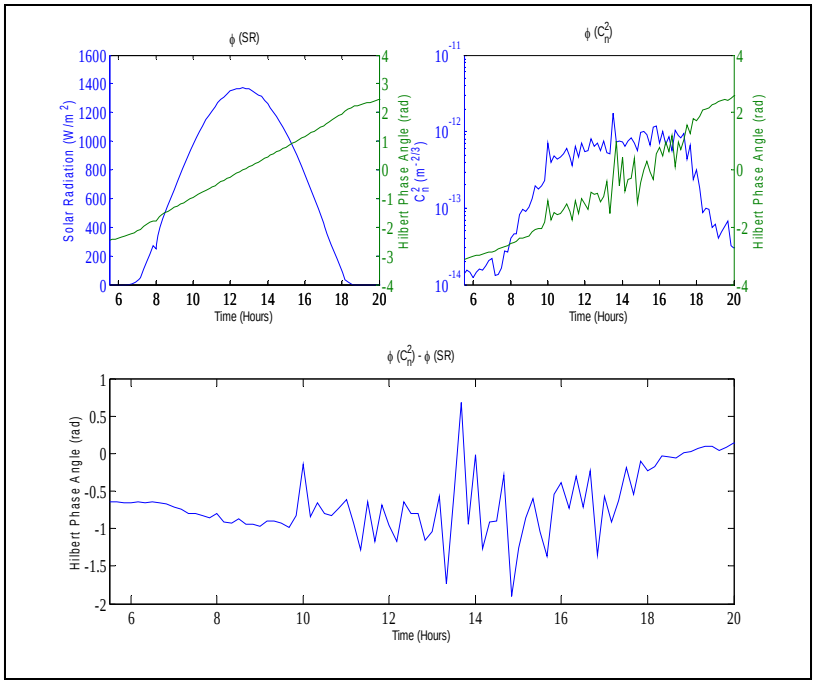

Figure 5.8: March 9, 2006, UPRM Experiment. (top right) Solar radiation data with its HPA over plotted. (top left) C_n^2 data with its HPA over plotted. At the bottom the difference of the solar radiation HPA from the C_n^2 HPA.

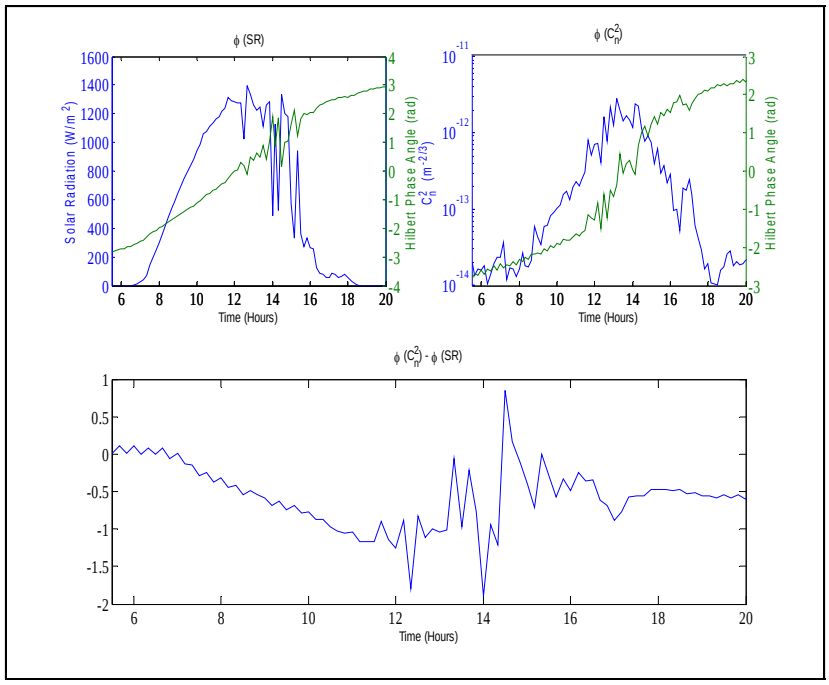

Figure 5.9: March 7, 2006, UPRM Experiment. (top right) Solar radiation data with its HPA over plotted. (top left) C_n^2 data with its HPA over plotted. At the bottom the subtraction of the solar radiation HPA from the C_n^2 HPA.

series we use the solar radiation and the C_n^2 data. Figure 5.8, at the left (top) show the corresponding data for the solar radiation for March 9 2006 and the Hilbert Phase angle calculated. At the right (top) is plotted the C_n^2 data with it Hilbert Phase angle. It is clear that the difference between both plots, where the solar radiation was completely smooth, indicating that for a sunny day the HPA results in a smooth line with a constant gradient, although there are some significant changes in the gradient corresponding to the sunrise and sunset times. Also we can observe how the HPA indicates not just the slow oscillations in the data, also the fastest oscillations like is the case of the C_n^2 HPA at the top right of the plot. The HPA of the solar radiation was subtracted from the HPA of the C_n^2 showing as a result a horizontal line close to zero value with small amplitude oscillations. This verifies strongest influence of the solar radiation over the C_n^2 over land.

To study the influence of the different weather parameters over the C_n^2 a cross-correlation was applied to the Hilbert phase angles calculated along a 24-hour time period. Figure 5.10 corresponding to March 9 2006 show a clear positive cross covariance between the solar radiation and temperature. This demonstrates the direct relation between these two variables along a sunny day. Cross covariance between C_n^2 and temperature, relative humidity and solar radiation where calculated. The cross covariance for the temperature and solar radiation with C_n^2 respectively show a positive relationship between them, as expected due the positive cross covariance between the solar radiation and temperature and an inverse relationship between the C_n^2 and the relative humidity is present in the data. Figure 5.11 show the data collected in February 28 2006, this data show a positive correlation between the C_n^2 and solar radiation at the same time that show an inverse relationship of the C_n^2 with

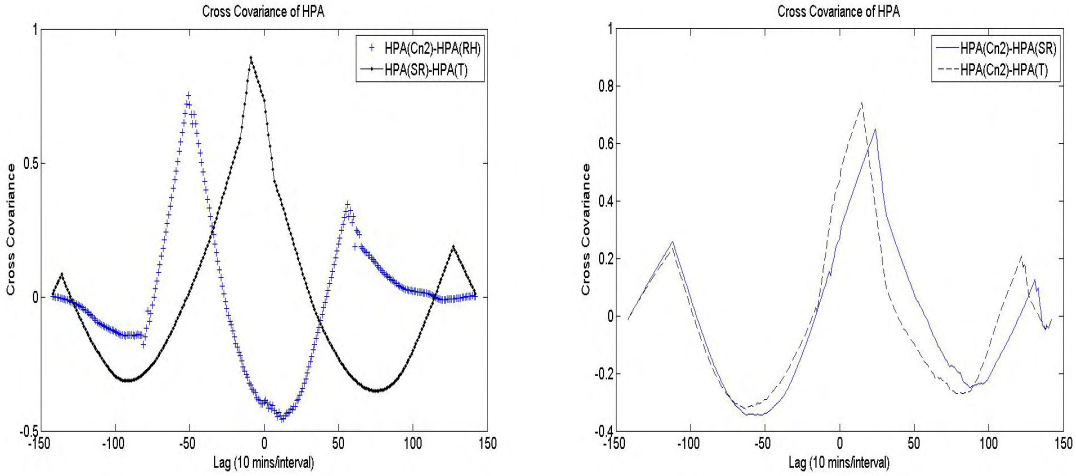

Figure 5.10: March 9, 2006. (Left) Cross covariance between the HPA(C_n^2) with HPA(RH) and between HPA(SR) with HPA(T). (Right) Cross covariance between the HPA(C_n^2) with HPA(SR) and between HPA(C_n^2) with HPA(T).

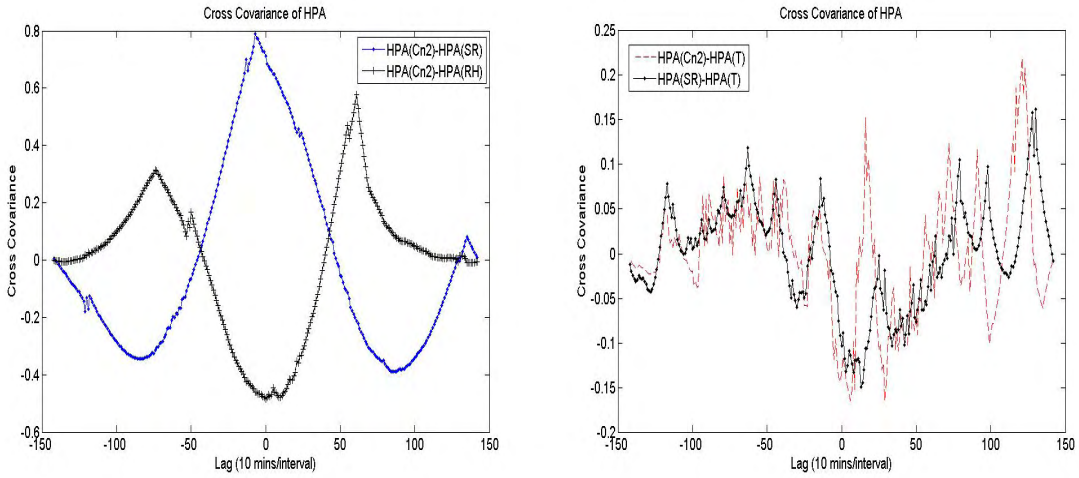

Figure 5.11: February 28, 2006. (Left) Cross covariance between the HPA(C_n^2) with HPA(RH) and between HPA(SR) with HPA(SR). (Right) Cross covariance between the HPA(C_n^2) with HPA(T) and between HPA(SR) with HPA(T).

the relative humidity. During this day we can observe how the relationship between the solar radiation and temperature is completely lost and the relation between temperature and C_n^2 is also lost. Indicating that more factors were affects the system. Even with this loss of relationships the inverse relationship between the C_n^2 and relative humidity still present.

5.2.3 HOPA VIPh Experiment

During this campaign C_n^2 data was collected over a .5 km propagation path. The other notable difference was that this data was collected over water. Once the data was filtered using the statistical values provided by the Scintillometer was plotted, as shown in figure 5.12. The C_n^2 data on the solid line correspond to the system located between the docks. It was observed that each of the large amplitude peaks in the data was produced by the boats passing close to the propagation path. The data from the other instrument was over plotted.

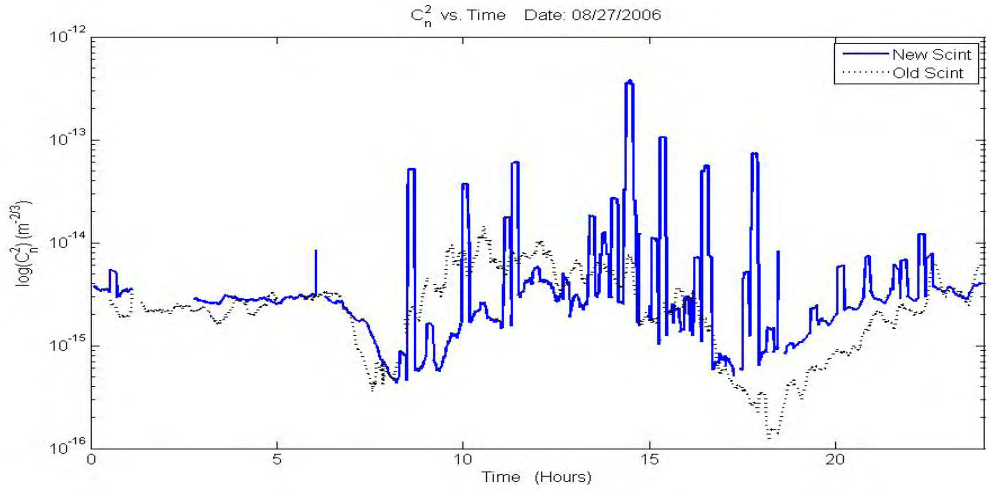

Figure 5.12: August 27, 2006. C_n^2 data for both Scintillometer over a 24-hours time period.

From this experiment two days of data were selected to apply the Hilbert Phase Analysis. These days were selected because each one presents more than 95% of good data in

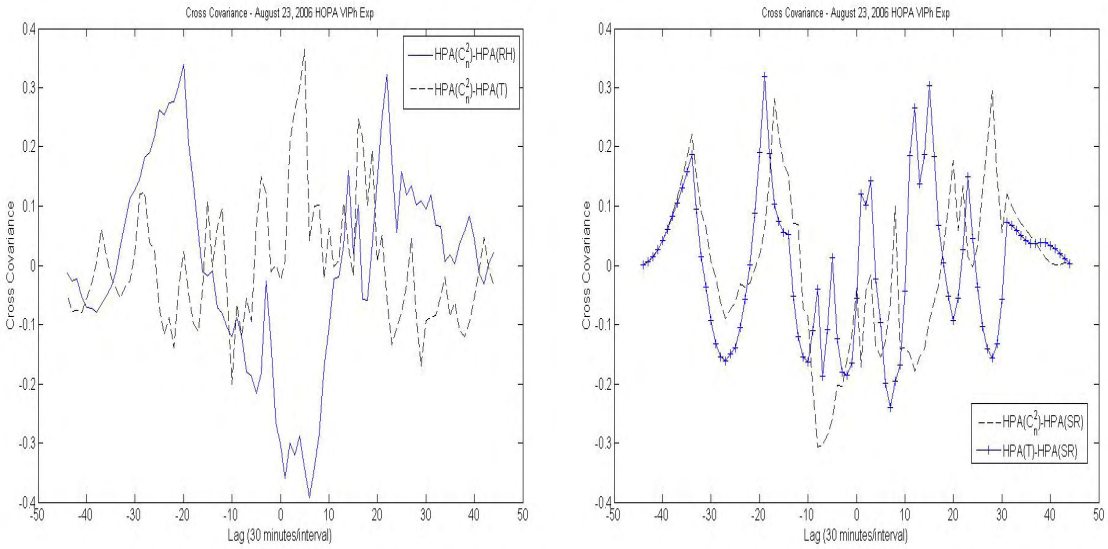

Figure 5.13: Cross Covariance of HPA for the New Scintillometer with the weather conditions collected by the weather station located at Magueyes Island. Data collected on August 23, 2006. Statistical values indicate that 99.98% of the C_n^2 data was good data.

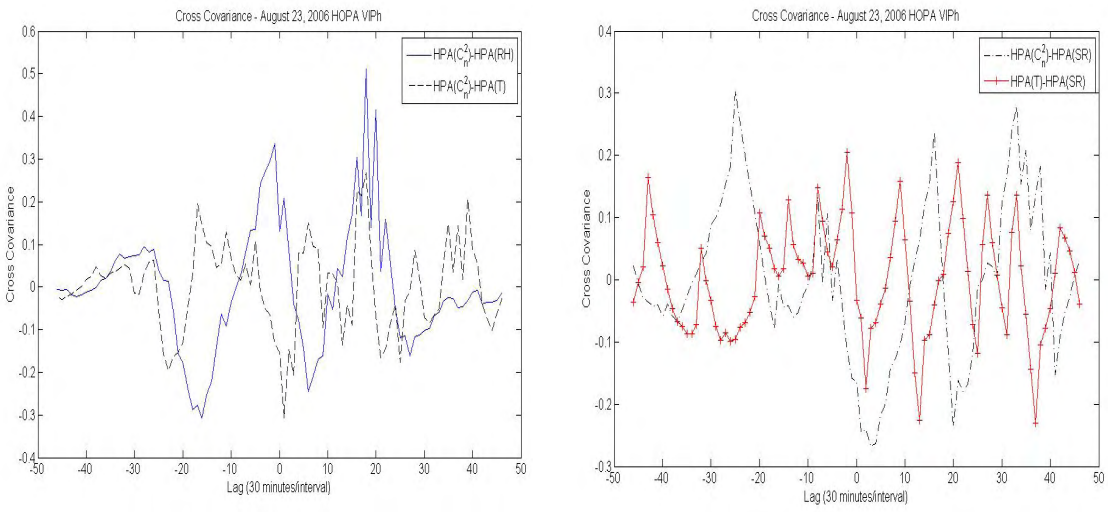

Figure 5.14: Cross Covariance of HPA for the Old Scintillometer with the weather conditions collected by the weather station located at Magueyes Island. Data collected on August 23, 2006. Statistical values indicate that 95.7% of the C_n^2 data was good data.

their statistical values for each system, also for availability of the good weather data along a 24-hour period. August 23, 2006 presented in figure 5.13 and figure 5.14 for Scintillometer #2 and for Scintillometer #1, respectively, shows the consistency on our method in illustrating the different kind of relations that exist between the different weather parameters and the C_n^2 parameter. The cross correlation zero lag coefficient clearly shows the relationship between the C_n^2 data and the Relative Humidity. In figure 5.13we show the inverse relationship between these two variables, although in figure 5.14 the relationship of these two variables, the C_n^2 with the relative humidity appears to be positive. This difference in this latter cross covariance may have been produced by other weather parameter affecting one of the systems, by example the wind, which is know it have some influence over the C_n^2 behavior but is not part of this study.

What is important to notice in both plots is that the cross covariance between the C_n^2 and the relative humidity and the cross covariance between the C_n^2 and the temperature is

opposite and consistent in both systems. Relationships showed by the cross covariance of other variables like the C_n^2 with the solar radiation or between the solar radiation and temperature can be lost due the instability in the weather conditions during these days in the experiment area. These weather conditions include very cloudy days and windy days. During August 27, 2006 it was also possible collect good data on both systems. Data from the weather station located at the dock of Villa Parguera Hotel was used for the analysis because the data from the weather station at the islet was not available for this day. In figure 5.15 we can observe the same behaviors observed in the data from August 23, 2006. Most of the different relationship showed by the cross covariance of the HPA are lost or in a minor scale than the ones observed in the UPRM Experiment data. But once again the HPA

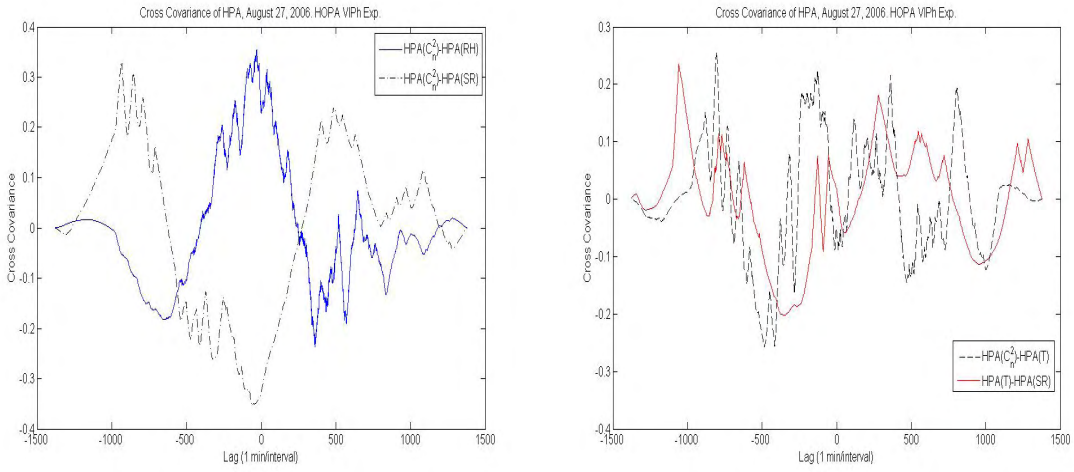

Figure 5.15: Cross Covariance of HPA for the New Scintillometer with the weather conditions collected by the weather station located at the Hotel. Data collected on August 27, 2006. Statistical values indicate that 99.99% of the C_n^2 data was good data. (Left) Cross covariance between the HPA(C_n^2) with HPA(RH) and between HPA(C_n^2) with HPA(SR). (Right) Cross covariance between the HPA(C_n^2) with HPA(T) and between HPA(SR) with HPA(T).

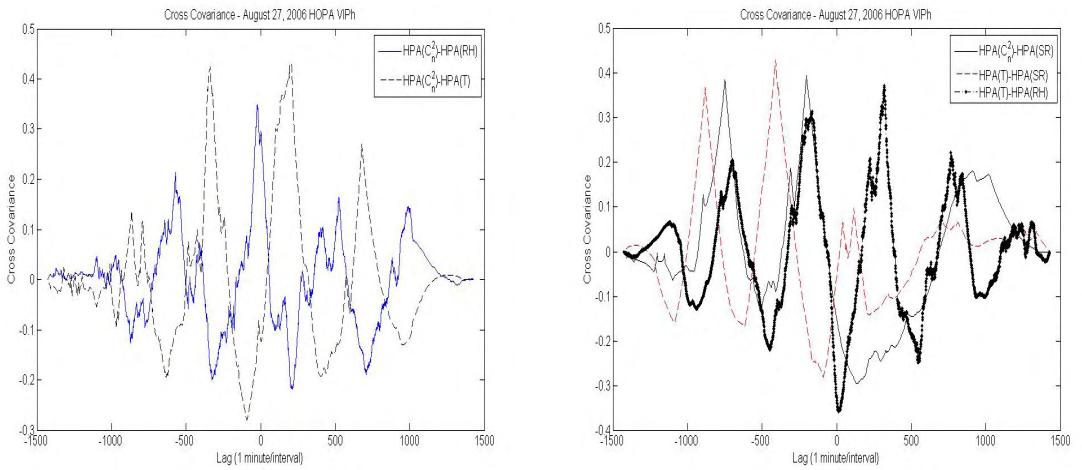

Figure 5.16: Cross Covariance of HPA for the Old Scintillometer with the weather conditions collected by the weather station located at Hotel. Data collected on August 27, 2006. Statistical values indicate that 96.67% of the C_n^2 data was good data. (Left) Cross covariance between the HPA(C_n^2) with HPA(RH) and between HPA(C_n^2) with HPA(T). (Right) Cross covariance between the HPA(C_n^2) with HPA(SR), between HPA(SR) with HPA(T) and between HPA(RH) with HPA(T).

method reveals a relationship between the C_n^2 and the relative humidity. In this plot this relation is a positive one, but the relation between the C_n^2 with the temperature and with the solar radiation respectively is negative. This confirms the direct influence between solar radiation and temperature and the same time that confirm the inverse relationship between the relative humidity and the temperature, demonstration the capabilities of our HPA method. Figure 5.16 which correspond to the data of the Old Scintillometer for August 27, 2006 too collaborate what was just describe from figure 5.15.

Once the data of the 3 experiments was reduced we were able to make some comparison of the crude C_n^2 data. Figure 5.17 show C_n^2 data set from each experiment discussed in this chapter, plotted as a function of time for a 24 hours period. Table 5.3 shows the principal characteristics which distinguish each experiment. It is clear how the turbulence that was mostly over the water keep always a lower order of magnitude than the other

	CBD Experiment	UPRM Experiment	HOPA VIPh Experiment
Distance of propagation	≈ 100 meters	≈ 90 meters	≈ 600 meters
Surface	Grassy area	Over roof of a building	Around 86% over water, 14% over land
Altitude respect the surface	1.5 meters	1.5 meters	≈10 meters

Table 5.3: Principal differences between the 3 experiments.

systems, been this a possible indication of the effects of presence of humidity along the propagation path. It is also notable how the similitudes between the three sets of data were they show a minimum close to the sunrise and other minimum around the sunset.

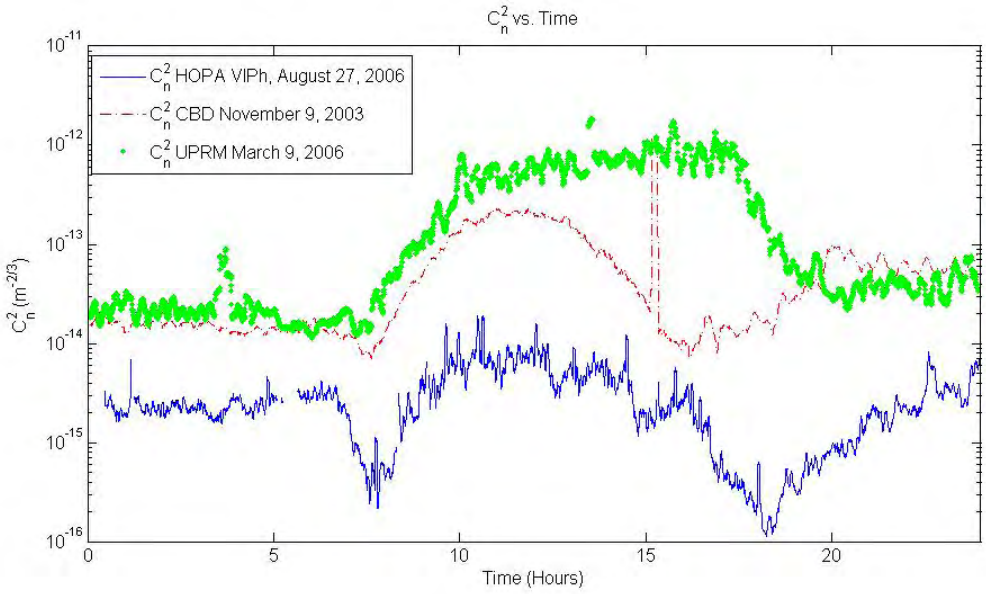

Figure 5.17: Plot of C_n^2 data of the three different experiments. The bottom plot represents the data collected on August 27, 2006 at La Parguera, Puerto Rico. The Middle one show data collected at the Cheseapeake Bay Detachment, Maryland, US, on November 9 2003. The top one show Cn2 data collected over the Physics Building roof at Mayagüez Puerto Rico on March 9 2006.

Chapter 6: Conclusions

In this project the optically measured atmospheric turbulence structure parameter, C_n^2, has been studied under different environment conditions. Also new and innovative techniques for analysis of the time series are been tested and developed.

For our first approach to study the possible influences of the humidity upon the C_n^2 parameter, we analyzed datasets provided by E. Oh of the Naval Research Laboratory. We verified the inverse relationship of C_n^2 with relative humidity as reported by O*h et al.*[14]. This data was the motivation to look for new analysis techniques which allow us to correctly analyze time series which do not possess stationary properties.

The introduction of the Empirical Mode Decomposition method (EMD) to this data was one of the most important steps for the success of this work. The identification of all the Intrinsic Mode Functions (IMFs) of the data and the ability to subtract the trend, allowed us to convert our non-stationary time series signal into a time series signal with stationarity properties. We could then apply standard statistical analysis methods with confidence and more importantly we were able to study in more detail the faster oscillations in our data. The development of the Hilbert Phase Analysis (HPA) in this work provides now what promises to be a powerful tool for the study of multiparameter time series data.

The HPA technique was consistent in the results of the analysis of our data for the three different experiments. The three experiments were distinct in geographical position, geometry and weather conditions, yet the method revealed the inverse relationship claimed in previous work between the C_n^2 and the relative humidity. Also it was very consistent in

identifying different relationships already known in the other weather parameters, specifically the relation between the solar radiation with the temperature and the inverse relation between the temperature and the relative humidity. Maybe the greatest contribution of the method due to this work is to show that the relative humidity is possibly a more consistent indicator for fluctuations in the C_n^2 parameter than the direct bulk parameters of temperature and pressure implemented by Monin-Obukhov similarity based theory which is used in predictive models of C_n^2 such as PAMELA [14]. This can be corroborated by comparing the results of table 5.1 for the CBD experiment where the eight cases studies show an inverse cross covariance between the C_n^2 and the relative humidity, versus just four cases which the show the proportional relationship between C_n^2 and temperature. During the UPRM and HOPA VIPh experiments the cross covariance between the HPA of the different variables show in all the cases a relationship between the C_n^2 and relative humidity. In three of the cases study for the HOPA VIPh experiment the relationship showed for the C_n^2 with the relative humidity it was positive, but there was an inverse relation between C_n^2 and temperature indicating the inverse relation between relative humidity and temperature. The presence of this relationship between the relative humidity and temperature is a strong indicator o the confidence of our method because show relations described by the theory and by other methods.

In conclusion the HPA method shows itself to be a very interesting new technique for the analysis of the time series signals, keeping their physical properties present during the analysis. This method shows it capabilities at a qualitative level and still undergoing improvement to allow for a quantitative level of analysis, which would allow us to determine the amount of influence of the different weather parameters upon the C_n^2 parameter.

Also as a result of this work a database for all the C_n^2 and weather data collected along the three different campaigns has been created for public access and can be accesses through the website http://physics.uprm.edu/~cfont/.

References

[1] L. C. Andrews, R. L. Phillips, C. Y. Hopen. “Laser Beam Scintillation with Applications” SPIE Press, 2001.

[2] M C Roggemann and B Welsh. “Imaging Through Turbulence”. CRC Press LLC, 1996.

[3] R K Tyson. Introduction to Adaptive Optics. SPIE Press, 2000.

[4] L. C. Andrews, R. L. Phillips. “Laser Beam Propagation through Random Media”. SPIE Press, 2005.

[5] R. K. Tyson. “Principles of Adaptive Optics”. Academic Press 1998.

[6] S. G. Lambert, W. L. Casey. “Laser Communications in Space”. Artech House, 1995.

[7] M. Chang, C. O. Font, F. Santiago, Y. Luna, E. Roura and S. Restaino, ‘Marine environment optical propagation measurements’, Proceedings of the SPIE, Volume 5550, pp. 40-46 (2004) .

[8] F. Santiago, C. Wilcox, M. Chang, C. Font, E. Roura, S. Restaino, ‘Low altitude horizontal scintillation measurements of atmospheric turbulence over the sea: Experimental results’, Proceedings of the SPIE, Volume 6014, pp. 321-329 (2005)

[9] C. Font, E. Oh, M. Chang, and C. Gilbreath, ‘Humidity contribution to the strength of turbulence parameter C_n^2’, proc. SPIE 6215, Defense and Security Symposium (April 2006), paper number 6215-3.

[10] C. Font, E. Roura, M. Chang, E. Oh, F. Santiago, C. Wilcox, S. Restaino, C. Gilbreath, ‘On the relationship between C_n^2 and humidity’, proc. SPIE 6268, Astronomical Telescopes & Instrumentation Conferences (May 2006), paper number 6268-127

[11] M. Chang, E. Roura , C. Font, C. Gilbreath, E. Oh, ‘Applying the Hilbert–Huang Decomposition to Horizontal Light Propagation C_n^2 data’ proc.SPIE 6268, Astronomical Telescopes & Instrumentation Conferences (May 2006), paper number 6268-128

[12] M. Chang, C. Font, E. Oh, C. Gilbreath, ‘Humidity’s influence on visible region refractive index structure parameter C_n^2’, Summited for publication in Applied Optics Journal, Manuscript ID: 71778

[13] C. Font, M. Chang, E. Oh, C. Gilbreath, ‘Applying the Hilbert Phase Analysis to the study of Atmospheric Turbulence Data’, Optical Society of America Meeting, October 8-12 2006. Press #: JWD45

[14] E. Oh, J. Ricklin, F. Eaton, C. Gilbreath, S. Doss-Hammell, C. Moore, J. Murphy, Y. H. Oh, and M. Stell, W. Gao and D. R. Shaw, 'Estimating optical turbulence using the PAMELA model,' in Remote Sensing and Modeling of Ecosystems for Sustainability, eds., Proc. SPIE 5550, pp. 256–266, 2004.

[15] G. Rilling, P. Flandrin and P. Gonclaves'On empirical mode decomposition and its algorithms'

[16] N. E. Huang, Z. Shen, S. R. Long, M. C. Wu, H. H. Shih, Q. Zheng, N.-C. Yen, C. C. Tung, and H. H. Liu, 'The empirical mode decomposition and the Hilbert spectrum for nonlinear and non-stationary time series analysis,' Proc. R. Soc. Lond. Ser. A 454, pp. 903–995, 1998.

[17] S. F. Clifford, G. R. Ochs, and R. S. Lawrence, "Saturation of optical scintillation by strong turbulence," Journal of the Optical Society of America 64, 148–154 (1974).

[18] M. Born and E. Wolf, "Principles of Optics, 7th edition", Cambridge University Press, Cambridge 1999.

Appendix A

Published Conferences Proceedings & Presentations

- '**Humidity contribution to the strength of turbulence parameter C_n^2**', Carlos Font, Eun Oh, Mark Chang, and Charmaine Gilbreath, **proc. SPIE 6215**, Defense and Security Symposium (April 2006), **paper number 6215-3**.

- '**On the relationship between C_n^2 and humidity**', Carlos Font, Erick Roura, Mark Chang, Eun Oh, Freddie Santiago, Christopher Wilcox, Sergio Restaino, Charmaine Gilbreath, **proc. SPIE 6268**, Astronomical Telescopes & Instrumentation Conferences (May 2006), **paper number 6268-127**

- '**Applying the Hilbert–Huang Decomposition to Horizontal Light Propagation C_n^2 data**' Mark Chang, Erick Roura , Carlos Font, Charmaine Gilbreath, Eun Oh, **proc. SPIE 6268**, Astronomical Telescopes & Instrumentation Conferences (May 2006), **paper number 6268-128**

- '**Applying the Hilbert Phase Analysis to the study of Atmospheric Turbulence Data**' Carlos Font, Mark Chang, Eun Oh, Charmaine Gilbreath. Optical Society of America Meeting, October 8-12 2006. **Pressentation #: JWD45**

Humidity contribution to the refractive index structure function C_n^2.

Carlos O. Font, Mark P. J. L. Chang[1], Eun Oh and Charmaine Gilbreath[2]

[1]Physics Department, University of Puerto Rico, Mayagüez, Puerto Rico 00680
[2]U.S. Naval Research Laboratory, Washington D.C. 20375

ABSTRACT

Humidity and C_n^2 data collected from the Chesapeake Bay area during the 2003/2004 period have been analyzed. We demonstrate that there is an unequivocal correlation between the data during the same time periods, in the absence of solar insolation. This correlation manifests itself as an inverse relationship. We suggest that C_n^2 in the infrared region is also function of humidity, in addition to temperature and pressure.

Keywords: Strength of turbulence, humidity, scintillation

1. INTRODUCTION

It has been known for some time[1] that the scintillation behaviour of point sources is a measure of the optical seeing in the atmosphere. What has been less well understood is the contribution of different environmental variables to optical seeing. Over the past decade, a great deal of study has been dedicated to clarifying this issue.

Comprehensive treatments of the theory of wave propagation in random media are given in Tatarskii's seminal works.[2,3] More recent developments are described in Tatarskii et al..[4] Some of the simplest models based on these complex works are well known and available in the literature: Greenwood,[5] Hufnagel–Valley,[6] SLC-Day and SLC-Night.[7] These models are used to predict the strength of weak clear air turbulence's refractive index structure function, C_n^2, but in all cases they have major failings: either they are too general and do not take into account local geography and environment (as in the former two) or they are too specific to a site (as in the latter two, which reference the median values above Mt. Haleakala in Maui, Hawaii).

A more recent numerical model known as PAMELA does attempt to account for geographical position and ambient climate factors. However, its inverse power windspeed term fails to explain some of the characteristics of C_n^2 during low wind conditions. It does an adequate job for characterizing horizontal and diagonal beam propagation within the atmospheric boundary layer.[8]

Despite the differences, the models agree in terms of the overall general behaviour of C_n^2. For example, it is to be expected that during the daylight hours, the C_n^2 trend will be dominated by the solar insolation and in those models that do account for day/night differences this is presented. The physical effect is evidenced in Oh,[9] where in many cases scintillometer measurements are seen to strongly follow the measured solar insolation function. When the sun sets however, it is less clear as to the predominant contributing factors. In an extension of earlier work, Oh presented indications of a possible anticorrelation effect between the ambient relative humidity and the value of C_n^2.

In this paper, we report on further analysis of the datasets obtained during that study to show that there is an unequivocal correlation in the absence of solar insolation in a littoral space.

Further author information: (Send correspondence to M.P.J.L.C.)
M.P.J.L.C.: E-mail: mchang@uprm.edu, Telephone: 1 787 265 3844

2. INSTRUMENTS AND ALGORITHMS

The C_n^2 and associated weather variable data was collected over a number of days during 2003 and 2004 at the Chesapeake Bay Detachment (CBD) of the Naval Research Laboratory.

The C_n^2 data was obtained with a commercially available scintillometer (model LOA-004) from Optical Scientific Inc, which serves as both a scintillometer and as an optical anemometer for winds transverse to the beam paths. The local weather parameters were determined by a Davis Provantage Plus (DP+) weather station. The LOA-004 had a sample rate of 10 seconds, while the DP+ was set at 5 minutes.

The LOA-004 instrument comprises of a single modulated infrared transmitter whose output is detected by two single pixel detectors. For these data, the separation between transmitter and receiver was 100-m. The path integrated C_n^2 measurements are determined by the LOA instrument by computation from the log–amplitude scintillation ($C_\chi(r)$) of the two receiving signals.[10,11] The algorithm for relating $C_\chi(r)$ to C_n^2 is based on an equation for the log–amplitude covariance function in Kolmogorov turbulence by Clifford *et al.*,[12] which we repeat here

$$C_\chi(r) = 2.94 \int_0^1 du \sigma_T^2(u)[u(1-u)^{5/6}] \int_0^\infty dy y^{-11/6} sin^y \exp\{-\sigma_T^2[u(1-u)]^{5/6} F(y)\} J_0 \left\{ \left[\frac{4\pi y u}{(1-u)} \right]^{1/2} r \right\} \quad (1)$$

The terms in this equation are: r, the separation between two point detectors in Fresnel zones $\sqrt{\lambda L}$, with L being the path distance between source and detectors; y is the normalized spatial wavenumber; $u = z/L$ is the normalized path position; J_0 is the zero order Bessel function of the first kind and

$$\begin{aligned} \sigma_T^2(u) &= 0.124 k^{7/6} L^{11/6} C_n^2(u) \\ F(y) &= 7.02 y^{5/6} \int_{0.7y}^\infty d\xi \xi^{-8/3} [1 - J_0(\xi)] \end{aligned} \quad (2)$$

This can be better appreciated if we define a path weighting function $W(u)$ such that

$$C_\chi(r) = \int_0^1 du C_n^2(u) W(u) \quad (3)$$

for a point source and point receivers where

$$W(u) = 0.365 k^{7/6} L^{11/6} [u(1-u)]^{5/6} \int_0^\infty dy g(u,y) J_0 \left\{ \left[\frac{4\pi y u}{(1-u)} \right]^{1/2} r \right\} \quad (4)$$

In the above expression, $g(u,y)$ carries the information related to C_n^2 for point source and point receivers. It can be modified to incorporate finite receiver and transmitter geometries.

Some comments are necessary at this point. The key assumptions made by the LOA-004 instrument in computing C_n^2 are:

- The turbulent power spectrum is Kolmogorov; the spatial power spectrum of temperature fluctuations $\Phi_T^2(k)$ and the humidity fluctuations $\Phi_H^2(k)$ are proportional to $k^{-5/3}$. This may not always be true, especially if the inner and outer scales are on the order of the relevant dimensions of the observing system.
- As a result of the previous assumption, the index of refraction structure function is assumed to be dependent only on the temperature structure function and pressure at optical frequencies.

What we demonstrate in this paper is that the LOA-004 measured C_n^2 function from the CBD experiment is indeed correlated with the humidity. The LOA-004's design is by no means optimal for extracting C_n^2, since its main purpose is to act as an anemometer. To that end we have an effort to evaluate contributions to the measurement error of C_n^2.

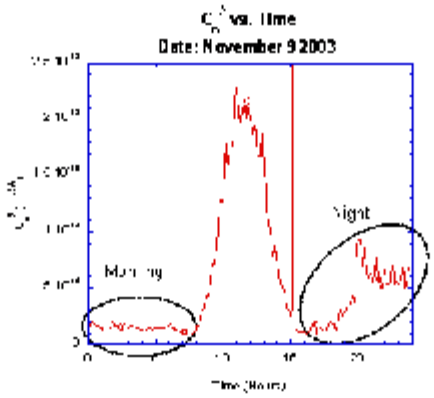

Figure 1. Morning and Night definitions for our purposes. See text for details.

3. ANALYSIS

The C_n^2 data was smoothed with a 60 point rolling average function. The effect of solar insolation was excluded from this study. We defined the morning and night portions of a 24 hour period as shown in Figure (1). Morning runs from midnight until sunrise (as corroborated by a solar irradiance measurement), while night runs from sunset to 23:59. As reported in Oh *et al.*[9] visual inspection of the valid time series data gives the impression that there is an approximate inverse relationship between C_n^2 and humidity. This can be appreciated in a more quantitative manner by graphing C_n^2 against humidity.

We chose data sets in which the temperature variations are no more than $\pm 15\%$ and the pressure change is at most 15 mbars over the time intervals of interest. The data sections were also selected to have no scattering effects due to snow or rain, and the wind was northerly (to within approximately $\pm 20°$, inflowing from the bay to land).

Given the aforementioned conditions, from the data available only a subset provided complete time series in both ambient weather variables and C_n^2. We were able to extract eight morning and evening runs, spanning seven days between November 2003 and March 2004 for the purpose of calculating the crosscorrelation, $\Gamma_{UV}(t+\delta t) = E[u(t+\delta t)v(t)]$, and cross covariance, $C_{UV}(t+\delta t) = E(u(t+\delta t) - \overline{u})(v(t) - \overline{v})$, between humidity and C_n^2 measureables. In these parameters, E represents expected value and $\overline{u}, \overline{v}$ are the mean values of the two random processes, considered stationary.

As can be seen from Figures (2 - 9), the C_n^2 against humidity correlograms all evidence a negative gradient. The tightness of the correlation is better examined in terms of the cross covariance. The results are normalized such that the value at zero time lag was unity for identically varying data.

3.1. Comments on Figures (2 - 9)

Fig.(2) The correlogram shows an approximately even dispersion along the length of the best fit trendline. The cross covariance lacks symmetry.

Fig.(3) The correlogram shows the tightest correlation between the data series of all the plots and the cross covariance is quite symmetric, although highly structured.

Fig.(4) The correlogram is fairly even, with some larger dispersion possibly occuring around 70% of humidity. The cross covariance is symmetric.

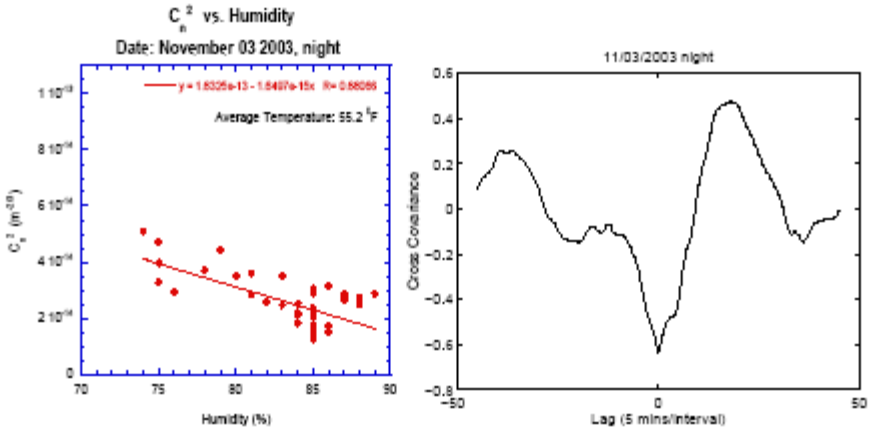

Figure 2. Nov 3 2003, Night

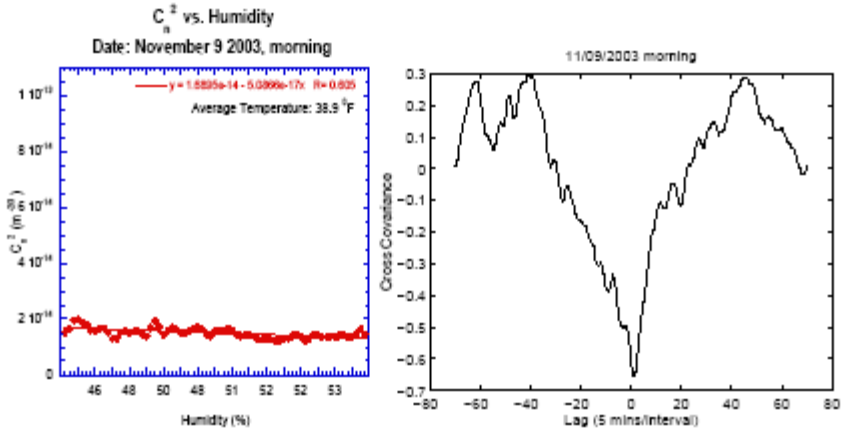

Figure 3. Nov 9 2003, Morning

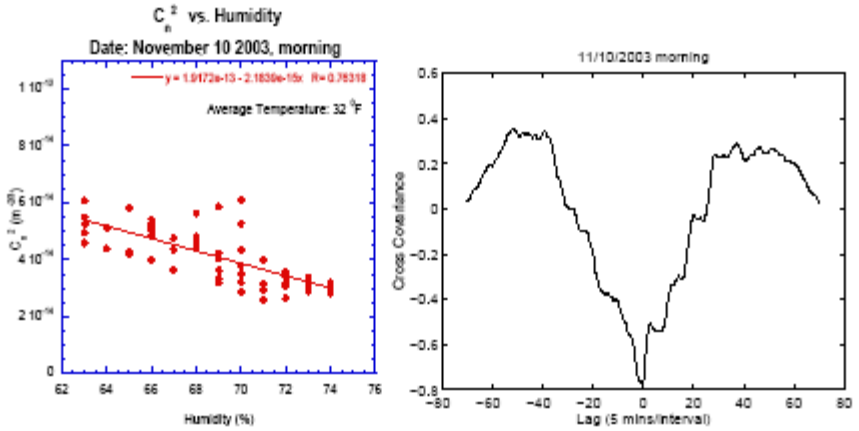

Figure 4. Nov 10 2003, Morning

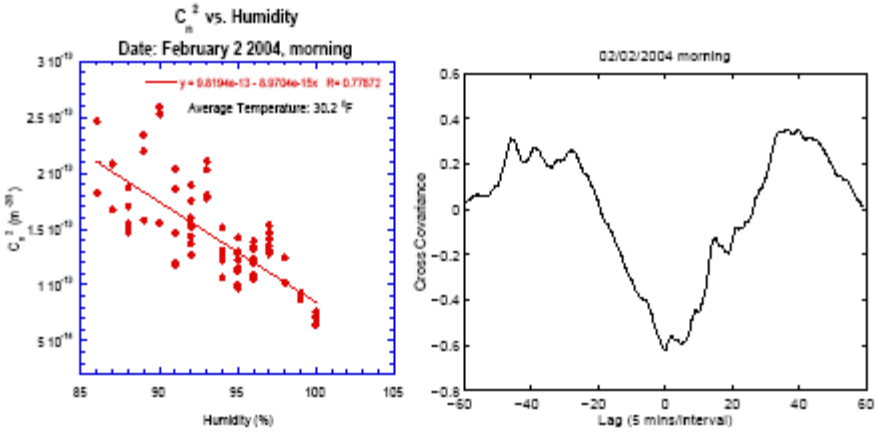

Figure 5. Feb 2 2004, Morning

5

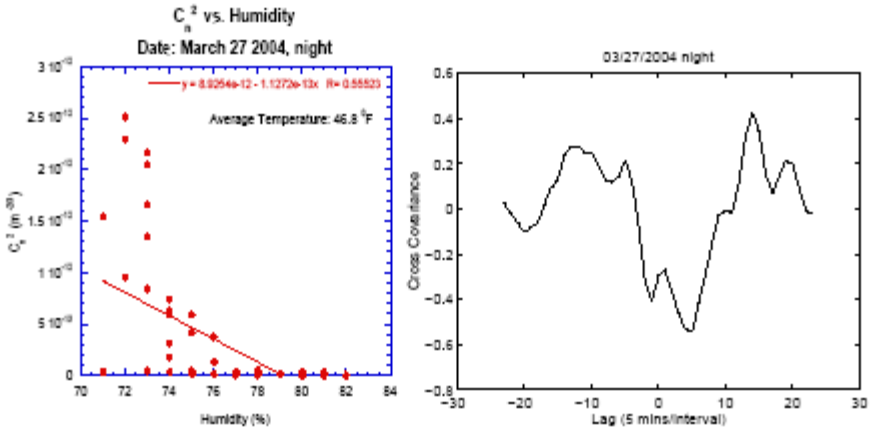

Figure 6. Mar 27 2004, Night

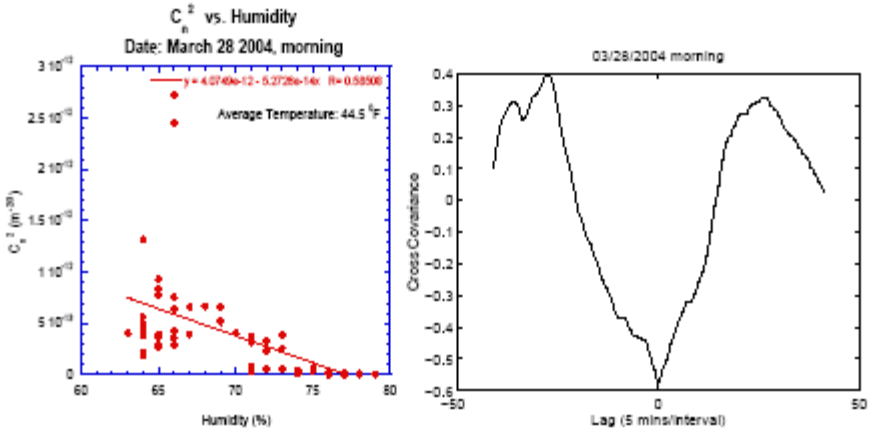

Figure 7. Mar 28 2004, Morning

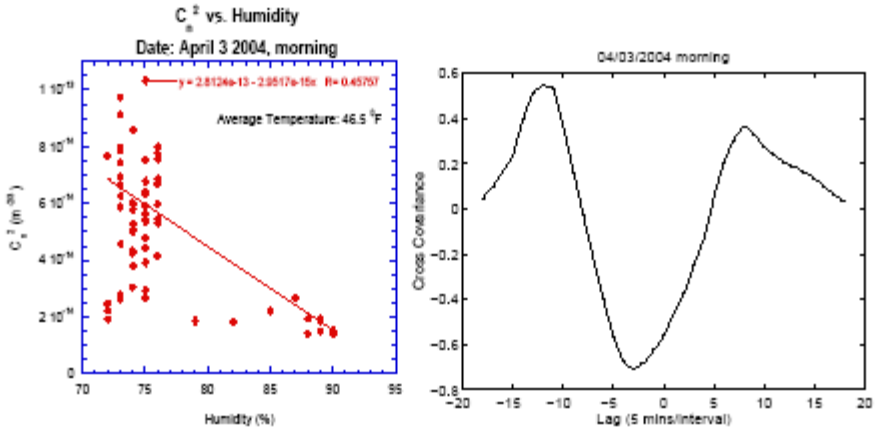

Figure 8. Apr 3 2004 Morning

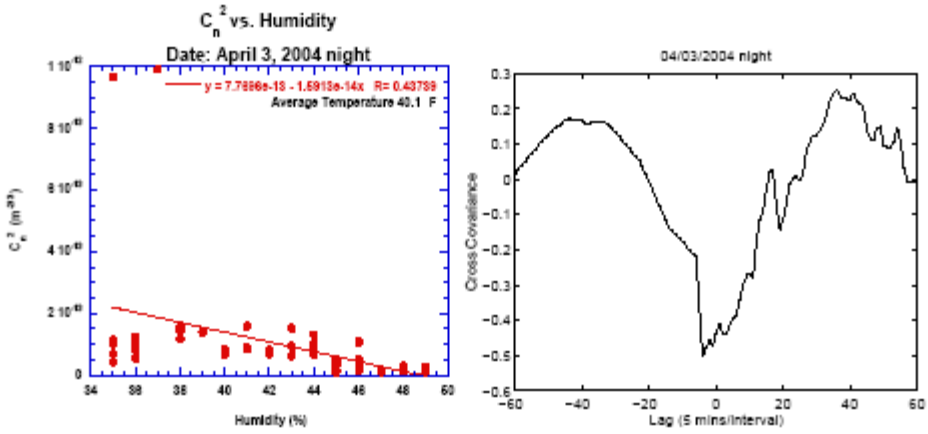

Figure 9. Apr 3 2004, Night

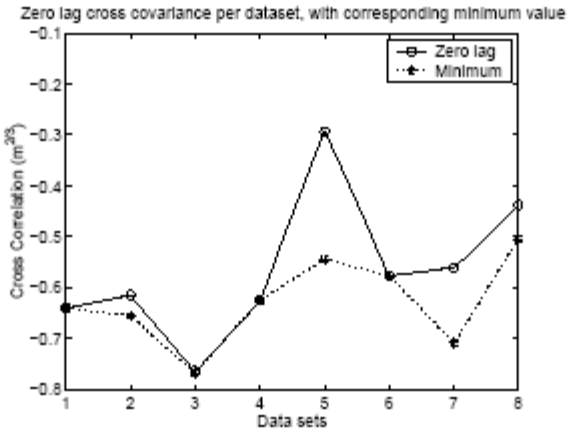

Figure 10. Cross covariance at zero lag. The data set numbers are defined in Table (1).

Fig.(5) The correlogram is evenly dispersed and the cross covariance is symmetric although spread.

Fig.(6) A greater dispersion is seen between 72% and 74% humidity than along the rest of the trendline, although in terms of magnitude it is not very large. The cross correlation is highly asymmetric with the minimum offset from the zero lag position.

Fig.(7) A greater dispersion is seen below 67% humidity than along the rest of the trendline (again the magnitude is not larger than the other plots).

Fig.(8) A large cluster of weakly correlated points are seen below 77% humidity. The cross covariance minimum is offset from the zero lag position but is otherwise reasonably symmetric.

Fig.(9) The correlogram shows a reasonably good correlation between the data series, although the cross covariance shows less symmetry than might be expected from the correlogram.

3.2. Covariance at zero lag, $C_{UV}(\delta t = 0)$

The C_{UV} at zero lag (i.e. when both C_n^2 and humidity data sets are totally overlapping) are given in Figure (10) and Table (1). The evidence for a negative correlation of humidity with C_n^2 is extremely strong; where the minimum cross covariances are different to the zero lag value, there is a time lag offset of no more than 25 minutes (equal to 5 sample points). Some of the offset error is possibly due to a timing mismatch between the clocks used for the DP+ and the LOA-004 instruments; even without accounting for this, the $C_{UV}(\delta t = 0)$ is still strongly negative.

The cross covariance method has provided unequivocal measures that the humidity and C_n^2 functions are negatively correlated.

4. CONCLUSIONS

Using empirical data, we have conclusively demonstrated that a strong negative correlation exists between the humidity and C_n^2 readings from experimental runs at the Naval Research Laboratory's Chesapeake Bay Detachment, for path lengths of about 100-m with relatively constant pressure, temperature and windspeed.

Data set number	Date [mm/dd/yyyy]	Zero timelag cross covariance
1	11/03/2003 night	-0.6397
2	11/09/2003 morning	-0.6144
3	11/10/2003 morning	-0.7632
4	02/02/2004 morning	-0.6251
5	03/27/2004 morning	-0.2930
6	03/28/2004 morning	-0.5764
7	04/03/2004 morning	-0.5604
8	04/03/2004 night	-0.4374

Table 1. The cross correlation datasets.

On the basis of this we suggest that C_n^2 is an inverse function of humidity in the absence of solar insolation at coastal sites.

We are currently in the process of taking equivalent data at UPR-Mayagüez and we expect to obtain measurements in the much less humid environment of New Mexico. With the availability of more data, we will be able to ascertain in a quantitative fashion the humidity contribution to C_n^2. We anticipate that a much deeper understanding of C_n^2 will be found from analysis of the complete data obtained under these extrememly varied ambient conditions.

ACKNOWLEDGMENTS

MPJLC would like to thank Haedeh Nazari and Erick Roura for valuable discussions.

REFERENCES

1. F. Roddier, "The effects of atmospheric turbulence in optical astronomy," *Progress in Optics* XIX, pp. 281–377, 1981.
2. V. Tatarskii, *Wave Propagation in a Turbulent Medium*, Mc Graw-Hill, New York, 1961.
3. V. Tatarskii, *The Effects of a Turbulent Atmosphere on Wave Propagation*, Israel Program for Scientific Translations, Jerusalem, 1971.
4. V. I. Tatarskii, M. M. Dubovikov, A. A. Praskovskii, and M. I. Kariakin, "Temperature fluctuation spectrum in the dissipation range for statistically isotropic turbulent flow," *Journal of Fluid Mechanics* 238, pp. 683–698, 1992.
5. D. P. Greenwood, "Bandwidth specifications for adaptive optics systems," *Journal of the Optical Society of America* 67, pp. 390–392, 1977.
6. R. R. Beland, *Propagation through atmospheric optical turbulence*, SPIE Optical Engineering Press, Bellingham, Washington, 1993.
7. M. Miller and P. L. Zieske, "Turbulence environmental characterization." RADC-TR-79-131, ADA072379, Rome Air Development Center, 1976.
8. Y. Han-Oh, J. C. Ricklin, E. S. Oh, and F. D. Eaton, "Evaluating optical turbulence effects on free-space laser communication: modeling and measurements at ARL's A_LOT facility," in *Remote Sensing and Modeling of Ecosystems for Sustainability*, W. Gao and D. R. Shaw, eds., *Proc. SPIE* 5550, pp. 247–255, 2004.
9. E. Oh, J. Ricklin, F. Eaton, C. Gilbreath, S. Doss-Hammell, C. Moore, J. Murphy, Y. H. Oh, and M. Stell, "Estimating optical turbulence using the PAMELA model," in *Remote Sensing and Modeling of Ecosystems for Sustainability*, W. Gao and D. R. Shaw, eds., *Proc. SPIE* 5550, pp. 256–266, 2004.
10. G. R. Ochs and T.-I. Wang, "Finite aperture optical scintillometer for profiling wind and C_n^2," *Applied Optics* 17, pp. 3774–3778, 1979.
11. T.-I. Wang, "Optical flow sensor." USA Patent No. 6,369,881 B1, April 2002.
12. S. F. Clifford, G. R. Ochs, and R. S. Lawrence, "Saturation of optical scintillation by strong turbulence," *Journal of the Optical Society of America* 64, pp. 148–154, 1974.

On the relationship between C_n^2 and humidity

Carlos O. Font, Mark P. J. L. Chang, Erick A. Roura[1], Eun Oh and Charmaine Gilbreath[2]

[1]Physics Department, University of Puerto Rico, PO Box 9016, Mayagüez, Puerto Rico 00681-9016
[2]U.S. Naval Research Laboratory, Washington D.C. 20375

ABSTRACT

We have recently shown the refractive index structure constant C_n^2 in the visible and near infrared to be a strong function of humidity in the absence of solar insolation effects, in stark contrast to the commonly held assumption that the humidity contribution can be ignored in that waveband. We expand our analysis of the effects of humidity on C_n^2 as measured across a 100-m long horizontal beam path to include temperature. Also we present a new technique for extracting information on changes in the parameter space of C_n^2 and local weather variables, which we term Hilbert Phase Analysis (HPA). This methodology, based on extracting the phase of the analytic signal via Hilbert transforms, reveals a wealth of detail that conventional analysis techniques cannot determine. The HPA provides additional confirmation that C_n^2 is strongly influenced by local humidity in the visible region. We have also found that HPA provides a clear demonstration that humidity competes with temperature in affecting the value of C_n^2.

Keywords: Hilbert Phase Analysis, Humidity, Refractive Index Structure Function

1. INTRODUCTION

During 2003 and 2004, measurements were taken of path integrated C_n^2 and a host of local climate parameters using commercially available instruments, as discussed in Font[1] *et al.* We present follow–up analysis of the datasets presented in the aforementioned work in this paper, wherein we identify system changes through Hilbert Transform based phase analysis or HPA.

1.1. HILBERT ANALYSIS OF TIME SERIES

Gabor defined the complex analytic signal, namely

$$\begin{aligned} \Psi(t) &= X(t) + iY(t) \\ \text{where } Y(t) &= \mathcal{H}[X(t)] \\ &= \frac{-1}{\pi} \mathrm{P} \int_\Omega \frac{X(t)}{(s-t)} ds \ , \quad t \in \Omega \end{aligned} \tag{1}$$

where $\mathcal{H}[\bullet]$ represents a Hilbert Transform. As a result, $\Psi(t)$ is unique and an analytic signal. The Hilbert Transform is a well known integral transform with a singular kernel $(1/(\pi(t-s))$, s also being a time variable if t is time. As a result it is also a Cauchy Principal integral, which we denote by P, where the real axis singularity at $t = s$ is taken along a positive semi-circular path. An alternative way of writing Equation 1 is

$$\begin{aligned} \Psi(t) &= a(t) \exp^{i\Phi(t)} \ , \quad \text{whence} \\ a(t) &= \sqrt{X^2(t) + Y^2(t)} \\ \Phi(t) &= \arctan\left(\frac{Y(t)}{X(t)}\right) \end{aligned} \tag{2}$$

This de Moivre form of the analytic signal is similar to the Fourier amplitude and phase expression. Note though that the Hilbert amplitude and phase are time dependent variables, as opposed to the Fourier analysis where they are fixed values per frequency.

Further author information: (Send correspondence to M.P.J.L.C.)
M.P.J.L.C.: E-mail: mchang@uprm.edu, Telephone: 1 787 265 3844

1.2. A PHYSICAL HILBERT TRANSFORMATION

If one applies the Hilbert Transform directly to a time varying signal, there is a high probability that at least one of five paradoxes[2] will be encountered, leading to unphysical results, due to the presence of so–called "riding waves" which cause asymmetries in the signal.

These paradoxes may be avoided by the application of Empirical Mode Decomposition[3] (EMD) method developed in a seminal work by Huang *et al.*[4] From the application of the EMD method, we extract Intrinsic Mode Functions (IMFs) whose instantaneous frequencies are well defined.

The application of the Hilbert Transform to the IMFs yields physically meaningful interpretations of the oscillatory phenomena. This may be best appreciated if we consider the Hilbert phase space, as in Figure 1.

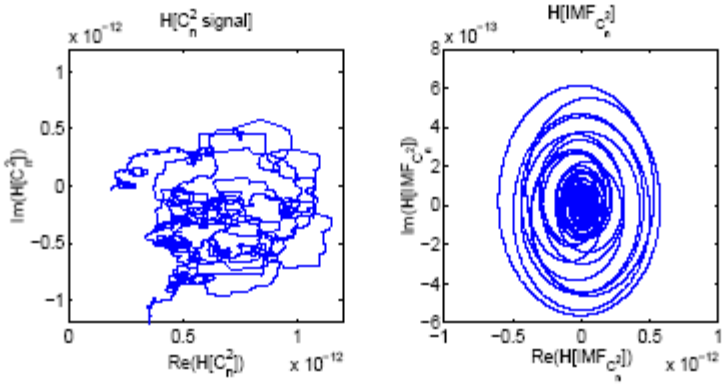

Figure 1. (a) Hilbert Phase Space plot of recorded C_n^2 signal, (b) Hilbert Phase Space plot of an example IMF of the C_n^2 signal.

By naïvely applying the Hilbert Transform to a non–stationary time series (C_n^2 measurements) we see that the trajectory of the analytic signal's vector is subject to many alterations in origin and phase angle. The instantaneous frequency, defined as

$$\omega = \frac{d\Phi}{dt} \tag{3}$$

can have both positive and negative values, rendering the Hilbert transform physically uninterpretable. The Hilbert Transform of the IMFs, of which an example is shown on the right side of Figure 1, ensures that the analytic signal vector's origin stays fixed and no sudden changes in the direction of ω occur.

1.3. HILBERT PHASE ANALYSIS

The HPA technique is based on the conditions mentioned in the previous subsections. The IMFs determined through EMD from the input signal are the analytic signal eigenfunctions of the EMD sifting operation and it is clear that a phase angle ($\Phi(t)$), as well as an amplitude ($a(t)$), can be determined from them. Physical effects of a non–linear, non–stationary time varying system can be studied by summing the $\Phi(t)$s of all the IMFs. It should be noted that the operations

$$\mathrm{H}\left[\sum \mathrm{IMF}\right] \quad \text{and} \quad \sum \mathrm{H}\left[\mathrm{IMF}\right] \tag{4}$$

are commutable, as may be seen in Figure 2. The term $\mathrm{H}[\bullet]$ represents the Hilbert Transform.

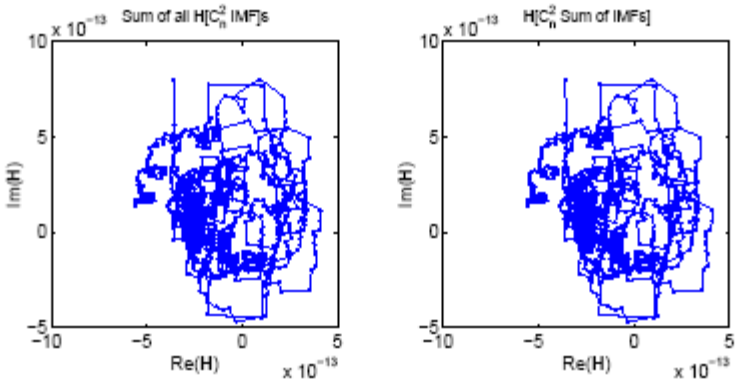

Figure 2. Plots illustrating the commutability of operations.

2. DATA

2.1. HPA PROTOCOL

The procedure for the HPA data analysis is as follows:

1. Firstly, we decompose the C_n^2, humidity and temperature time series measured at the Cheasapeake Bay Detachment (CBD) facility of the Naval Research Laboratory via EMD, obtaining their IMFs and trend lines.
2. Next we apply the Hilbert Transform to the various IMF sets, taking care to exclude the trend lines.
3. As a final step, we sum the phase angle $\Phi(t)$ of the Hilbert Transformed IMFs.

2.2. RESULTS

The Hilbert phase angles $\Phi(t)$ are plotted for each of the time series: C_n^2, humidity and temperature in Figures 3 to 10. We also include the difference between pairs of phase angle series: $\Phi_C - \Phi_H$, $\Phi_C - \Phi_T$ and $\Phi_C - \Phi_{(H+T)/2}$.

3. DISCUSSION

Upon inspecting the Hilbert phase of the C_n^2 IMFs, Φ_C, we see that the gradients of the various functions are not constant, although there is an increasing trend in all the plots. The Hilbert phase functions of humidity and temperature, Φ_H, Φ_T respectively, also show an increase (except for one case, where the temperature function produced only the trend) with time, although their gradients vary markedly between data sets.

The straightforward average function of the humidity and temperature phase angles are all approximately linear (and increasing) over time in all cases. This occurs despite the variations in the individual Φ_H and Φ_T; the conclusion that we may draw from this observation is that the humidity and temperature are approximately inversely related during the time intervals of these data sets.

To better understand the dependence of Φ_C upon humidity and temperature, we turn to the plots of the difference functions against time. The overall linearity of the Φ_C and $(\Phi_H + \Phi_T)/2$ functions might lead one to expect that $[\Phi_C - (\Phi_H + \Phi_T)/2]$ would be constant as a function of time. The actual graphs give the lie to that expectation. Instead what is seen is the influence of different factors competing over time, a fact that is deduceable by comparison with the $\Phi_C - \Phi_H$ and $\Phi_C - \Phi_T$ graphs.

As a result of inspecting the various difference functions, we conclude the following,

- November 3, 2003 (night) : temperature dominates the C_n^2 behaviour.
- November 9, 2003 (morning) : both temperature and humidity vie for dominance over the time interval of this sample.
- November 10, 2003 (morning) : temperature dominates.
- February 2, 2004 (morning) : the earlier half is dominated by temperature and the latter half is dominated by humidity.
- March 27, 2004 (night) : temperature dominates.
- March 28, 2004 (morning) : humidity dominates.
- April 3, 2004 (morning) : temperature dominates.
- April 3, 2004 (night) : humidity dominates.

4. CONCLUSIONS

We have described the Hilbert Phase Analysis, a new technique for determining the characteristics of multiple, non–stationary time series data and their interrelated effects. We have found that the contribution of humidity to C_n^2 is significant and cannot be disregarded, confirming our earlier work. We have also determined that temperature had an approximate inverse relationship to humidity in the measurements taken. Finally, and most significantly, we have shown that the HPA methodology is able to discriminate between the competing influences of humidity and temperature on the behaviour of C_n^2.

ACKNOWLEDGMENTS

Thanks are due to Sergio Restaino, Christopher Wilcox and Freddie Santiago for help with the scintillometers and data reduction software.

REFERENCES

1. C. O. Font, M. P. J. L. Chang, E. Oh, and C. Gilbreath, "Humidity contribution to the refractive index structure function C_n^2," in *Atmospheric Propagation III, Proc. SPIE* 6215, p. *in press*, 2006.
2. L. Cohen, *Time frequency analysis*, Prentice Hall, Englewood Cliffs, New Jersey, 1995.
3. E. Oh, J. Ricklin, F. Eaton, C. Gilbreath, S. Doss-Hammell, C. Moore, J. Murphy, Y. H. Oh, and M. Stell, "Applying the hilbert-huang decomposition to horizontal light propagation C_n^2 data," in *Advances in Stellar Interferometry, Proc. SPIE* 6268, p. *these proceedings*, 2006.
4. N. E. Huang, Z. Shen, S. R. Long, M. C. Wu, H. H. Shih, Q. Zheng, N.-C. Yen, C. C. Tung, and H. H. Liu, "The empirical mode decomposition and the Hilbert spectrum for nonlinear and non-stationary time series analysis," *Proc. R. Soc. Lond. Ser. A* 454, pp. 903–995, 1998.

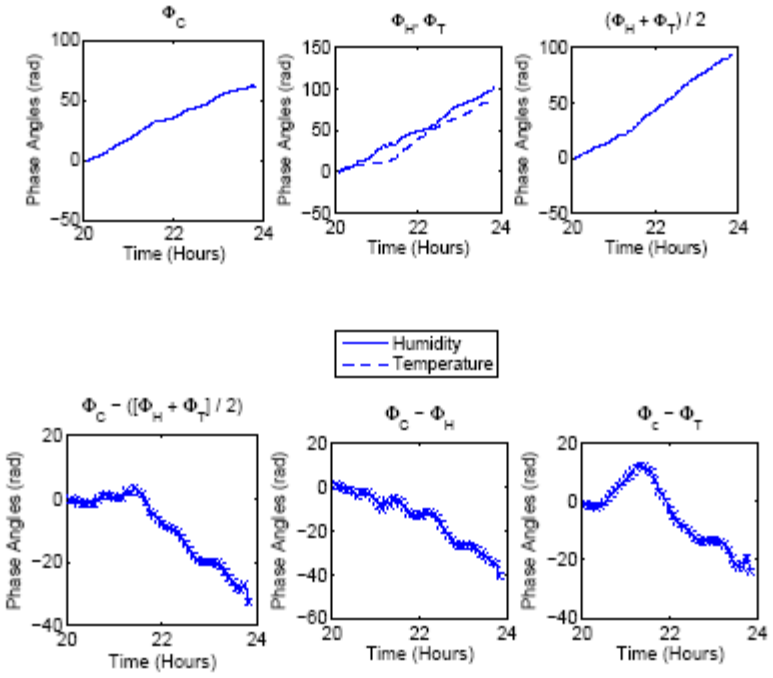

Figure 3. November 3, 2003 night. Temperature dominates.

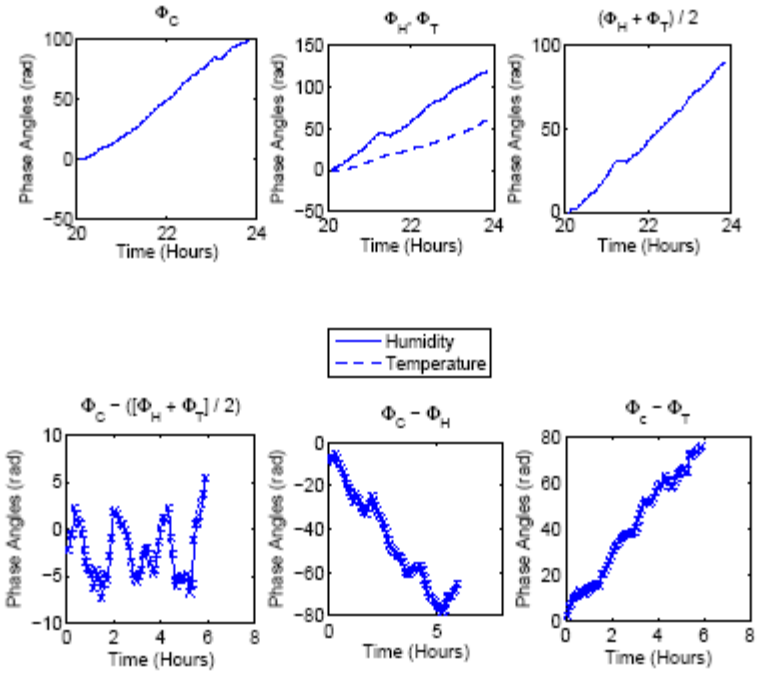

Figure 4. November 9, 2003 morning. Temperature and humidity are seen to compete for influence on the C_n^2 function.

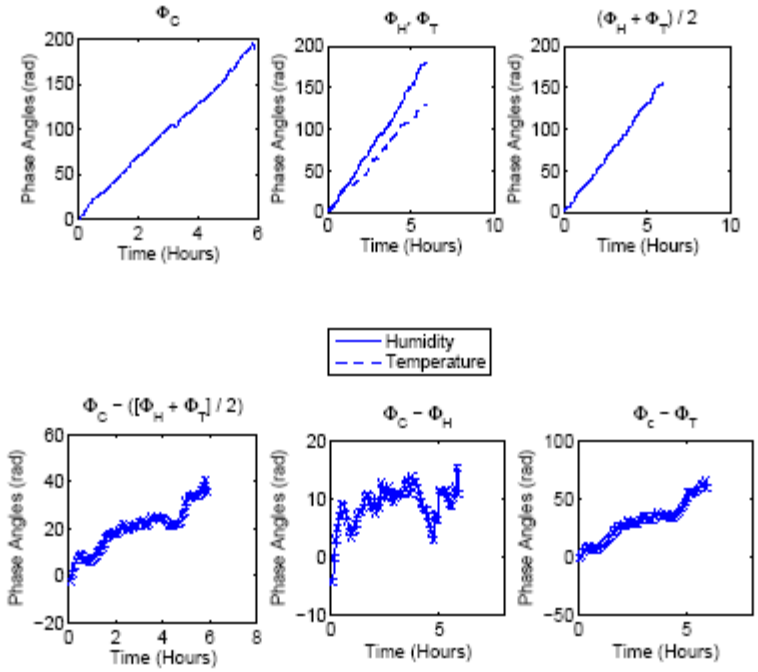

Figure 5. November 10, 2003 morning. Temperature dominates.

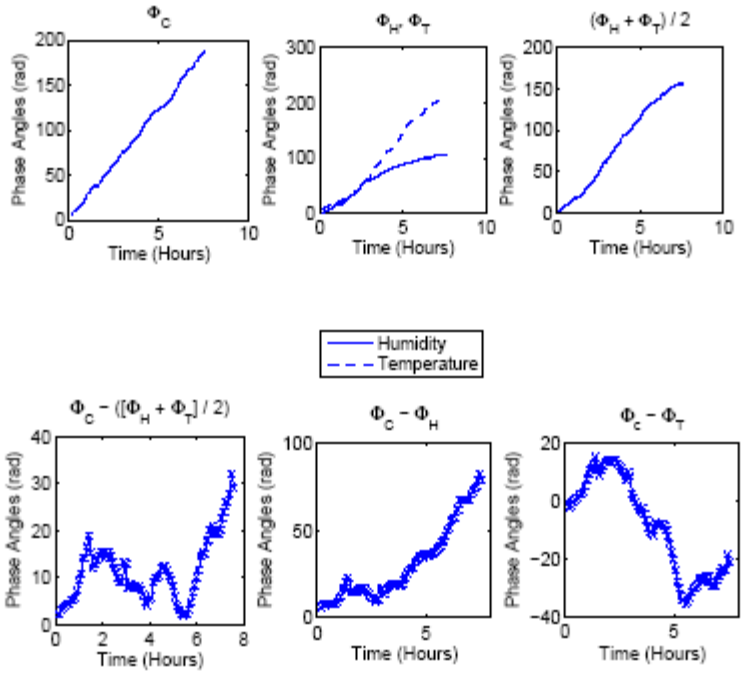

Figure 6. February 2, 2004 morning. Temperature dominates in the early stage, then humidity takes over.

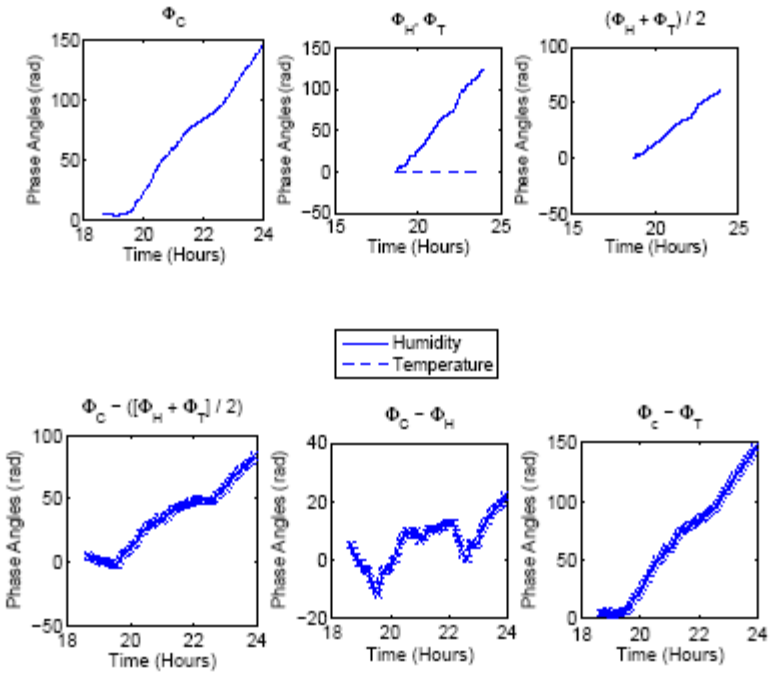

Figure 7. March 27, 2004 night. The temperature phase plot shows a constant phase angle since the original data was in itself an IMF, therefore EMD extracted only a single IMF. Naturally temperature dominates.

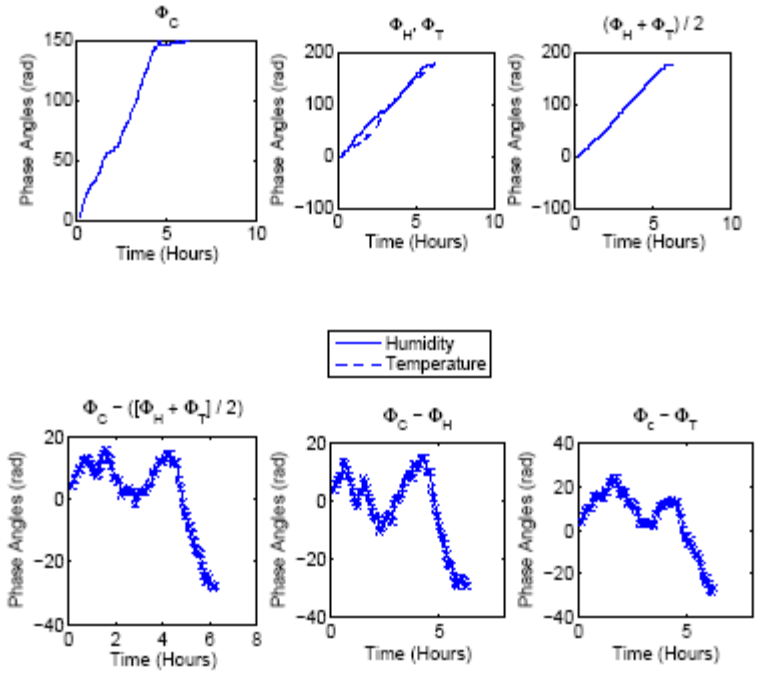

Figure 8. March 28, 2004 morning. Humidity dominates.

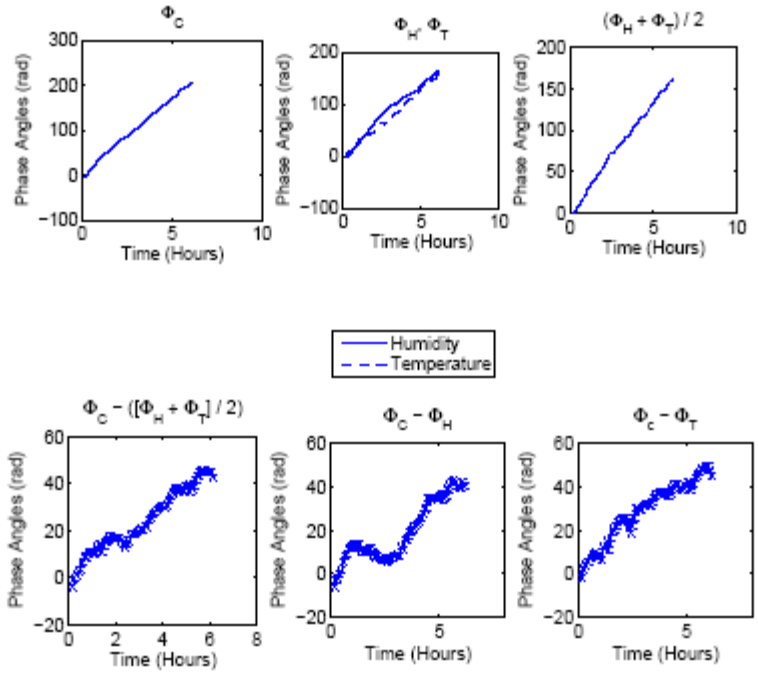

Figure 9. April 3, 2004 morning. Temperature dominates.

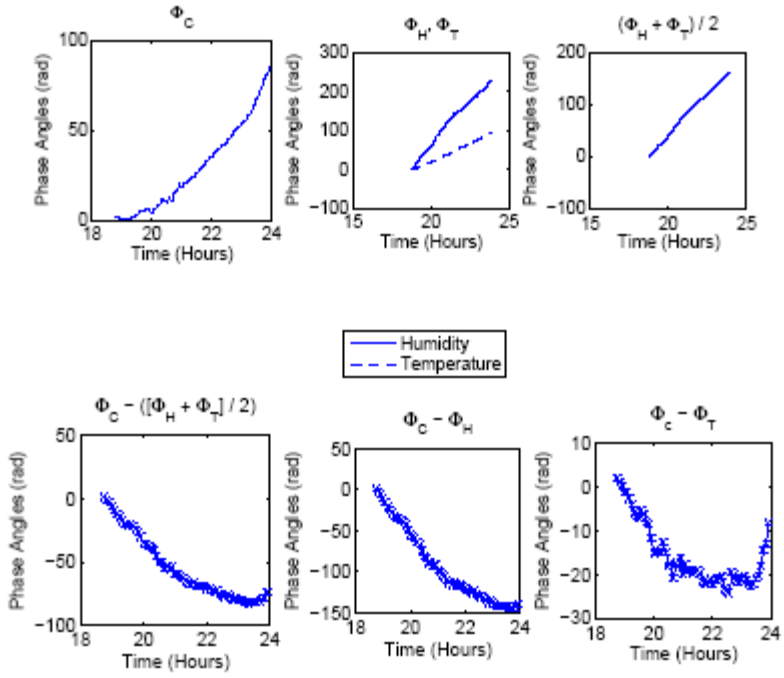

Figure 10. April 3, 2004 night. Humidity dominates.

Applying the Hilbert–Huang Decomposition to Horizontal Light Propagation c_n^2 data

Mark P. J. L. Chang, Erick A. Roura, Carlos O. Font[1], Charmaine Gilbreath and Eun Oh[2]

[1]Physics Department, University of Puerto Rico, Mayagüez, Puerto Rico 00680
[2]U.S. Naval Research Laboratory, Washington D.C. 20375

ABSTRACT

The Hilbert Huang Transform is a new technique for the analysis of non–stationary signals. It comprises two distinct parts: *Empirical Mode Decomposition* (EMD) and the *Hilbert Transform* of each of the modes found from the first step to produce a Hilbert Spectrum. The EMD is an adaptive decomposition of the data, which results in the extraction of Intrinsic Mode Functions (IMFs). We discuss the application of the EMD to the calibration of two optical scintillometers that have been used to measure C_n^2 over horizontal paths on a building rooftop, and discuss the advantage of using the Marginal Hilbert Spectrum over the traditional Fourier Power Spectrum.

Keywords: Empirical Mode Decomposition, Hilbert Transform, Strength of Turbulence, Scintillation

1. INTRODUCTION

The common practice when studying time series data is to invoke the tools of Fourier spectral analysis. Although extremely versatile and simple, the technique suffers from some stiff contraints that limit its usefulness when attempting to examine the effects of optical turbulence in the frequency domain. Namely, the system must be linear and the data must be strictly periodic or stationary. Strict stationarity is a constraint that is impossible to satisfy simply on practical grounds, since no detector can cover all possible points in phase space. The linearity requirement is also not generally fulfilled, since turbulent processes are by definition non–linear.

Fortunately a new technique that has come to be known as the Hilbert Huang Transform (HHT) has been developed,[1] patented by NASA. This allows for the frequency space analysis of non–stationary, non–linear signals. The HHT is composed of two main algorithms for filtering and analyzing such data series. Firstly it employs an adaptive technique to decompose the signal into a number of Intrinsic Mode Functions (IMFs) that have well prescribed instantaneous frequencies, defined as the first derivative of the phase of an analytic signal. The second step is to convert these IMFs into an energy–time–frequency relationship, by means of the Hilbert Transform.

Asides from overcoming the problems associated with more traditional Fourier methods, the HHT makes it possible to visualize the energy spread between available frequencies locally in time, rather like wavelet transform methods. The advantage the HHT has over wavelet transforms is that it is of much higher resolution, since it does not *a priori* assume a basis; rather it "lets the data do the talking".

2. INSTANTANEOUS FREQUENCY

Key to the HHT is the idea of instantaneous frequency, which we will sometimes refer to as simply "the frequency". The ideal instantaneous frequency is quite simply the frequency of the signal at a single time point. No knowledge is required of the signal at other times. Naturally such a statement leads to difficulties in definition; Huang et al[2] take it to be the derivative of the phase of the analytic signal, found from the real and imaginary parts of the signal's Hilbert Transform, which we follow.

Further author information: (Send correspondence to M.P.J.L.C.)
M.P.J.L.C.: E-mail: mchang@uprm.edu, Telephone: 1 787 265 3844

The immediate problem in dealing with a phase so defined is that, for the most part, the Hilbert Transforms of the direct signals are not well behaved resulting in negative instantaneous frequencies which do not represent physical effects. The method by which this is circumvented is to ensure that the input to the Hilbert Transform obeys the following conditions:

(a) The number of local extrema of the input and the number of its zero crossings must be either equal or differ at most by one.

(b) At any point in time t, the mean value of the upper envelope (determined by the local maxima) and the lower envelope (determined by the local minima) is zero.

The functions that obey these are considered the IMFs.

3. EMPIRICAL MODE DECOMPOSITION

We have implemented an IMF filtering algorithm, known as Empirical Mode Decomposition (EMD), following Huang et al.[1,3] The IMFs and the residual trend line thus obtained are verified to be complete by simply summing them to recreate the signal. The maximum relative error we have found is of the order 10^{-9} %.

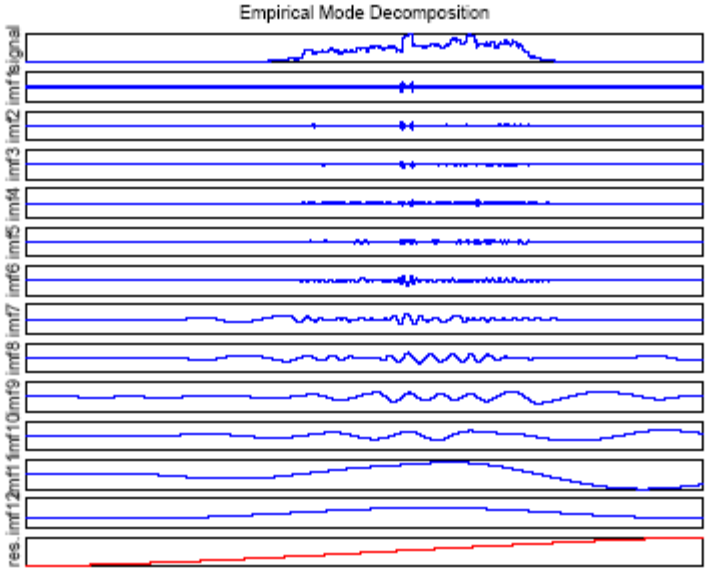

Figure 1. The IMFs found from a typical input signal (taken on 9-March-2006), with the signal itself shown at the top. For convenience, we refer to the lowest order IMF as one with the fastest oscillation. The bottom-most graph is the residual after removing all the IMFs and represents the overall trend.

The IMFs show that in a very real sense the EMD method is acting as a filter bank, separating the more rapid oscillations from the slower oscillations. It seems that a subset of the individual IMFs may be added to determine the effect of physical variables, as suggested in Figure 2. In the absence of the major effects of

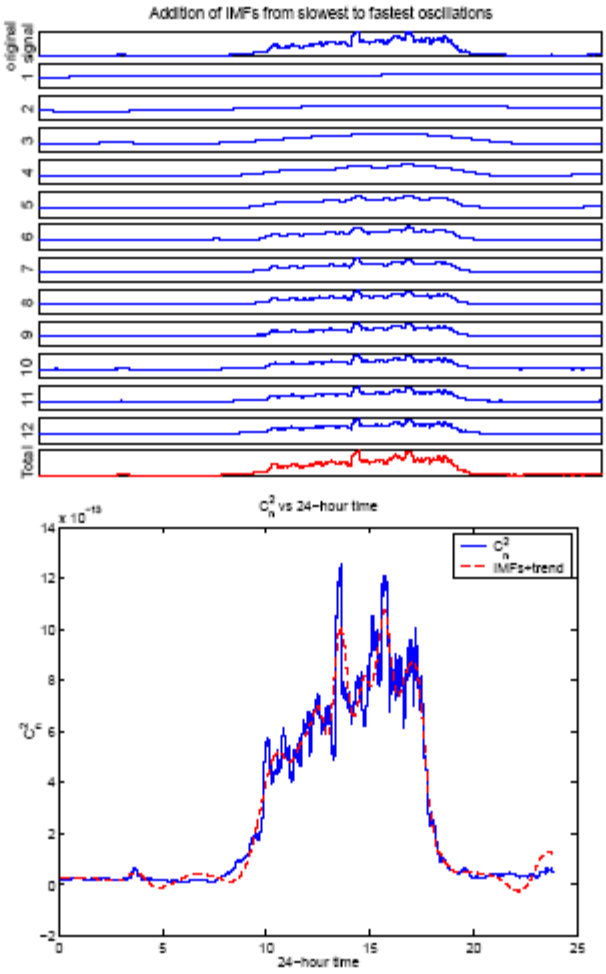

Figure 2. (a) Stepwise summation of the 9-March-2006 IMFs and trend line to recreate the original input signal. (b) The sum of the trendline and the slowest 3 IMFs superimposed on the input signal. The overshoot into negative values of C_n^2 is unphysical, and serves to demonstrate that the information content of the subset is incomplete. Nevertheless, the fit does suggest that the IMFs represent an underlying physical process (primarily solar insolation).

solar insolation, the HHT technique reveals that the majority contribution to the C_n^2 signal lies in the highest order (slowest oscillation) IMFs, as can be seen from the extremely faithful fit to the data composed of the trend line and the 3 highest order IMFs shown in Figure 3. As a guide to the significance of the various modes,

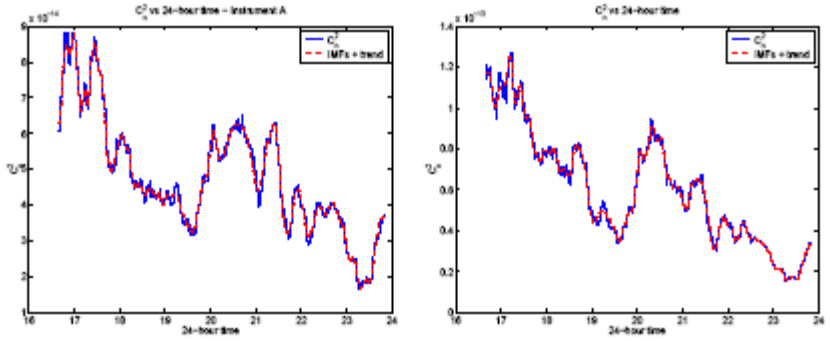

Figure 3. The 20-Feb-2006 C_n^2 and fit composed of the trend line and 3 highest order IMFs for both instruments (A on the left and B on the right). Sunset was at 18:31 local time.

we examined the energy in the IMFs and compared the energy in each mode to the energy distribution of red noise. As an initial naïve estimator, we take IMF1 to be representative of the noise contained in the data. This is unlikely to be completely correct; probably a better noise estimator would be IMF1 - <IMF1>, where the angle brackets signify the mean value over the same temporal epoch (e.g. month or season). We do not do this simply because we do not have sufficient data.

We define the red noise (random) time series to be an AR1 process

$$r(t_n) = \sigma E(t_n) + \rho r(t_{n-1}) \tag{1}$$

The terms are:

$$\begin{aligned} \sigma &:= \text{standard deviation of IMF1} \\ E &:= \text{uniform distribution of random numbers between 1 and -1} \\ t_n &:= \text{the } n\text{th timestep} \\ \rho &:= \text{the autocorrelation at 1 lag step of IMF1} \\ r &:= \text{the random time series} \end{aligned} \tag{2}$$

The IMFs of an ensemble of AR1 time series are generated and then this Monte Carlo is used to simulate the power distribution of the noise. The power of each C_n^2 derived IMF is then compared to the noise power distribution to determine the mode's significance. Figure 4 shows that of the IMFs, the first three lie at or below the median red noise power. IMF4 to IMF9 lie above the median noise power, with the higher order IMFs being most significant. We interpret this simulation to mean that IMF6-IMF9 are highly physically significant.

4. HILBERT TRANSFORM OF IMFS

Following the decomposition into IMFs of the original signal, the derived components can be Hilbert transformed to produce a time–frequency map or spectrum. Figure 5 shows that during the hours when there is no solar insolation the C_n^2 energy is distributed in the lowest frequencies. The highest frequencies sampled are only reached after the Sun is contributing energy into the lower atmosphere. The discontinuous, filamentary aspect of the plot indicates a large number of phase dropouts which shows that the data are non–stationary.

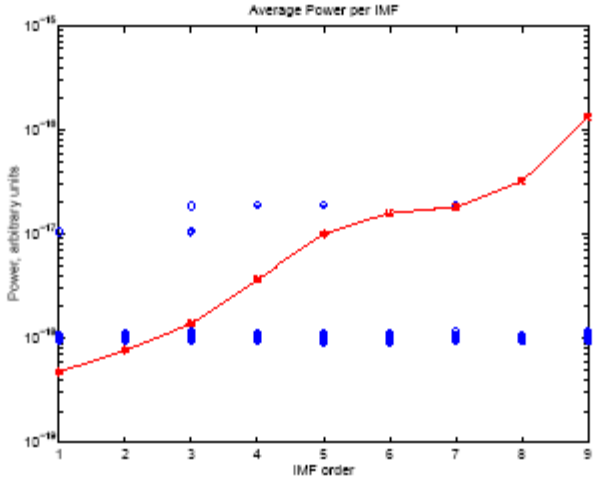

Figure 4. Monte Carlo simulations show the significance of the C_n^2 (solid line) derived IMFs for a single instrument on the afternoon/evening of 20-Feb-2006, compared to the equivalent red noise power (open circles).

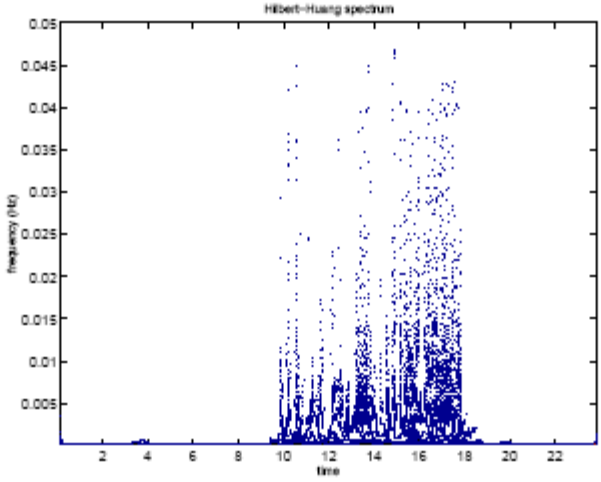

Figure 5. The Hilbert spectrum of the 9-March-2006 IMFs shown in Figure 1 plotted as a series of contour lines.

We are also able to find a Marginal Spectrum by integrating the Hilbert spectrum across time. The Marginal Spectrum shown in Figure 6 clearly suffers from less leakage into the high frequencies than the Power Spectrum. The interpretation of both spectra are quite different: the Fourier Power Spectrum indicates that certain frequencies exist throughout the entire signal with a given squared amplitude. The Marginal Spectrum, on the other hand, describes the probability that a frequency exists at some local time point in the signal. It is clear

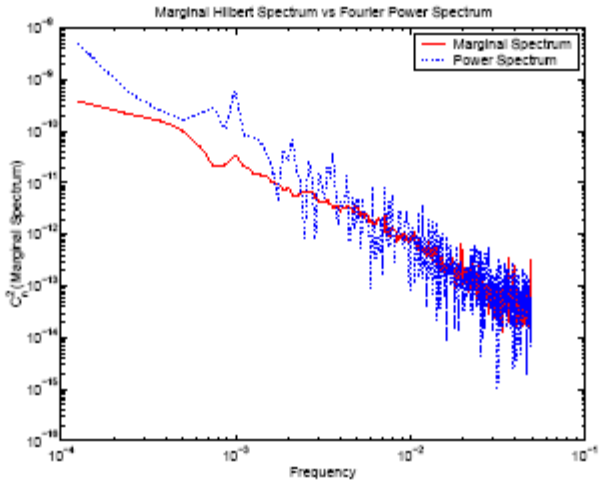

Figure 6. The Hilbert Marginal spectrum (solid line) of the 9-March-2006 IMFs compared to the Fourier Power Spectrum (dotted line) of the same data. The Power Spectrum has been shifted so that its maximum frequency coincides with that of the Marginal Spectrum. Note also that the units of the ordinate axis are arbitrary for the Fourier Power Spectrum.

that the two spectra have a difference in the standard deviations: the logarithm of the Marginal Spectrum has a standard deviation of 1.88 compared to the logarithm of the Fourier Power Spectrum, whose standard deviation is 2.24.

Applying a Kolmogorov–Smirnov test to the two spectra returns a P–value of 0 and a cumulative distribution function distance of 1, indicating that the data sets represent different distributions, as we might guess from their different gradients. We may therefore state that the spectra are unrelated and we argue on the basis of non–stationarity that the Fourier Power Spectrum has little, if any, physical meaning.

5. INSTRUMENTS AND DATA REDUCTION

The C_n^2 data used in this study was collected during 2006 at the University of Puerto Rico, Mayagüez Campus, on the rooftop of the Physics Department.

The data were obtained with two commercially available scintillometers (model LOA-004) from Optical Scientific Inc, co–located such that the transmitter of system 1 was next to the receiver of system 2.

Each LOA-004 instrument comprises of a single modulated infrared transmitter whose output is detected by two single pixel detectors. For these data, the separation between transmitter and receiver was just under 100-m. The sample rate was set to 10 seconds, so that each C_n^2 point was found from a 10 second time average. The path integrated C_n^2 measurements are determined by the LOA instruments by computation from the log–amplitude scintillation ($C_\chi(r)$) of the two receiving signals.[4,5] The algorithm for relating $C_\chi(r)$ to C_n^2 is based on an equation for the log–amplitude covariance function in Kolmogorov turbulence by Clifford *et al.*[6]

The data was collected by dedicated PCs, one per instrument. During analysis, the data were smoothed by a 120 point (10 minute) boxcar rolling average. This value was chosen for future ease of comparison with local weather station data, sampled at one reading per 10 minutes. Figure 7 compares the extracted IMFs from a single day, from midnight to midnight. There are no data dropouts in the time signal for instrument A, while instrument B is 99.81% valid. A visual examination reveals that the measured C_n^2 functions are very similar and both instruments have 11 IMFs. Differences are to be found in the IMFs themselves. In Figure 8 we show

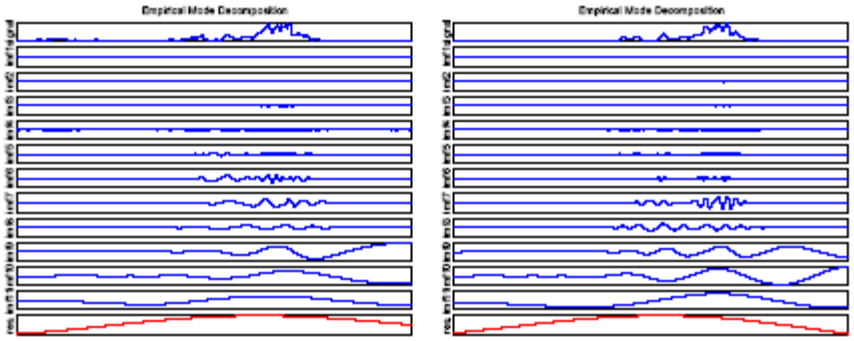

Figure 7. The IMFs extracted from each instrument for the same day (3-March-2006), beginning and ending at midnight (A on the left and B on the right).

the Hilbert Marginal Spectra derived from the IMFs together with a Kolmogorov Power Spectrum trend scaled to start coincident with the Marginal Spectra. Both Marginal Spectra follow each other fairly well, with similar frequency probabilities. Applying a Kolmogorov–Smirnov test to the two Marginal Spectra data sets gives the same means and standard deviations. This is indicative of a P–value of 1 and a cumulative distribution function distance of 0, so we may conclude that the instrument outputs have come from exactly the same distribution and are statistically identical. A further confirmation can be found by calculating the Hilbert phase difference between the two Marginal Spectra. Such a test displays phase synchronization, or lack thereof. In this case we find a phase difference of zero, so that the spectra are perfectly in phase.

6. CONCLUSIONS

We have presented the results of applying the Hilbert Huang Transform to C_n^2 time series data. When used to compare the outputs of two of the same model of commercial scintillometer, we have been able to demonstrate that they provide identical output in terms of their Hilbert Marginal Spectra. It is clear that the HHT technique is a very useful tool in the analysis of non–stationary turbulence data and promises much in terms of understanding the nature of optical turbulence.

ACKNOWLEDGMENTS

MPJLC would like to thank Norden Huang for introducing him to the Hilbert Huang Transform. Thanks also are due to Sergio Restaino and Christopher Wilcox for making available the scintillometers and providing data processing software.

REFERENCES

1. N. E. Huang, Z. Shen, S. R. Long, M. C. Wu, H. H. Shih, Q. Zheng, N.-C. Yen, C. C. Tung, and H. H. Liu, "The empirical mode decompcsition and the Hilbert spectrum for nonlinear and non-stationary time series analysis," *Proc. R. Soc. Lond. Ser. A* 454, pp. 903–995, 1998.

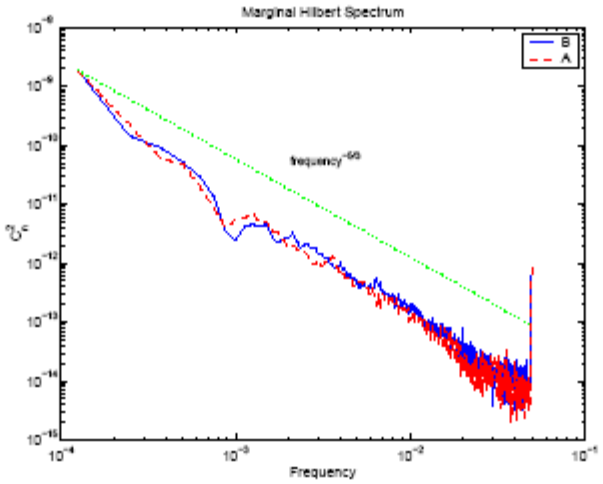

Figure 8. The 3-March-2006 Marginal Spectra of both instruments with a comparison frequency$^{-5/3}$ (Kolmogorov Spectrum) trend line.

2. N. E. Huang, S. R. Long, and Z. Shen, "A new view of water waves - the Hilbert spectrum," *Ann. Rev. Fluid Mech.* 31, pp. 417–457, 1999.
3. N. E. Huang, M.-L. C. Wu, S. R. Long, S. S. P. Shen, W. Qu, P. Gloersen, and K. L. Fan, "A confidence limit for the empirical mode decomposition and Hilbert spectral analysis," *Proc. R. Soc. Lond. Ser. A* 459, pp. 2317–2345, 2003.
4. G. R. Ochs and T.-I. Wang, "Finite aperture optical scintillometer for profiling wind and C_n^2," *Applied Optics* 17, pp. 3774–3778, 1979.
5. T.-I. Wang, "Optical flow sensor." USA Patent No. 6,369,881 B1, April 2002.
6. S. F. Clifford, G. R. Ochs, and R. S. Lawrence, "Saturation of optical scintillation by strong turbulence," *Journal of the Optical Society of America* 64, pp. 148–154, 1974.

Applying the Hilbert Phase Analysis to the study of Atmospheric Turbulence Data

Carlos O. Font[1,2], Mark P. J. L. Chang[3], Charmaine Gilbreath[1] and Eun Oh[2]
Naval Research Laboratory, Freespace Photonics Communications Office, Code 5505, 4555 Overlook Ave, SW Washington, DC 20375
Naval Research Laboratory, Remote Sensing Division, Code 7231, 4555 Overlook Ave, SW Washington, DC 20375
Physics Department, University of Puerto Rico, Mayagüez Campus, PO Box 9016, Mayagüez, PR 00681-9016
carlos.font@gmail.com

Abstract Hilbert Phase Analysis is a new technique that combined with the Hilbert-Huang Decomposition method allows analysis of a non-stationary data. We apply this method for the study of the C_n^2 parameter and weather data. ©2006 Optical Society of America
OCIS Codes: 010.1330 Atmospheric Turbulence, 070.4340 Nonlinear Optical Signal Processing

1. Introduction

In studying atmospheric turbulence and weather data, the principal problem is the non-stationarity and non-linearity of the data sets. This can be solved by the application of the Hilbert-Huang Decomposition method [1]. With the application of this technique we extract the Intrinsic Mode Functions (IMFs), whose instantaneous frequencies are well defined. Upon applying the Hilbert Transform to the extracted IMFs, we can define Hilbert Phase Angles [2] for the time series, with which we can study the physical behavior of the systems. We refer to this algorithm as the Hilbert Phase Angle or HPA method.

2. Applying the HPA technique to Atmospheric Turbulence (C_n^2) and Solar Radiation data.

As observed in Figure (1), the Hilbert phase angle of solar radiation in a 24-hour time period shows an increase in the gradient when sunrise occurs and a decrease at sunset, maintaining a constant, low gradient during the night. During daytime there are changes in phase gradient as the solar radiation intensity varies. We infer that the phase angle is describing the transport of energy in the system. On the right, we see the difference between the solar radiation phase and the C_n^2 phase, for the same day. The strong influence of solar radiation on the behavior of C_n^2 in the daytime causes the mean phase difference to be constant while there is measurable solar radiation. We postulate that other local ambient parameters causing the remaining fluctuations during the day and night. The rapid oscillations are probably due to poor phase unwrapping.

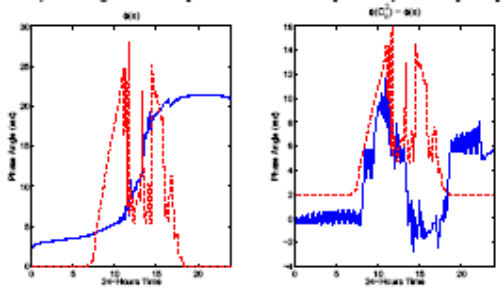

Figure 1. (Left) Plot of the Hilbert Phase for the solar radiation for 02/21/06. (Right) Plot of the Hilbert Phase difference between C_n^2 and the solar radiation for 02/21/06. In each graph the solar radiation function is superimposed at an arbitrary scale.

3. References

[1] M. P. J. L. Chang, Erick A. Roura, C. O. Font, C. Gilbreath and E. Oh "Applying the Hilbert–Huang Decomposition to Horizontal Light Propagation C_n^2 data," in Advances in Stellar Interferometry, J. D. Monnier, M. Schoeller and W. C. Danchi, eds., Proc. SPIE vol. 6268 (2006). [in press]
[2] C. O. Font, M. P. J. L. Chang, Erick A. Roura, E. Oh and C. Gilbreath "On the relationship between C_n^2 and Humidity," in Advances in Stellar Interferometry, J. D. Monnier, M. Schoeller and W. C. Danchi, eds., Proc. SPIE vol. 6268 (2006). [in press]

Appendix B

Journal Paper

Submitted to Applied Optics in June 7 2006. Revise on November 9 2006. Pre-print available on ArXiv server physics/0606075.

Humidity's influence on visible region refractive index structure parameter C_n^2

Mark P. J. L. Chang, Carlos O. Font[1,2],

[1] *Physics Department, University of Puerto Rico, PO Box 9016, Mayagüez, Puerto Rico 00681-9016*

G. Charmaine Gilbreath and Eun Oh

[2] *U.S. Naval Research Laboratory, Washington D.C. 20375*

mchang@uprm.edu

In the near infrared and visible bandpass, optical propagation theory conventionally assumes that humidity does not contribute to the effects of atmospheric turbulence on optical beams. While this assumption may be reasonable for dry locations, we demonstrate in this paper that there is an unequivocal effect due to the presence of humidity upon the strength of turbulence parameter, C_n^2, from data collected in the Chesapeake Bay area over 100-m length horizontal propagation paths. We describe and apply a novel technique, Hilbert Phase Analysis, to the relative humidity, temperature and C_n^2 data to show the contribution of the relevant climate variable to C_n^2 as a function of time.

OCIS codes: 010.1300, 010.7060, 030.7060

1. Introduction

It has been known for some time[1] that the scintillation behaviour of point sources is a measure of the optical seeing in the atmosphere. What has been less well understood is the contribution of different environmental variables to optical seeing.

Over the past decade, a great deal of study has been dedicated to clarifying this issue. Comprehensive treatments of the theory of wave propagation in random media are given in Tatarskii's seminal works.[2,3] Some of the simplest models based on these complex works are well known and available in the literature: Hufnagel–Valley,[4] SLC-Day and SLC-Night.[5] These models are commonly used to predict the strength of weak clear air turbulence's refractive index structure parameter, C_n^2.

The underlying assumption is that the index of refraction of air depends solely upon pressure and temperature at visible and near infrared wavelengths.[2,6] We can verify this from landbound horizontal path measurements. These show that during the daylight hours on a clear sunny day, the weak scintillation régime C_n^2 trend is dominated by solar insolation, as is illustrated by the left hand plot of Fig. 1.

The right hand plot of Fig. 1 illustrates the well known fact that the effects of turbulence do not cease after sunset. Here it is less clear as to the predominant contributing factors. The assumption of temperature dominance is sensible in the driest of environments, but we will demonstrate from experimental evidence that this is an incomplete condition where there is a significant amount of water vapour

entering or leaving air volume where C_n^2 is measured.

1.A. Past work

A body of work has been reported whose aims have been to compare bulk climate estimates of C_n^2 with optically derived readings.[7,8,9] In those works, the wavelengths of the optical measurements were in the mid–infrared (3 to 5 μm), and all showed that humidity along the measurement volume plays a significant rôle in the temporal behaviour of C_n^2.

In a theoretical study of the structure parameter using bulk measureables over sea ice and snow, Andreas[10] defined a refractive index scale n_* via

$$n_* = At_* + Bq_* \rightarrow \frac{n_*}{At_*} = 1 + \frac{Bq_*}{At_*} \tag{1}$$

where t_* and q_* represent temperature and humidity, scaled such they are constant with height and A and B are constants given in Appendix A. The variable n_* therefore represents a horizontal refractive index layer above the terrestrial surface. He rewrote Eq. (1) in terms of the Bowen ratio Bo, the ratio of sensible heat flux to latent heat flux, such that

$$\frac{n_*}{At_*} = 1 + \left(\frac{\rho c_p}{L}\right)\frac{B}{A(Bo)} = 1 + \left(\frac{B}{KA(Bo)}\right) \tag{2}$$

where c_p represents the specific heat of air at constant pressure, L the latent heat of sublimation of ice and ρ is the air density. Since $Bo \propto t_*/q_*$, this formulation allows the dependence of the refractive index scale upon temperature and humidity scales to be easily interpreted.

We adapt Eq. (2) to our experimental conditions by setting L to be the latent heat of vapourisation of water, and we assume $P = 1000$ hPa, $T = 25$ °C and $\lambda = 0.93$ μm. The result is shown in Fig. 2; from this it is clear that when $|Bo|$ is large, n_*/At_* is near 1. This means that when sensible heat (heat exchange without change of thermodynamic phase) dominates the Bowen ratio, the t_* in the denominator of Eq. (1) is the principal parameter.

When $|Bo|$ is small however, the latent heat flux dominates so q_* makes the major contribution to n_*. Thus there is an interplay between humidity and temperature effects upon the refractive index in the visible/near infrared, which vary as a function of the Bowen ratio. The pole at the origin of Fig. 2 is indicative of a breakdown of this formulation at very small Bowen ratios. Nevertheless the curve strongly suggests that as long as there is significant injection of moisture into the measurement volume of C_n^2, humidity effects become non-negligible.

In this paper we demonstrate that the temporal behaviour of the optically determined turbulence structure parameter C_n^2 in the visible and near infrared bandpass at a coastal site is strongly influenced by local humidity. Although no Bowen ratio values could be determined from the available measurements, the results do support the qualitative interpretation of Andreas' work.

2. Experiment and Correlogram Analysis

The C_n^2 and associated weather variable data used in this study were collected over a number of days during 2003 and 2004 at Chesapeake Beach in Maryland, USA.

The C_n^2 data were obtained with a commercially available scintillometer (model LOA-004) from Optical Scientific Inc, which serves as both a scintillometer and as an optical anemometer for winds transverse to the beam paths. The separation between source and receiver was just under 100-m, placing the system in the weak scintillation régime. The local weather parameters were determined by a Davis Provantage Plus (DP+) weather station. The LOA-004 had a sample rate of 10 seconds, while the DP+ was set at 5 minutes.

The LOA-004 instrument comprises of a single modulated infrared transmitter whose output is detected by two single pixel detectors. The transmitting LED has a bandwidth of 0.92 to 0.96 μm, while the detector bandwidth is much broader, at 0.65 to 1.0 μm. The path integrated C_n^2 measurements are determined by the LOA instrument by computation from the log–amplitude scintillation ($C_\chi(r)$) of the two receiving signals.[11,12] The algorithm for relating $C_\chi(r)$ to C_n^2 is based on an equation for the log–amplitude covariance function in Kolmogorov turbulence by Clifford *et al.*.[13]

The C_n^2 data was smoothed with a 60 point (5 minute) rolling average function. We define the morning and night portions of a 24 hour period with respect to the

measured solar irradiance function, such that we exclude the effect of solar insolation from the data in this study. Morning runs from midnight until sunrise, while night runs from sunset until 23:59. As reported in Oh *et al.*[14,15,16] visual inspection of the time series data gives the impression that there is an approximate inverse relationship between C_n^2 and relative humidity. This can be appreciated in a more quantitative manner by graphing one parameter against the other.

We chose data sets in which the temperature variations are no more than 16° F and the pressure change is at most 15 hPa over the time intervals of interest. The actual range of variation per data set is shown in table 1. The data sections were also selected to have no scattering effects due to snow or rain, and the wind was northerly (to within approximately ±20°, inflowing from the bay to land). Only a small subset eight morning and evening runs, spanning seven days between November 2003 and March 2004, provided complete time series in both ambient weather variables and C_n^2. Part of this is shown in Fig. 3; the C_n^2 vs. humidity correlograms evidence a negative gradient in all eight runs. Table 1 shows us that the relative humidity variation is more strongly reflective of changes in absolute moisture content than of moisture holding capacity of the air.

We conclude that humidity plays a significant part in the behaviour of the refractive index structure parameter C_n^2 in the datasets studied.

3. The Stationarity Problem

The unsophisticated use of the correlogram tool in Section 2 is a rapid, first order method for inferring the statistical influence of one measurable upon another. However it is unsatisfactory as it does not reveal any detailed information, such as exactly when the humidity contribution is important with respect to all other possible parameters (e.g. temperature) and to what degree its contribution is influential. Cross covariance techniques are a possible second order method[17] for extending the analysis, but there are two major stumbling blocks. The first is the difficulty in interpreting the meaning of the covariance functions physically and the second is the non–stationary nature of the data. In the latter case it is well known that strict stationarity is a constraint that is impossible to satisfy on practical grounds, since no detector can cover all possible points in phase space. This has motivated us to employ a novel analysis technique to infer the relationship between C_n^2 and climate parameters, which we briefly describe in the following section. We leave a more detailed study of the limitations of the technique to a separate paper.

3.A. The Analytic Signal

Gabor[18] defined the complex analytic signal, namely

$$\Psi(t) = X(t) + iY(t) \tag{3}$$

$$\text{where } Y(t) = \mathcal{H}[X(t)] = \frac{-1}{\pi}\mathbf{P}\int_{-\infty}^{\infty}\frac{X(\tau)}{(t-\tau)}d\tau$$

where $\mathcal{H}[\bullet]$ represents a Hilbert Transform. Through this definition, $\Psi(t)$ is unique. The Hilbert Transform is a well known integral transform with a singular kernel $(1/(\pi(t-\tau))$, τ also being a time variable if t is time. It is also a Cauchy Principal integral, which we denote by P. Note that the Hilbert Transform preserves the norm of the real signal; the difference between Y and X is a $\pi/2$ phase shift for a periodic function. That is, the Hilbert Transform of $\cos t$ is $\sin t$, and $\sin t$ is $-\cos t$, and the transform of a constant is zero.

Eq. (3) means that we can write the analytic signal as

$$\Psi(t) = a(t)\exp^{i\Phi(t)} \quad , \quad \text{where} \quad \begin{aligned} a(t) &= \sqrt{X^2(t)+Y^2(t)} \\ \Phi(t) &= \arctan\left(\frac{Y(t)}{X(t)}\right) \end{aligned} \tag{4}$$

which is similar to the well known Fourier expression. We may now determine the instantaneous signal phase, $\Phi(t)$. Thus we can also calculate the instantaneous frequency $\omega(t)$, defined as

$$\omega(t) = \frac{d\Phi(t)}{dt}. \tag{5}$$

Both $\Phi(t)$ and $\omega(t)$ can be interpreted as physical measureables, provided certain preconditions are met which we describe below.

3.B. Hilbert Phase Analysis

There is a problem with the definition of Eq. (3); the Hilbert Transform's kernel represents a non–causal filter, of infinite support. So if one applies the Hilbert Transform

directly to a time varying signal which has a non-zero local mean in any subsection, there is a high probability that at least one of a number of paradoxes[19] will be encountered. This may be best appreciated if we consider a signal in phase space, as in the left hand plot of Fig. 4. Here we show the real versus imaginary components of the Hilbert Transform of a series of analytic C_n^2 measurements. The trajectory of the analytic signal's vector is subject to many alterations in the vector start point, norm and phase angle. Any attempt to determine the instantaneous frequency is bound to be problematic as we are not able to follow the signal vector's start position over time; this starting point obviously does not remain at the origin of the coordinate system. Calculating the instantaneous frequency from the Hilbert Transform as is will generate both positive and negative values, rendering it physically uninterpretable.

The paradoxes may be avoided by the application of the Empirical Mode Decomposition (EMD) method developed by Huang *et al*,[20] which we have implemented[21,22]. EMD is a unique and novel method that is able to separate an arbitrary real time series into "eigenfunctions" termed Intrinsic Mode Functions or IMFs, each of which possesses a structure with well defined instantaneous frequencies, $\omega(t)$. The term eigenfunction is used suggestively here; we do not mean to imply that the IMFs are eigenfunctions in the strict sense.

Briefly, the EMD technique consists of (1) the determination of two envelope functions about the time series, covering all the local minima and maxima respectively; (2) the computation of the mean of the two envelope functions; (3) the removal of the

mean of the envelopes from the time series in an iterative manner, until the mean is found to be zero; (4) the storing of the resulting mode as an IMF. The IMF is then subtracted from the original time series and steps (1) to (4) are repeated, thereby sifting out a family of IMFs, stopping only when the resulting mode shows no variation. The final mode represents the overall trend of the signal and is not itself an IMF.

The Hilbert Transform of the IMFs, one of which is shown on the right side of Fig. 4, ensures that the analytic signal vector's origin stays fixed and no sudden changes in the direction of $\omega(t)$ occur. These conditions being satisfied, the instantaneous frequency remains positive and physically meaningful.

4. Hilbert Phase Analysis

The *Hilbert Phase Analysis* (HPA) technique is based on the ideas mentioned in the previous subsections. It is clear that a phase angle ($\Phi(t)$), as well as an amplitude ($a(t)$), can be found from the Hilbert Transform of the IMFs derived from the EMD sifting process.

The procedure for the HPA data analysis follows a three step protocol:

1. Decompose the time series measurements of differing parameters via EMD, obtaining their IMFs and trend lines.

2. Apply the Hilbert Transform to the various IMF sets. We discard the trend lines as the reason that the original time series fail to be Hilbert Transformed

in a physically comprehensible manner.

3. Examine the instantaneous phase angles of the Hilbert Transformed IMFs between different parameters to infer the dynamics of the physical system.

4.A. Interpretation of HPA

In this section we demonstrate that physical effects of a non–linear, non–stationary, time varying system can be studied via the sum of all IMF phases, $\sum_{IMF} \Phi(t)$.

In Fig. 5 the $\sum_{IMF} \Phi(t)$ is graphed with the solar radiation data superimposed for example days. There is clearly a gradient change in the phase function at sunrise and sunset. Also notable is the phase jump towards a lower gradient whenever the solar radiation function exhibits a drop in amplitude; likewise the phase gradient increases with sudden increases in the measured solar radiation. This can be understood as: a reduction in energy in the system leads to a lower instantaneous frequency, therefore we see a lower phase gradient. A change in energy results in a change in instantaneous frequency, so we see a modified gradient.

We conclude that overall physical features of a non–stationary time series can be extracted by inspection of the sum of its Hilbert Phases of the IMFs.

5. HPA of C_n^2, humidity and temperature

5.A. Phase locking between measureables

To better understand the dependence of Φ_C upon humidity and temperature, we consider the difference between observable phases, as illustrated in Fig. 7. We define the following difference terms,

$$\begin{aligned} \Delta_{CT} &= \sum \Phi_C - \sum \Phi_T \ , \quad \Delta_{CH} = \sum \Phi_C - \sum \Phi_H \\ \Delta_{C\overline{HT}} &= \sum \Phi_C - \frac{(\sum \Phi_H + \sum \Phi_T)}{2} \end{aligned} \tag{6}$$

representing the phase differences between C_n^2 and the bulk climate parameter. It is anticipated that the controlling climate parameter will be indicated by a near zero difference, Δ. We reason this because if Δ is constant between C_n^2 and a climate variable then the two datasets must be phase locked. If the mean Δ is zero, then any variations about zero should indicate a synchronization between the datasets. Supporting empirical evidence is found upon studying cases wherein the solar insolation influence upon the measured C_n^2 is strong, as in Fig. 6. In those plots one can see that the difference between the summed Hilbert Phase of C_n^2 and solar radiation $(\sum \Phi_C - \sum \Phi_S)$ flattens out when the solar function is significant.

Motivated by this, we determined by linear regression the mean gradients of all the Δ curves, which we list in Table 2. If we assume that the only major contributor should be the local temperature variations, Δ_{CT} should be zero or near zero in all cases. This turns out not to have occurred. In fact, Δ_{CT} has no near zero value, so

temperature variation cannot be said to be phase locked with the refractive index structure parameter.

If humidity has a controlling effect in the visible / near infrared, then it should exhibit a range of values near zero for Δ_{CH}. It only does so for 11/10/03 (am) and 03/28/04 (am). It is noteworthy that 11/09/03 shows a possible phase lock between the mean of humidity and temperature with C_n^2. This seems to indicate that that temperature is vying with humidity for influence over the C_n^2 parameter during that morning.

5.B. Further study

If we define "dominance" to mean that the phase gradient is the value closest to zero of the differences under scrutiny then we find that humidity is dominant for the 11/10/03, 02/02/04, 03/27/04 and 03/28/04 datasets. The 11/03/03 and 04/03/04 (a.m. and p.m.) datasets show that $\Delta_{CT} < \Delta_{CH}$, indicating the dominant effect is temperature, this being extremely strong for the 04/03/04 (pm) dataset and rather weaker for the other two. We postulate that the 11/03/03 and 04/03/04 datasets indicate both temperature and humidity are contributing to the behaviour of C_n^2, with the HPA method possibly showing the proportional contribution to C_n^2 of each climate variable. This is clearly an area to be examined further.

6. Conclusions

From experimental data we have shown conclusively that humidity plays a significant part in the visible/near infrared measure of C_n^2 in a coastal environment. This is in qualitative agreement with Andreas' model and is a natural extension of the results from the mid infrared.

Furthermore we have explored a new technique, Hilbert Phase Analysis, with which to study this physical phenomenon. In overall terms, the HPA method is in agreement with the correlogram results. Phase locking between data is an unexpected result that needs further examination. We have found that the HPA technique described here is very promising and is likely to provide much more information about the changes to a physical system than traditional methods.

Appendix A: Definitions

The constants A and B of Eq. 1 in the 0.36 to 3 μm wavelength region are

$$A = -10^{-6} m_1(\lambda)(P/T^2) \tag{A1}$$

$$B = 4.6150 \times -10^{-6}[m_2(\lambda) - m_1(\lambda)].$$

P and T are the ensemble average air pressure and temperature, respectively. The functions m_1 and m_2 are polynomials in wavenumber given by

$$m_1(\lambda) = 23.7134 + \frac{6839.397}{130 - (1/\lambda)^2} + \frac{45.473}{38.9 - (1/\lambda)^2} \tag{A2}$$

$$m_2(\lambda) = 64.8731 + 0.58058(1/\lambda)^2 - 0.0071150(1/\lambda)^4 + 0.0008851(1/\lambda)^6$$

with λ's units in micrometres.

A. Acknowledgements

MPJLC is grateful to Norden Huang, Haedeh Nazari and Erick Roura for illuminating discussions. Part of this work was supported by the Office of Naval Research.

References

1. F. Roddier, "The Effects of Atmospheric Turbulence in Optical Astronomy," Progress in Optics **XIX**, 281–377 (1981).
2. V. Tatarskii, *Wave Propagation in a Turbulent Medium* (Mc Graw-Hill, New York, 1961).
3. V. Tatarskii, *The Effects of a Turbulent Atmosphere on Wave Propagation* (Israel Program for Scientific Translations, Jerusalem, 1971).
4. R. R. Beland, *Propagation through atmospheric optical turbulence* (SPIE Optical Engineering Press, Bellingham, Washington, 1993).
5. M. Miller and P. L. Zieske, "Turbulence environmental characterization," RADC-TR-79-131, ADA072379, Rome Air Development Center (1976).
6. M. C. Roggeman and B. Welsh, *Imaging through turbulence* (CRC Press, Boca Raton, Florida, 1996).
7. P. A. Frederickson, K. L. Davidson, C. R. Zeisse, and C. S. Bendall, "Esitimating the Refractive Index Structure Parameter (C_n^2) over the Ocean using Bulk

Methods," Journal of Applied Meteorology 39, 1770–1783 (1999).

8. K. L. Davidson, G. E. Schacher, C. W. Fairall, and A. K. Goroch, "Verification of the bulk method for calculating overwater optical turbulence," Applied Optics 20, 2919–2924 (1981).

9. G. J. Kunz, M. M. Moerman, P. J. Fritz, and G. de Leeuw, "Validation of a bulk turbulence model with thermal images of a point source," in *Image Propagation through the atmosphere*, C. Dainty and L. R. Bissonnette, eds., vol. 2828 of *Proc. SPIE*, pp. 108–116 (1996).

10. E. L. Andreas, "Estimating C_n^2 over snow and sea ice from meteorological data," Journal of the Optical Society of America A 5, 481–494 (1988).

11. G. R. Ochs and T.-I. Wang, "Finite aperture optical scintillometer for profiling wind and C_n^2," Applied Optics 17, 3774–3778 (1979).

12. T.-I. Wang, "Optical Flow Sensor," USA Patent No. 6,369,881 B1 (2002).

13. S. F. Clifford, G. R. Ochs, and R. S. Lawrence, "Saturation of optical scintillation by strong turbulence," Journal of the Optical Society of America 64, 148–154 (1974).

14. E. Oh, J. Ricklin, F. Eaton, C. Gilbreath, S. Doss-Hammell, C. Moore, J. Murphy, Y. H. Oh, and M. Stell, "Estimating Optical Turbulence Using the PAMELA Model," in *Remote Sensing and Modeling of Ecosystems for Sustainability*, W. Gao and D. R. Shaw, eds., vol. 5550 of *Proc. SPIE*, pp. 256–266 (2004).

15. S. Doss-Hammel, E. Oh, J. C. Ricklin, F. D. Eaton, G. C. Gilbreath, and D. Tsintikidis, "A comparison of optical turbulence models," in *Remote Sensing and Modeling of Ecosystems for Sustainability*, J. C. Ricklin and D. G. Voelz, eds., vol. 5550 of *Proc. SPIE*, pp. 236–246 (2004).

16. E. Oh, J. C. Ricklin, G. C. Gilbreath, N. J. Vallestero, and F. D. Eaton, "Optical turbulence model for laser propagation and imaging applications," in *Free-Space Laser Communication and Active Laser Illumination III*, D. G. Voelz and J. C. Ricklin, eds., vol. 5160 of *Proc. SPIE*, pp. 25–32 (2004).

17. C. O. Font, M. P. J. L. Chang, E. Oh, and C. Gilbreath, "Humidity contribution to the refractive index structure function C_n^2," in *Atmospheric Propagation III*, C. Y. Young and G. C. Gilbreath, eds., vol. 6215 of *Proc. SPIE* (2006).

18. M. Born and E. Wolf, *Principles of Optics, 7th ed.* (Cambridge University Press, Cambridge, 1999).

19. L. Cohen, *Time frequency analysis* (Prentice Hall, Englewood Cliffs, New Jersey, 1995).

20. N. E. Huang, Z. Shen, S. R. Long, M. C. Wu, H. H. Shih, Q. Zheng, N.-C. Yen, C. C. Tung, and H. H. Liu, "The empirical mode decomposition and the Hilbert spectrum for nonlinear and non-stationary time series analysis," Proc. R. Soc. Lond. Ser. A 454, 903–995 (1998).

21. M. P. J. L. Chang, E. A. Roura, C. O. Font, C. Gilbreath, and E. Oh, "Applying

the Hilbert–Huang Decomposition to Horizontal Light Propagation C_n^2 data," in *Advances in Stellar Interferometry*, J. D. Monnier, M. Schoeller, and W. C. Danchi, eds., vol. 6268 of *Proc. SPIE* (2006).

22. C. O. Font, M. P. J. L. Chang, E. Oh, and C. Gilbreath, "On the relationship between C_n^2 and humidity," in *Advances in Stellar Interferometry*, J. D. Monnier, M. Schoeller, and W. C. Danchi, eds., vol. 6268 of *Proc. SPIE* (2006).

23. H. Beaumont, C. Aime, E. Aristidi, and H. Lantéri, "Image quality and seeing measurements for long horizontal overwater propagation," Pure and Applied Optics 6, 15–30 (1997).

List of Figure Captions

Fig. 1. The effects of solar insolation on C_n^2 as measured on March 9, 2006 in Puerto Rico. Solar radiation measurements are superimposed at an arbitrary scale on top of the C_n^2 data. (Left) The full 24 hour period. The vertical axis values are of order 10^{-12} $m^{-2/3}$. (Right) Close up of the evening period. The vertical axis values are of order 10^{-14} $m^{-2/3}$. The C_n^2 data were obtained at an urban site 1.75-km from the sea. These values are in agreement with measurements of seeing over the sea by alternative means.[23]

Fig. 2. Graph of $n_*/(At_*)$ vs Bowen ratio for $\lambda = 0.93$ μm.

Fig. 3. Example correlograms of C_n^2 and Relative Humidity in the absence of solar insolation. The upper and lower bounds indicate the 50% confidence level. The C_n^2 magnitudes are 10^{-15} $m^{-2/3}$, in agreement with measurements of seeing over the sea by alternative means.[23]

Fig. 4. (left) Hilbert Phase Space plot of the trajectory of the C_n^2 signal vector of Fig. 1. The signal vector's start point drifts arbitrarily around the phase space, making the determination of a physically reasonable instantaneous frequency impossible over the whole path. (right) Hilbert Phase Space plot of the trajectory of a single IMF derived from the C_n^2 signal. The IMF vector's start point is stable and its trajectory does not change direction, so a positive instantaneous frequency can be determined at all points.

Fig. 5. Sum of all Hilbert Phases of the measured Solar Radiation IMFs ($\sum \Phi_S$) for the following days: Feb 2, Mar 27, Mar 28 and Apr 3, 2004. The Solar Radiation is superimposed at an arbitrary scale.

Fig. 6. Plots of Hilbert Phase differences between C_n^2 and solar radiation for 03/27/04 and 03/28/04. The solar radiation function is superimposed at an arbitrary scale on each graph. Note the flattening out of the phase difference function during the daylight hours.

Fig. 7. Difference plots for the morning of November 10, 2003. The dotted line is a linear regression, estimating the mean phase gradient. The top left graph shows a phase lock between C_n^2 and relative humidity.

Table 1. Mean and range of bulk parameters measurements and the maximum range of specific humidity (Δ_{Q_s}).

Table 2. Linear regression line gradients of the Phase Differences.

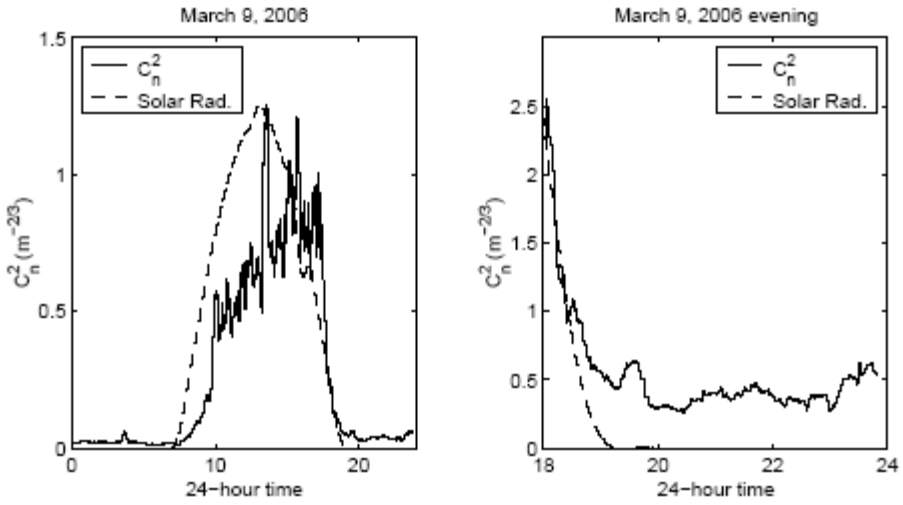

Fig. 1. The effects of solar insolation on C_n^2 as measured on March 9, 2006 in Puerto Rico. Solar radiation measurements are superimposed at an arbitrary scale on top of the C_n^2 data. (Left) The full 24 hour period. The vertical axis values are of order 10^{-12} $m^{-2/3}$. (Right) Close up of the evening period. The vertical axis values are of order 10^{-14} $\mathrm{m}^{-2/3}$. The C_n^2 data were obtained at an urban site 1.75-km from the sea.

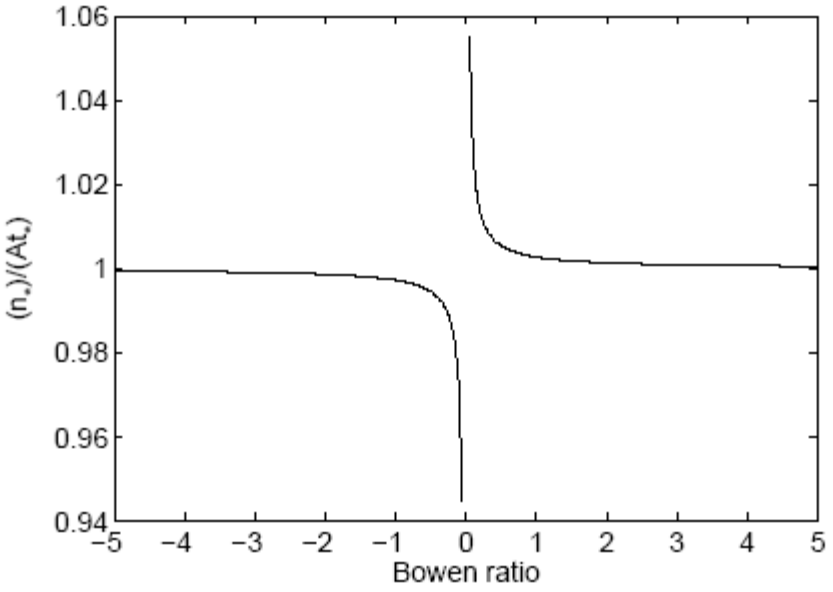

Fig. 2. Graph of $n_*/(At_*)$ vs Bowen ration for $\lambda = 0.93$ μm.

Table 1. Mean and range of bulk parameters measurements and the maximum range of specific humidity (Δ_{Q_s}).

Date	$\overline{RH}$ (%)	$\overline{T}$ (°F)	$\overline{P}$ (hPa)	Δ_{RH}	Δ_T	Δ_P	Δ_{Q_s} (g/kg)
11/03/03 (pm)	83.6	65.2	1015.3	15	2	0.4	2.2
11/09/03 (am)	49.3	38.8	1030.9	11	3.1	1.2	0.5
11/10/03 (am)	76.4	46.8	1027.6	11	8	1.8	0.6
02/02/04 (am)	91.4	29.9	1022.9	16	2.5	6.6	0.8
03/27/04 (pm)	76.4	46.8	1027.6	11	8	1.8	1.7
03/28/04 (am)	71	44.5	1027.6	16	0.7	0.6	0.9
04/03/04 (am)	76.1	46.6	997.4	18	5.9	4.9	0.4
04/03/04 (pm)	43	40.1	1004.5	14	5.6	2.1	1.1

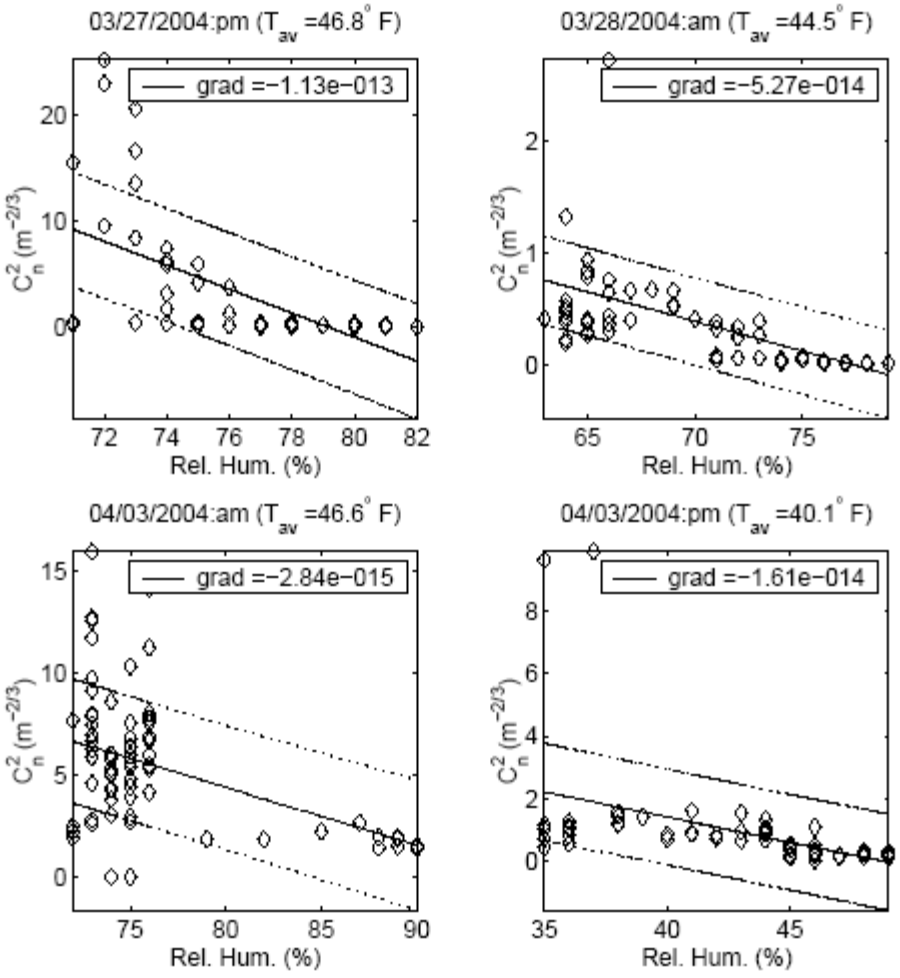

Fig. 3. Example correlograms of C_n^2 and Relative Humidity in the absence of solar insolation. The upper and lower bounds indicate the 50% confidence level. The C_n^2 magnitudes are 10^{-15} $m^{-2/3}$, in agreement with measurements of seeing over the sea by alternative means.[23]

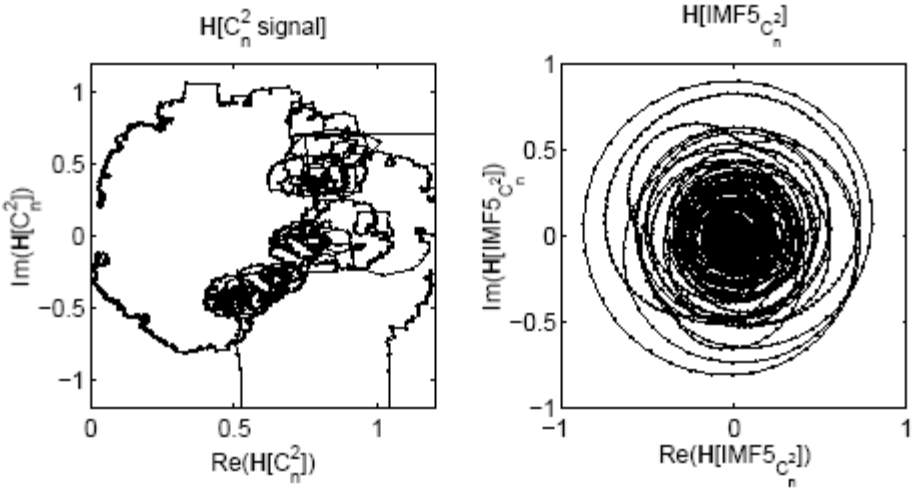

Fig. 4. (left) Hilbert Phase Space plot of the trajectory of the C_n^2 signal vector of figure 1. The signal vector's start point drifts arbitrarily around the phase space, making the determination of a physically reasonable instantaneous frequency impossible over the whole path. (right) Hilbert Phase Space plot of the trajectory of a single IMF derived from the C_n^2 signal. The IMF vector's start point is stable and its trajectory does not change direction, so a positive instantaneous frequency can be determined at all points.

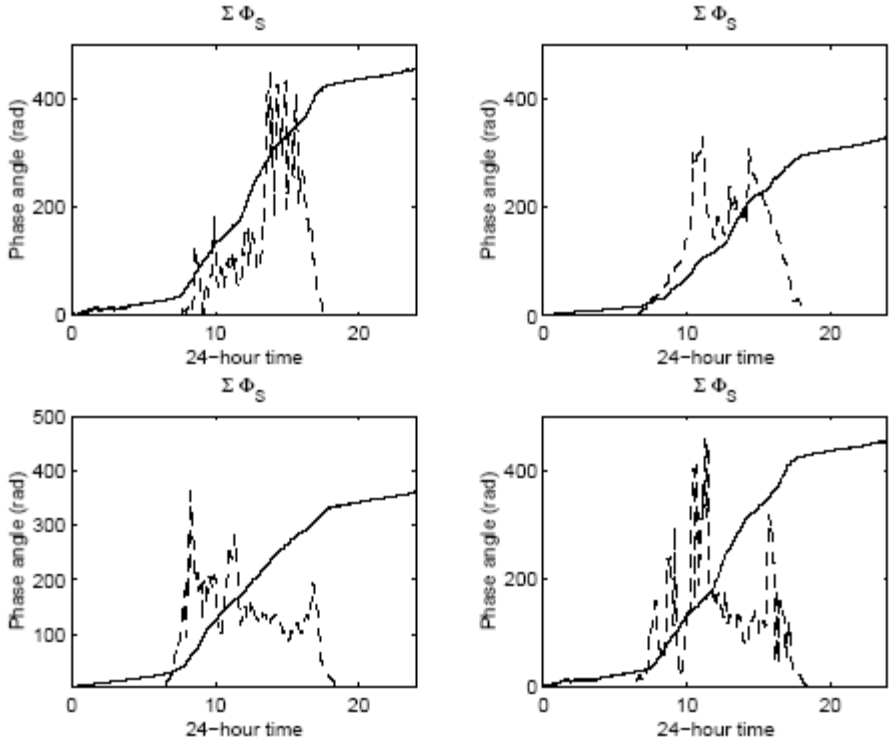

Fig. 5. Sum of all Hilbert Phases of the measured Solar Radiation IMFs ($\sum \Phi s$) for the following days: Feb 2, Mar 27, Mar 28 and Apr 3, 2004. The Solar Radiation is superimposed at an arbitrary scale.

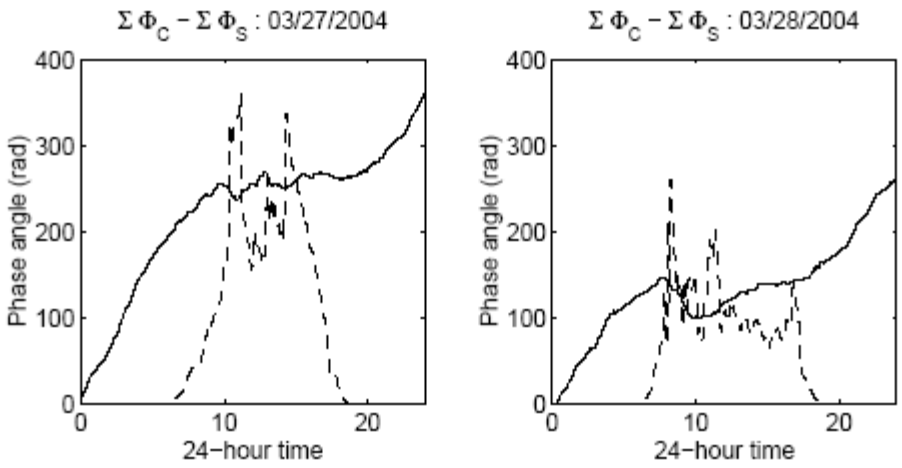

Fig. 6. Plots of Hilbert Phase differences between C_n^2 and solar radiation for 03/27/04 and 03/28/04. The solar radiation function is superimposed at an arbitrary scale on each graph. Note the flattening out of the phase difference function during the daylight hours.

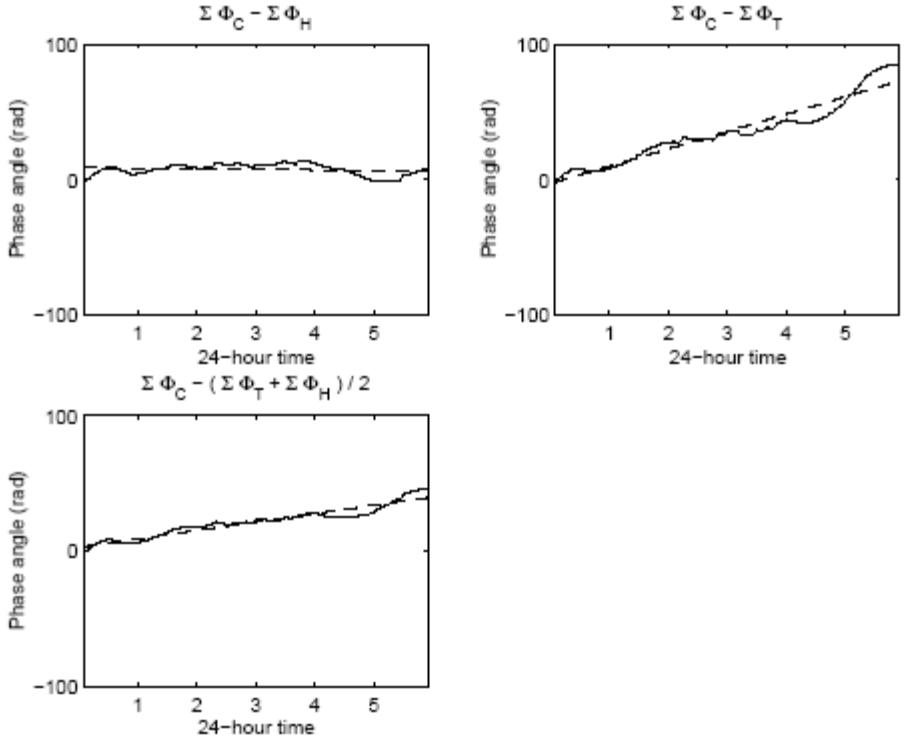

Fig. 7. Difference plots for the morning of November 10, 2003. The dotted line is a linear regression, estimating the mean phase gradient. The top left graph shows a phase lock between C_n^2 and relative humidity.

Table 2. Linear regression line gradients of the Phase Differences.

Date	Δ_{CH}	Δ_{CT}	$\Delta_{C\overline{HT}}$
11/03/03 (pm)	-9.7(4)	-8.0(0)	-8.8(7)
11/09/03 (am)	-11.2(4)	9.7(7)	-0.7(4)
11/10/03 (am)	-0.4(1)	12.7(9)	6.1(9)
02/02/04 (am)	8.5(1)	-12.3(0)	-1.8(9)
03/27/04 (pm)	3.7(6)	28.1(7)	15.9(7)
03/28/04 (am)	0.0(2)	-3.3(1)	-1.6(5)
04/03/04 (am)	6.8(1)	6.6(8)	6.7(4)
04/03/04 (pm)	-27.3(3)	-2.3(3)	-14.8(3)